DETECTION OF SINKHOLE PRECURSORS THROUGH SAR INTERFEROMETRY

by

Andre Theron

Thesis presented in fulfilment of the requirements for the degree of Master of Science in the Faculty of Science at Stellenbosch University

Supervisor: Dr J Kemp

Co-supervisor: Dr J Engelbrecht

Department of Geography and Environmental Studies

March 2017

Declaration

By submitting this thesis electronically, I declare that the entirety of the work contained therein is my own, original work, that I am the owner of the copyright thereof (unless to the extent explicitly otherwise stated) and that I have not previously in its entirety or in part submitted it for obtaining any qualification.

Andre Theron

March 2017

Abstract

Differential Interferometric Synthetic Aperture Radar (DInSAR) is a mature ground deformation monitoring technique and research presented in this thesis supports this technology as a key tool for an operational sinkhole early warning system in South Africa. Sinkholes are an unpredictable geohazard that endangers life and property in dolomitic terrains. They are a significant threat in Gauteng, the most populated and urbanised province in South Africa. More than 3000 events have been recorded here in the last ~50 years that has led to the loss of 37 lives and more than 1.2 billion Rands in property damage. There is a need for risk mitigation measures in areas that are already developed. Such measures will also allow further development of sinkhole-prone land. Small-scale surface subsidence is frequently present prior to the collapse of a sinkhole yet not much is known about this phenomenon. This is mostly due to the unpredictable nature of sinkholes and the challenges in monitoring large areas for small-scale deformation. Nevertheless, it is hypothesised that the presence of precursory surface deformation can be exploited to develop early warning systems to mitigate further damages. Spaceborne DInSAR is able to monitor small-scale surface deformation over large areas and can be exploited to detect and measure precursors to sinkhole development. Recently, there have been successful case studies supporting this technique for sinkhole precursor detection. Yet the operational limitations have not been determined.

The first results of DInSAR-based monitoring effort of dolomite areas associated with sinkhole development are presented here. TerraSAR-X was tasked to acquire data from January 2015 – January 2016 with short revisit times (generally 11 days but up to 77 days) resulting in 21 interferometrically compatible images. Sequential image pairs were processed through conventional DInSAR processing workflows. Three previously unknown deformation basins were detected, one of which could be confirmed in the field. This confirmed subsidence ultimately led to a burst high-pressure water supply pipeline. The detected deformation basins were between 40 m and 100 m in diameter. The maximum displacement was measured as 7 cm over 55 days. Deformation before the infrastructure damage could be detected up to 6 months in advance. The detection could have provided a viable early warning to landowners who were unaware of the subsidence. Another event that remains unconfirmed by in-situ observations was characterised by unexplained ground uplift.

These results indicate that high-resolution X-band DInSAR is able to monitor dolomite-induced instability in an urban environment. Although some deformation features were observed, seven sinkhole events occurred in the observation period for which no DInSAR deformation could be detected. Two factors were identified to be major challenges to the detection of precursory deformation, 1) the minimum detectable scale of deformation and 2) coherence loss due to temporal decorrelation, mainly because of ground disturbance during large rainfall events. The physical presence of precursors is further discussed as a fundamental limitation to early warning systems. Future research should explore ultra-high resolution sensors and consider advanced DInSAR processing techniques to overcome coherence limitations. This research supports the statement that DInSAR could contribute to an operational early warning system and further recommends that local geohazard policy should consider its capabilities.

Keywords: Remote sensing, SAR, Interferometry, TerraSAR-X, Sinkhole, Precursor, Dolomite, Gauteng

Opsomming

Differensiële Sintetiese Apertuur Radar Interferometrie (DInSAR) is 'n bevestigde grond vervorming monitering tegniek en navorsing in hierdie tesis ondersteun hierdie tegnologie as 'n belangrike instrument vir 'n operasionele sinkgat waarskuwingstelsel in Suid-Afrika. Sinkgate is 'n onvoorspelbare aard-gevaar wat lewe en eiendom in gevaar stel in dolomitiese terreine. Dit is 'n groot bedreiging in Gauteng, die mees bevolkte en verstedelikte provinsie in Suid-Afrika. Meer as 3000 gebeurtenisse is al hier aangeteken in die laaste 50 jaar en het gelei tot die verlies van 37 lewens en meer as 1,2 miljard Rand se skade aan eiendom. Daar is ‘n behoefte aan maatreëls om risiko te verminder in gebiede wat reeds ontwikkel is. Sulke maatreëls sal ook toelaat dat verdere ontwikkeling kan plaasvind in gebiede wat geneig is tot sinkgat vorming. Kleinskaalse oppervlak vervorming is dikwels teenwoordig voor die ineenstorting van 'n sinkgat. Daar is egter nog nie veel bekend oor hierdie verskynsel nie, deels as gevolg van die onvoorspelbare aard van sinkgate en die uitdagings om groot gebiede vir kleinskaalse (<10cm) vervorming te moniteer. Nogtans word dit veronderstel dat die teenwoordigheid van voorloper oppervlak vervorming benut kan word om vroeë waarskuwingstelsels te ontwikkel om verdere skade te beperk. Ruimte gebaseerde DInSAR is in staat om kleinskaalse oppervlak vervorming oor groot gebiede te monitor en kan benut word om voorlopers van sinkgat ontwikkeling op te spoor en te meet. Onlangse suksesvolle gevallestudies ondersteun hierdie tegniek vir sinkgat voorloper opsporing maar operasionele beperkings is nog nie bepaal nie.

Die eerste resultate van DInSAR-gebaseerde monitering poging van dolomiet areas wat verband hou met sinkgat ontwikkeling word hier aangebied. TerraSAR-X is getaak om data te verkry vanaf Januarie 2015 - 2016 met kort herbesoek tye (oor die algemeen 11 dae, maar tot 77 dae) wat gelei het tot 21 interferometriese versoenbare beelde. Opeenvolgende beeld pare is verwerk deur middel van konvensionele DInSAR metodes. Drie voorheen onbekende vervorming areas is opgespoor, waarvan een in die veld bevestig is. Hierdie bevestigde grondvervorming het uiteindelik gelei tot die bars van ‘n hoë druk watervoorsiening pyplyn. Die vervormende areas wat ontdek is, was tussen 40 m en 100 m in deursnee. Die maksimum verplasing wat gemeet was, was 7 cm oor 55 dae. Vervorming kon opgespoor word tot 6 maande voor die infrastruktuur skade. Die opsporing kon 'n lewensvatbare vroeë waarskuwing gebied het aan grondeienaars wat nie bewus was van die versakking nie. Nog 'n gebeurtenis, wat nie bevestig is deur in-situ waarnemings nie, was gekenmerk deur onverklaarbare grond opheffing.

Hierdie resultate dui daarop dat hoë-resolusie, X-band, DInSAR in staat is om onstabiliteit, as gevolg van dolomiet, te monitor in 'n stedelike omgewing. Maar, alhoewel sommige vervorming eienskappe wel waargeneem is, het daar sewe sinkgat gebeure plaasgevind gedurende die waarneming tydperk waarvoor geen vervorming opgespoor kon word nie. Twee faktore is geïdentifiseer as groot uitdagings vir die opsporing van voorlopers van vervorming, insluitend 1) die minimum waarneembare skaal van vervorming en 2) verlies van sein korrelasie as gevolg van oppervlak verandering - hoofsaaklik as gevolg van grond versteuring tydens swaar reënval tydperke. Die fisiese voorkoms van sinkgat voorlopers word verder bespreek as 'n fundamentele beperking vir vroeë waarskuwing stelsels. Toekomstige navorsing behoort ultra-hoë resolusie sensors te verken en moet oorweeg om meer gevorderde DInSAR verwerking tegnieke te gebruik om korrelasie beperkinge te bowe te kom. Hierdie navorsing ondersteun die stelling dat DInSAR kan bydra tot 'n operasionele vroeë waarskuwingstelsel en beveel verder aan dat plaaslike aard-gevaar beleid die nuwe tegnologie in ag moet neem.

Trefwoorde: Afstandswaarneming, SAR, Interferometrie, TerraSAR-X, Sinkgat voorloper, Dolomiet

List of publications

Theron A, Engelbrecht J, Kemp J, Kleynhans W, Turnbull T 2016. *Detection of sinkhole precursors through SAR interferometry: first results from South Africa.* Proceedings of the IEEE International Geoscience and Remote Sensing Symposium held 10-15 July, Beijing, China.

Theron, A. Engelbrecht, J. and Kemp, J. 2016. *Potential of sinkhole precursor detection through interferometric SAR.* Proceedings of the 35th International Geological Congress held 27 August to 4 September 2016, Cape Town, South Africa.

Theron A, Engelbrecht J, Kemp J, Kleynhans W, Turnbull T (under review). Detection of sinkhole precursors through SAR interferometry: radar and geological considerations. IEEE *Geoscience and Remote Sensing Letters.*

Acknowledgements

I would like to thank the following people and institutions for their contribution towards this research:

- The CSIR Meraka institute for generous funding and providing me with the opportunity to attend various conferences and training courses.
- My supervisors, Dr Jeanine Engelbrecht (CSIR Meraka Institute) and Jaco Kemp (Stellenbosch University) for their patient and expert supervision, support and encouragement during this exciting project.
- Dr Waldo Kleynhans (CSIR Meraka Institute) and Terrence Turnbull (South African Air Force) for their efforts in acquiring the SAR data.
- The wonderful support staff at the CSIR for taking much of my administrative tasks into their own capable hands, including Elsie Mosenye, Tumi Serapane and the late Pamela Maseko.
- The Council for Geoscience for providing the sinkhole inventory, especially to Samantha Constantinou and Tharina Oosthuizen for valuable expert knowledge and fieldwork.
- The Centre for Geographical Analysis at the Stellenbosch University for providing the SUDEM elevation model.
- The South African Weather Service for providing rainfall data over the study area.
- The TerraSAR-X/TanDEM-X satellites and everyone responsible for their great performance.
- Mendeley, Dropbox, Grammarly, Google scholar, GAMMA and even MS Word – finally software is becoming more useful than frustrating.
- My family for their patience and backing my inevitable journey into science - Particularly my father (Francois), for teaching me that curiosity is sometimes more important than calculation, my mother (Miemie) for showing me the value in never giving up, and my siblings (Mercia and Bernie) for keeping life interesting with their African adventures.
- Simone Pretorius for the incredible sacrifices she made and for her unwavering support and inspiration while also completing her thesis. More importantly, for reminding me to keep my eyes on the summits – those above and others out of sight.
- The internal and external examiners for their valuable assessment and time.

Table of contents

Abstract ii

Opsomming iii

List of publications iv

Acknowledgements v

Table of contents vi

List of tables ix

List of figures x

Acronyms and abbreviations xiii

Definition of key terms xiv

Chapter 1 Introduction 1

1.1 Background to SAR and DInSAR 1

1.2 Research problem 3

1.3 Research goals and objectives 4

1.4 Methodology and research design 4

1.5 Introduction to the study area 6

1.6 Chapter overview 8

Chapter 2 Literature Review 9

2.1 Sinkholes as a geohazard 9

2.1.1 Overview of sinkhole formation 9

2.1.2 Precursory deformation 11

2.1.3 Sinkhole geology in the Gauteng province 12

2.1.4 Sinkhole risk management in the Gauteng province 14

2.1.5 Current sinkhole monitoring techniques 16

2.2 DInSAR for measuring surface deformation 18

2.2.1 Synthetic Aperture Radar 18

2.2.2 SAR interferometry 19

2.2.2.1 Factors controlling differential interferometric phase 20

2.2.2.2 From differential phase to displacement 22

2.2.2.3 Coherence 23

2.2.2.4 Accuracy assessment 24
2.2.3 Advanced DInSAR techniques 24
2.2.3.1 Polarimetric interferometry (PolInSAR) 25
2.2.3.2 Small Baseline Subset (SBAS) 25
2.2.3.3 Persistent scatterer interferometry (PSInSAR) 26
2.2.3.4 Limitations to advanced DInSAR 27
2.2.4 The use of interferometry in southern Africa 28
2.2.5 Interferometric detection of sinkhole precursors 30
2.3 SAR system considerations 36
2.3.1 Wavelength 36
2.3.2 Acquisition modes (spatial resolution and swath size) 38
2.3.3 Revisit time (temporal baseline) 38
2.3.4 Polarisation 39
2.3.5 Line of sight (LOS) and incidence angle 40
2.3.6 SAR platforms 40
Chapter 3 Data and methods 42
3.1 SAR data and processing 42
3.1.1 SAR data 42
3.1.2 Differential interferometry processing 44
3.2 Ancillary data 47
Chapter 4 DInSAR results 51
4.1 Interpretation of DInSAR outputs 51
4.2 Sinkhole inventory events and DInSAR observations 53
4.2.1 Event A1 53
4.2.2 Event A2 55
4.2.3 Event A3 57
4.2.4 Event A4 59
4.2.5 Event A5 61
4.2.6 Event A6 65
4.2.7 Event A7 66

4.3 DInSAR deformation observations 68
4.3.1 Event B1 69
4.3.1.1 Basin 1 69
4.3.1.2 Basin 2 73
4.3.1.3 Further investigation and sinkhole event 75
4.3.2 Event B2 78
4.3.3 Event B3 81
Chapter 5 Discussion of DInSAR for sinkhole precursor detection 86
5.1 SAR system and processing considerations 86
5.1.1 Resolution and swath width 87
5.1.2 Wavelength 88
5.1.3 Temporal baseline 89
5.1.4 Incidence angle and LOS 90
5.1.5 Coherence 90
5.2 Physical considerations 93
5.2.1 Presence of precursors 94
5.2.2 Physical characteristics 95
5.2.3 Seasonality 97
5.2.4 Field evidence 97
Chapter 6 Conclusion 100
6.1 Summary of findings 101
6.1.1 Objective 1 101
6.1.2 Objective 2 101
6.1.3 Objective 3 101
6.1.4 Objective 4 103
6.2 Limitations to the study 104
6.3 Recommendations for further research 105
6.4 Concluding remarks 107
References 109

List of tables

Table 2.1 Details of the most important SAR systems available for SAR research (adapted from Ozden et al. (2016)). 41

Table 3.1 The date and interferometric properties of the SAR images acquired for the study. 44

Table 3.2 Sinkhole inventory for the study area between January 2015 and February 2016. 48

Table 4.1 A summary of the physical dimensions of the first basin of Event B1 detected between June and August 2015 along with appropriate interferometric properties. 71

List of figures

Figure 1.1 Overall research design diagram. 5

Figure 1.2 The study area indicating the location of known dolomite land, important place names, the weather station and the footprint covered by TerraSAR-X. The enlarged map area is shown as a red block in the map insert. 7

Figure 2.1 A widely used sinkhole classification system whereby a sinkhole is classified by its geological conditions (row) and its subsidence process (column) (adapted from Gutiérrez et al. (2014)). 10

Figure 2.2 Diagram illustrating the formation of a cover-collapse sinkhole due to subsurface erosion. Note the surface deformation due to underground cavity migration before the sinkhole forms which referred to as precursory deformation (indicated by the red arrow in block B). 11

Figure 2.3 The geometry of repeat-pass SAR interferometry illustrating the different baselines. Note the exaggerated difference in incidence angles between acquisitions. In reality these are approximately equal due to the large distance between the satellite and the earth's surface. 20

Figure 3.1 Automated processing workflow for two-pass differential interferometry used during this study. 45

Figure 3.2 A timeline of data acquisitions and sinkhole events. 49

Figure 4.1 An example of baseline-dependant fringe pattern on interferograms characteristic of topographical phase residue (A, B, C & D). In this case, the fringe pattern is due to topographical variation not modelled in the DEM (F). Inspection of the aerial imagery shows that this is the result of a mine tailings dam (E). 52

Figure 4.2 Interferograms of data available prior to, and during, event A1's sinkhole formation show no deformation fringes (A & B: differential interferograms; C & D: associated coherence maps; E: aerial photo). 54

Figure 4.3 Aerial imagery captured after the sinkhole event A1 formed showing the extensive excavation works done on the surrounding area following the sinkhole event. 55

Figure 4.4 Aerial imagery indicating the location of sinkhole event A2 with a red circle. 56

Figure 4.5 Interferograms for the area round event A2 with the sinkhole and its approximate extent indicated with a black circle. 57

Figure 4.6 Aerial imagery indicating the approximate location of sinkhole event A3 (red star). The SAR line of sight (LOS) direction is also provided. 58

Figure 4.7 Interferograms for the area round event A3 with the approximate location reported as the black star. 59

Figure 4.8 Aerial imagery indicating the location of sinkhole event A4. The SAR line of sight (LOS) direction is also provided. 60

Figure 4.9 Interferograms for the area round event A4 with the approximate location reported as the black star. 61

Figure 4.10 (A) Field photograph of event A5 showing the sinkhole and resulting damages to the cell phone tower infrastructure. (B) An aerial image of the area where the sinkhole occurred 62

Figure 4.11 Interferogram time series over the entire study period from the 29th January 2015 to the 27th January 2016. 63

Figure 4.12 A time series of all the coherence images over the approximate location of event A5 showing the loss of coherence associated with the sinkhole can be seen on the final two images. 64

Figure 4.13 (A) Aerial imagery indicating the location of sinkhole event A6 as well as a field photograph of the sinkhole (B). 65

Figure 4.14 Interferograms for the area round event A6 with the sinkhole and its approximate extent indicated with a black circle. 66

Figure 4.15 Aerial imagery indicating the location of sinkhole event A7. The SAR line of sight (LOS) direction is also provided. 67

Figure 4.16 Interferograms for the area round Event A7 with the sinkhole indicated with a black star, the exact location is uncertain, however. 68

Figure 4.17 Aerial imagery indicating the approximate maximum extent and location of the deformation basins and pipe (blue line) discussed as event B1. 69

Figure 4.18 Interferograms for the area round event B1 with the subsidence and its approximate extent indicated with a black circle. 70

Figure 4.19 Displacement maps of the deformation event B1 derived from three interferograms as well as the sum of the three maps showing the total deformation detected over the period. 72

Figure 4.20 A three-dimensional representation of the total deformation detected over event B1. 73

Figure 4.21 Interferograms (left) and vertical displacement maps (right) of the second deformation detection period of event B1. 74

Figure 4.22 A time series of all the coherence images showing the first basin of event B1 (red circle 76

Figure 4.23 Field observations of Event B1. 78

Figure 4.24 High-resolution aerial image indicating the location and approximate extent of deformation event B2. 79

Figure 4.25 Interferograms for the area round event B2 with the subsidence and its approximate extent indicated with a black circle. 80

Figure 4.26 Vertical displacement maps of the area around Event B2, generated from the interferometric pairs where deformation was detected. 81

Figure 4.27 High-resolution aerial imagery indicating the location of event B3 between two roadways. 82

Figure 4.28 Interferograms for the area round event B3 with the subsidence and its approximate extent indicated with a black circle. 83

Figure 4.29 Vertical displacement maps of Event B3. 84

Figure 4.30 Field photograph of the area where the uplift was detected for Event B3. 85

Figure 5.1 Comparisons between globally averaged interferometric coherence and factors that may influence coherence namely A) perpendicular baseline, B) temporal baseline, C) Enhanced Vegetation Index (EVI) and D) rainfall accumulation. 91

Figure 5.2 Competent land cover types capable of resisting gradual subsidence leading to sinkhole events not preceded by precursory deformation 94

Acronyms and abbreviations

APS	Atmospheric Phase Screen
B_{perp}	Perpendicular baseline
B_{temp}	Temporal baseline (SAR revisit time)
CGS	Council for Geoscience
CoT	City of Tshwane
DEM	Digital Elevation Model
DInSAR	Differential Interferometric SAR
DLR	Deutsches Zentrum für Luft- und Raumfahrt (German Aerospace Center)
ESA	European Space Agency
EVI	Enhanced Vegetation Index
GB-DInSAR	Ground-based Interferometric SAR
GIS	Geographic Information System
HH/VV/HV/VH	SAR Polarisations (H=Horizontal, V=Vertical)
LiDAR	Light Detection And Ranging
LOS	Line Of Sight
MDDG	Maximum Detectable Deformation Gradient
NASA	National Aeronautics and Space Administration
PolInSAR	Polarimetric Interferometric SAR
PSInSAR	Persistent Scatterer Interferometric SAR
Radar	Radio Detection And Ranging
SANS	South African National Standard
SAR	Synthetic Aperture Radar
SAWS	South African Weather Service
SFM	Structure from motion
SLC	Single Look Complex (focussed complex valued SAR image)
SNR	Signal to Noise Ratio
SRTM	Shuttle Radar Topography Mission
SUDEM	Stellenbosch University Digital Elevation Model
TSX	TerraSAR-X
UAV	Unmanned Aerial Vehicle
WAD	Weathered Altered Dolomite

Definition of key terms

Amplitude	A measure of the intensity of the returning Radar pulse.
Azimuth	Refers to the coordinate axis horizontal to the SAR flight direction.
Coherence	A measure of decorrelation of the phase within a SAR interferogram.
Dolomite	Sedimentary calcium magnesium carbonate rock, which is composed predominantly of the mineral dolomite, very prone to sinkholes.
Dolomite Land	Sinkhole-prone areas where dolomite occurs at the sruface or at shallow depth.
Doppler effect	The change in frequency of a wave for an observer moving relative to its source.
Fringe	Phase change over an interferogram from +π and –π.
Hazard	Situation that poses a threat to life, health, property or the environment.
Interferogram	Resulting image after the complex combination of two SAR images.
Interferometry	Technique in which electromagnetic waves are superimposed in order to extract information (principally change in range for SAR imaging).
Karst	Landscapes where the bedrock compromises of highly soluble evaporite or calcium carbonate rock characterised by sinkholes.
Persistent scatterer	A pixel that remains coherent over an interferogram time series (also refers to physical objects that maintain coherence).
Phase	The phase of a wave, measured in degrees, indicating the current position of the wave relative to a reference position.
Polarisation	Oscillation direction of electromagnetic waves (generally describing either horizontal or vertical for SAR imaging).
Range	Distance from the SAR platform to the ground (also refers to the coordinate axis perpendicular to the SAR flight direction).
Resolution	Mainly refers to pixel spacing in this thesis.
Risk	Risk is the potential of gaining or losing something of value. Hazard and possibility interact to create risk.
Risk avoidance	Measures taken to avoid exposure to a risk.
Risk mitigation	Measure taken to reduce harm in case of a risk occurring.
Sinkhole	Depression or hole in the ground that is caused by some form of collapse of the surface layer.
Sinkhole precursor	Early warning sign, particularly in the form of subsidence, leading up to sinkhole collapse.
Temporal resolution	Time (in days) between SAR acquisitions forming in interferometric pair.
TerraSAR-X	SAR satellite used in the study (in formation with its twin, TanDEM-X).
Wavelength	The distance between successive crests of an electromagnetic wave.
X-, C- & L-band	Relevant Radar wavelength determinations (~3 cm, ~5.6 cm, ~23.5 cm).

Chapter 1
Introduction

Sinkholes are a geological hazard associated with karst and evaporite terrain that can cause damage to infrastructure and a loss of life globally (Guerrero et al. 2008) including certain areas of South Africa (Buttrick et al. 2011; De Waele et al. 2011; Potgieter, Pretorius & Walt 2016). The most affected area in South Africa is its most densely populated and urbanised province, Gauteng. Here more than 2.5 million people live and continue to develop on sinkhole-prone dolomitic land (Trollip 2006). Sinkhole events are challenging to predict but there is often precursory ground deformation months or even years before ultimate collapse (Nof et al. 2013; Chang & Hanssen 2014; Jones & Blom 2015; Intrieri et al. 2015; Kim, Lu & Degrandpre 2016). Space-borne radar interferometry is one of the latest developments in the field of deformation monitoring and has the potential to detect such precursory deformation. These detections can be incorporated into a cost effective sinkhole early warning system (Joyce et al. 2009; Vaccari et al. 2013; Stevanovic et al. 2015; Intrieri et al. 2015; Bruckno et al. 2015; Ozden et al. 2016). Such a system will greatly improve dolomite risk management in Gauteng, and has the potential to be used in other sinkhole-prone areas of the world. However, only a few successful detections of precursory deformation through interferometry have been reported on in literature globally. Publications on negative results investigating the causes for non-detections are also limited (Baer et al. 2002; Paine et al. 2012; Rucker et al. 2013). As a result, there is limited understanding of the capabilities and limitations of DInSAR when applied to sinkhole early warning. Furthermore, the conditions under which sinkholes develop vary depending on the local conditions and geological environment. Therefore, findings on the detection of sinkhole precursors in one geographical region may not necessarily be applicable in a different region. Research on the nature of precursory deformation and its detection using DInSAR in South African conditions is required.

This chapter will provide and introduction to the general concept of radar interferometry and its applications, globally as well as in South Africa, with a brief summary of the state of the art for sinkhole precursor detection (Section 1.1). This is followed by a motivation for the study and the selected methods (Section 1.2), leading to the research question and the aims and objectives chosen for addressing the question (Section 1.3.). The research methodology is then provided (Section 1.4). The study area is finally introduced (Section 1.5).

1.1 Background to SAR and DInSAR

Spaceborne radar interferometry is based on Synthetic Aperture Radar (SAR) data. SAR is an active microwave imaging system with cloud-penetrating capabilities (Massonnet & Feigl 1998). SAR imaging is set apart from other remote sensing imaging techniques as it captures not only the intensity of the return signal but also its phase. This phase information is used in an image

processing technique called Differential Interferometry (DInSAR) to derive surface displacement measurements. The extraction of surface deformation from phase is based on the principle that the radar phase is directly related to the two-way travel distance between the satellite and the surface. The phase information of the same area over different times can be compared, resulting in an interferogram. The interferogram can be adjusted to compensate for phase contributions due to topography and other external influences, to provide a measure of surface displacement between image acquisitions (Ferretti et al. 2007). DInSAR has matured as a technology and has proven to be capable of measuring ground deformation with sub-centimetre accuracy over large areas and timescales (Ferretti et al. 2015).

Spaceborne SAR has been widely used, and reviewed in literature, for its ability to monitor ground deformation with millimetre precision through differential interferometry (Crosetto, Arnaud & Duro 2003; Joyce et al. 2009; Zhou, Chang & Li 2009; Prati, Ferretti & Perissin 2010; Sansosti et al. 2014; Ferretti et al. 2015). Original applications of DInSAR techniques in the 1990s involved the study of earthquake deformation, such as the seminal 1993 Nature article: “The displacement field of the Landers earthquake mapped by radar interferometry” (Massonnet et al. 1993). Volcanic activity of Mount Etna (Bonforte et al. 2011), landslides (Dehghani 2016), ice sheet motion in Antarctica (Sansosti et al. 2014), and mining subsidence (Engelbrecht et al. 2014). The focus of applications has not shifted much from earlier studies as earthquake, volcano and mining deformation, ground subsidence and slope instabilities are still the most important applications for SAR interferometry.

The technology has recently matured through advanced processing techniques and new sensor development to provide continuously improving results when applied to classic as well as novel applications (Sansosti et al. 2014; Ferretti et al. 2015; Voigt et al. 2016). Building and infrastructure monitoring have become an important new application area for DInSAR specifically due to the availability of high-resolution SAR systems (Galve, Castañeda & Gutiérrez 2015; Ozden et al. 2016). In South Africa, DInSAR was first tested in the late 1990s (Doyle, Inggs & Hartnady 1997; Doyle, Stow & Inggs 2001) and is currently used mainly for monitoring deformation due to mining activities (Engelbrecht & Inggs 2013; Engelbrecht et al. 2014). There is, therefore, potential to exploit SAR interferometry for new applications over South Africa, as well as the African continent as a whole.

The detection of precursors to sinkhole collapse is a novel application of SAR interferometry and a substantial body of research is yet to be established. Radar interferometry has not yet been widely adopted for precursory sinkhole detection due to the typically high cost of SAR imagery combined with the low frequency, small scale and unpredictability of sinkhole collapse (Gutiérrez et al. 2014; Intrieri et al. 2015). However, recent advances in the resolution of the sensors (Sansosti et al. 2014) and the development of techniques applied to the data (Prati, Ferretti & Perissin 2010) are enabling research into this field. Successful case studies report that this application has the

potential of achieving reliable and accurate results (Jones & Blom 2013; Nof et al. 2013; Chang & Hanssen 2014). The hypothesis that measurable precursory deformation occurs before sinkhole collapse is vital to the development of an early warning detection system and can only be tested empirically (Augarde, Lyamin & Sloan 2003). Here, the new generation of radar satellites and interferometric techniques are proving to be an ideal tool for gathering evidence. Their large synoptic view and frequent orbital revisit times are providing data that is often superior to ground-based observations (Engelbrecht & Inggs 2013; Chang & Hanssen 2014). DInSAR has furthermore been shown to be cost effective as a tool for monitoring urban infrastructure when compared to *in situ* methods (Ozden et al. 2016).

1.2 **Research problem**

Sinkholes pose a threat to people and property in many areas of the world (Guerrero et al. 2008), as well as in urban areas in South Africa (Buttrick et al. 2011; Richardson 2013). Dolomite underlies large areas of economically important land in South Africa. Decades of rapid economic and social development in this region implies that, in places, development took place before proper risk mitigation or avoidance measures could be implemented (Oosthuizen & van Rooy 2015). Furthermore, urban expansion is driving new developments over susceptible areas (Watermeyer et al. 2008), increasing the risk for future sinkhole formation (Gutiérrez et al. 2014). Due to the risks associated with sinkhole development, there is a need to develop a sinkhole early warning system using appropriate technology (Joyce et al. 2014). There is currently no operational way of receiving a reliable advanced warning of sinkhole formation despite the fact that there is a pressing need and global scientific interest (Joyce et al. 2014; Gutiérrez et al. 2014; Galve, Castañeda & Gutiérrez 2015). However, precursory ground deformation has been recorded prior to sinkhole formation and detecting such subsidence prior to sinkhole development may be the key to an early warning system (Nof et al. 2013).

DInSAR techniques provide the ability to map the small-scale movement of the earth surface. International research has indicated that the detection of precursors to sinkhole collapse is possible and cost effective with SAR interferometric techniques. However, there are limited case studies and these are based on a small number of sinkhole events (Nof et al. 2013; Chang & Hanssen 2014; Jones & Blom 2015; Intrieri et al. 2015; Kim, Lu & Degrandpre 2016). There is also a lack of literature on the nature of precursory deformation in general (Parise & Lollino 2011).

The South African development framework for dolomitic ground (discussed in Section 2.1.4) and local research acknowledges the need for sinkhole activity monitoring in high-risk areas (SABS 2012; Richardson 2013). However, the potential for SAR interferometry for monitoring deformation prior to sinkhole events has not been recognised by these authors. Current South African sinkhole mitigation policies have shown to be effective in reducing sinkhole frequency and resulting damages, yet there is no pro-active monitoring system for risk management. A lack of pro-active

dolomite risk management is not only a problem in developing countries such as South Africa but also in more developed countries (Potgieter, Pretorius & Walt 2016).

SAR Interferometry, as part of a pro-active risk management strategy, therefore has the potential to reduce the risk to sinkhole formation. However, the core question of whether SAR interferometry can reliably detect precursors to sinkhole formation remains largely unknown. Investigating this question will contribute to the growing international body of knowledge regarding DInSAR precursor detection in various environments and further the state of DInSAR application in southern Africa.

1.3 Research goals and objectives

This thesis aims to test whether ground deformation prior to sinkhole formation in Gauteng, South Africa, can be detected using SAR interferometry. Following this overall aim, the research will focus on answering the question:

Can X-band differential SAR interferometry detect ground deformation prior to sinkhole development and provide an early warning to sinkhole formation in Gauteng?

To answer the research question, this research aims to address the following objectives:

1. Perform DInSAR analysis to identify ground deformation in the study area;
2. Compare DInSAR results to known sinkhole events recorded in the study period;
3. Assess the limitations inherent to the data and processing techniques;
4. Identify considerations for detection related to the characteristics of sinkholes and their precursors in the study area.

1.4 Methodology and research design

An empirical research approach was taken to answer the overall research question, identified through the literature review. The overall research design diagram is shown in Figure 1.1. Primary data were quantitative and consisted of ongoing SAR acquisitions throughout the study period. Processing of these data is elaborated on in Chapter 3. Ancillary data, both descriptive and numerical in nature, were collected from various sources and used mainly to aid interpretation of the primary data processing results. The DEM is the exception as it was used for both primary data processing and result interpretation. Data interpretation and identification of deformation for meeting Objective 1 was based on visual analysis of the processing results using established principles (Massonnet & Feigl 1998). Comparison of DInSAR results to the sinkhole inventory for meeting Objective 2 was mainly qualitative due to the lack of reliable measurements in the inventory. Consequently, comparisons were based primarily on whether detections were successful or not. Both quantitative and qualitative approaches were used to meet Objectives 3 and 4.

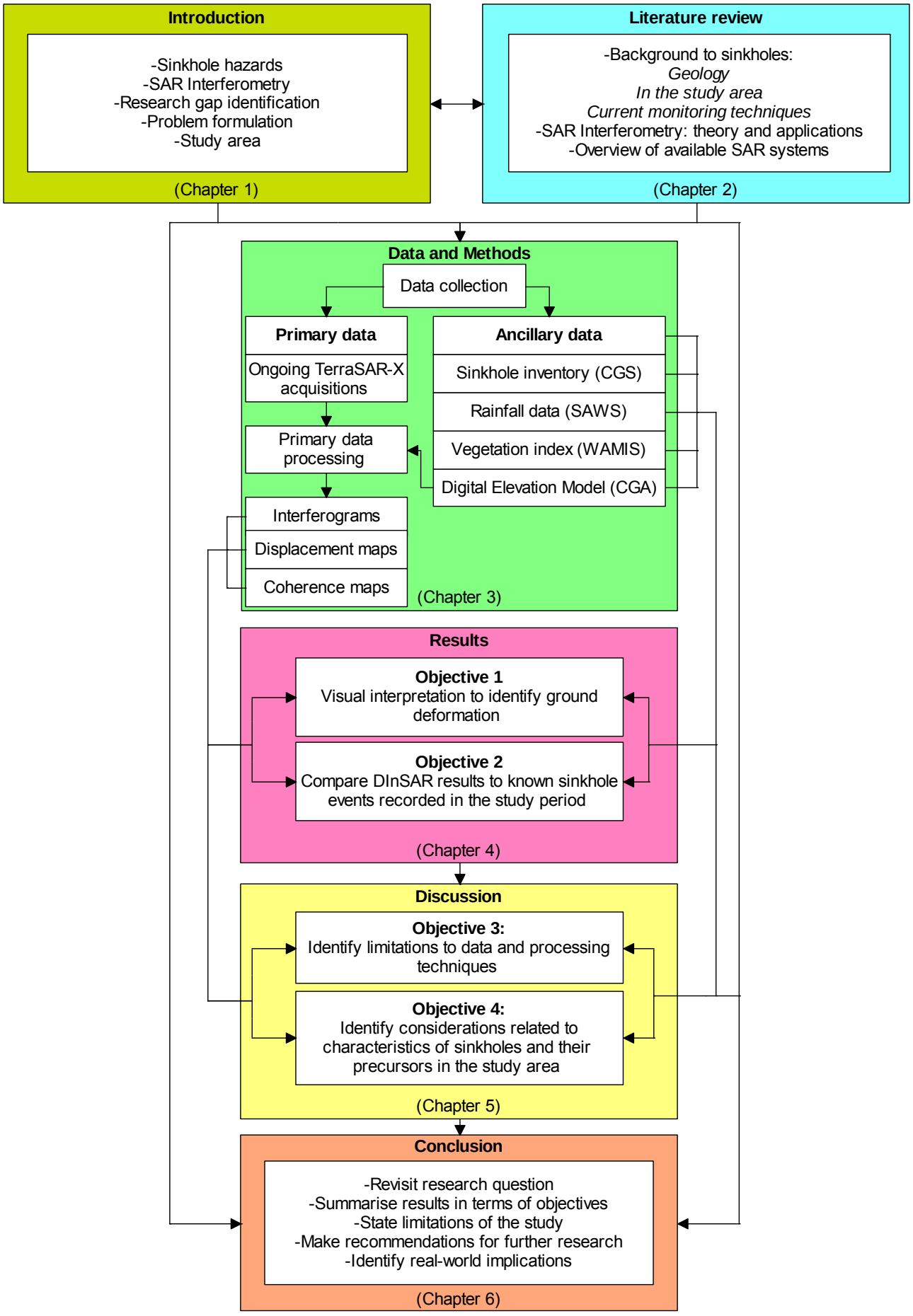

Figure 1.1 Overall research design diagram.

1.5 Introduction to the study area

The study area is shown in Figure 1.2 and is located in the Tshwane metropolitan municipality, which occupies the north of the Gauteng province of South Africa. The study area is defined by the SAR image footprint and includes the city of Pretoria and the Centurion area to the south. This area is ideal for the detection of sinkhole precursors due to up-to-date reports of ground deformation in some parts of the study area as well as a historical record of sinkhole activity (Richardson 2013). The area has a complex urban built-up and peri-urban character. Large areas of known dolomitic ground are present (red areas in Figure 1.2) which often intersect with built-up areas (shown in grey in Figure 1.2). Sinkhole formation in Gauteng causes significant financial losses annually due to high levels of human activity and development taking place above susceptible geology (Trollip 2006). More than 4 million South Africans live or work on dolomite land and, in extreme cases, entire communities had to be relocated due to the hazard (Buttrick et al. 2011). Sinkholes are common in the area and there is evidence of ground deformation activity in the form of infrastructure and building damage, tension cracks and documented sinkhole collapse events. Underground cavities, which lead to sinkhole formation, are so widespread in the area that they are assumed to be present during geotechnical investigations even if they are not detected by drilling (Buttrick et al. 2011). There has been a renewed concern surrounding dolomitic land in Gauteng after sinkholes were identified to be one of the biggest hazards to the recently developed Gautrain rapid rail infrastructure (Jaros, James & Gewanlal 2009; Sartain et al. 2011; Richardson 2013).

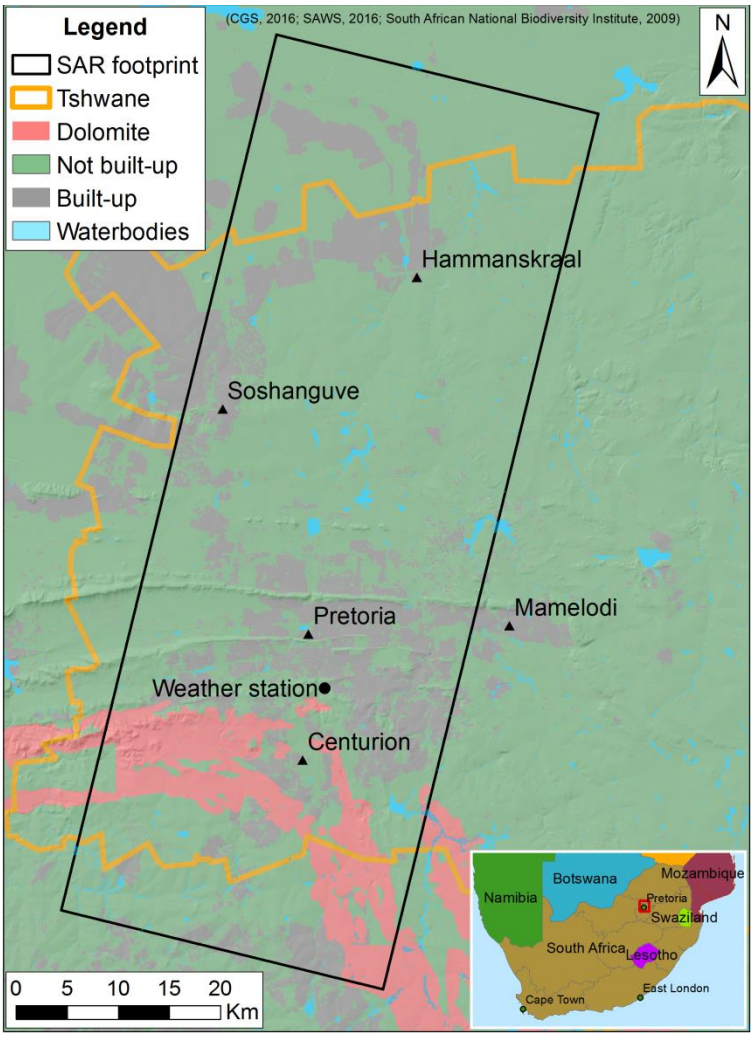

Figure 1.2 The study area indicating the location of known dolomite land, important place names, the weather station and the footprint covered by TerraSAR-X. The enlarged map area is shown as a red block in the map insert. Note that the Gauteng province shares its northern and western boundaries with the corresponding borders of the Tshwane metropolitan municipality shown in orange.

Sinkhole hazard areas in the Gauteng province can be separated into three distinct areas, Tshwane (in particular areas south of Pretoria such as Centurion), Ekurhuleni, and the West Rand. An analysis of historical records for all these areas, up to 2011, was recently conducted (Richardson 2013) and the results revealed that approximately 3048 events (sinkholes, subsidence and cracks) occurred in the last 60 years. These events were found to be occurring regularly, yet a decreasing frequency was noted over the last decade. Sinkhole occurrences in the West Rand and Tshwane were attributed to the ingress of water while in Ekurhuleni most of the events were due to dewatering. The majority of the sinkholes were less than 15 m in diameter.

In the Tshwane area alone, there were 1365 recorded sinkhole events between 1960 and 2011, occurring at a historical rate of 27 events per annum. The rate of sinkhole occurrence is 0.13 sinkholes/km^2/year and they have been found to form mainly in highly developed areas (Richardson 2013). The earliest recorded event in the Tshwane area took place in 1938. Within Tshwane, an area known as Centurion exhibited a high probability of sinkhole events occurring

over a relatively small area (~ 1 600 Ha). In Centurion, more than 119 sinkhole events have been recorded at a density of 7.2 sinkholes per square kilometre (Oosthuizen & van Rooy 2015).

Sinkholes result in major economic damages and the loss of life in Gauteng. At least 39 deaths can be attributed to sinkholes and evidence shows that 35% of events impact manmade structures with a total reported property damage now exceeding R1.2 Billion (Trollip 2006; Buttrick et al. 2011). Sinkholes occurring in Centurion during the period 1984 - 2004 analysed by Buttrick et al. (2011) resulted in damage to buildings with an estimated total loss of US $250 million, or $80 000 per event (unconverted currency quoted directly from the paper). Poor communities, already settled in high-risk areas of Gauteng, are especially vulnerable to sinkhole development and often cannot afford geotechnical site investigations or enhanced building standards. Resettlement of these communities is challenging due to negative associations with resettlement because of past discriminatory apartheid policies (Potgieter, Pretorius & Walt 2016).

Sinkhole formation in the study area has been associated with rainfall, and more events occur in months or years with high rainfall. However, the two variables show a statistically poor fit and one cannot be used to predict the other (Richardson 2013). The area receives an average of 600 – 800 mm of rain per year that falls predominantly in the summer between October and March as high-intensity convectional showers (Richardson 2013). This is the main growing season for the vegetation in the area. However, the vegetation here is not necessarily dependent on rainfall (White et al. 2002). However, 2015 was a dry year in southern Africa, likely due to an intense El Nino event present throughout the year (FEWSNET 2016). Only 392mm of rain was recorded during 2015 at a rainfall station central to the study area, in comparison to the long-term average of 600 mm – 800 mm.

1.6 **Chapter overview**

An overview of the current state of the art on sinkhole formation and DInSAR for deformation monitoring is presented in Chapter 2. The data and research methods are presented in Chapter 3. Chapter 4 provides the results of DInSAR monitoring of the study area and the discussion of the results is presented in Chapter 5. Concluding remarks and recommendations are presented in Chapter 6.

Chapter 2
Literature Review

The following chapter provides an overview of sinkhole hazards (Section 2.1.1) with a focus on the mechanisms of sinkhole formation and precursory deformation (Section 2.1.2). Properties and management of sinkholes in the Gauteng province (Section 2.1.3 and 2.1.4) and currently available monitoring methods (Section 2.1.5) are then discussed. The concept of radar interferometry for surface deformation monitoring will then be introduced (Section 2.2.2) before discussing the DInSAR state of the art in terms of technical advances (Section 2.2.3), South African examples (Section 2.2.4) and sinkhole precursor detection (Section 2.2.5). Important considerations for SAR platform selection in the context of sinkhole precursor detection will finally be presented (Section 2.3).

2.1 Sinkholes as a geohazard

This first section discusses the geological aspects of sinkhole formation, risk management and ground surface monitoring in the context of the study area.

2.1.1 Overview of sinkhole formation

Sinkholes occur worldwide due to the cavernous nature of underlying rock and are a characteristic feature of karst landscapes. Karst landscapes are defined as areas where the bedrock comprises of highly soluble evaporite or calcium carbonate rock, such as dolomite or limestone (Buttrick et al. 2011). Karst landscapes often have a visible surface component and a more important invisible subsurface component. Underground, a complex three-dimensional drainage pattern is found due to the high rates of dissolution dominating over mechanical erosion (Gutiérrez et al. 2014). Dissolution due to slightly acidic groundwater leads to subterranean caverns and conduits to form, first small in scale but growing over time. This generally occurs over timescales of tens of thousands of years, for small caverns to form, to millions of years for their complete development (De Waele et al. 2011). These caverns and conduits lead to the possibility of sinkholes forming in the overburden as the caverns can collapse or become receptacles of overlaying material. Anthropogenic factors can lead to faster rates, particularly in evaporite karsts which are more soluble than calcium carbonates (Gutiérrez et al. 2014).

Receptacles are an important part of sinkhole morphology and are defined as any voids or cavities capable of receiving mobilised materials from above (Buttrick et al. 2011). Sinkholes can be differentiated by two main triggering processes. The first is caused by groundwater extraction effectively lowering the water table and the second is due to the ingress of water, often from leaking services or poor storm water drainage (Oosthuizen & Richardson 2011). Both these processes ultimately lead to the removal of roof strata support and its collapse, caused by either

the lack of void water pressure or the ingress of water leading to the erosion of weathered material into receptacles (Buttrick et al. 2011). A third triggering process worth mentioning is if the roof strata of a cavern become overloaded (e.g. by infrastructure development) leading to its collapse (Van den Eeckhaut et al. 2007).

Sinkholes are identifiable by an abrupt depression at the soil surface (Van den Eeckhaut et al. 2007). They vary in morphology (cylindrical, conical, bowl- or pan-shaped) and can occur in a wide range of sizes from less than a metre up to hundreds of metres across and a few tens of metres deep (Gutierrez et al. 2014). It should be noted that there are significant differences between sinkholes forming in evaporite compared to carbonate rocks. Evaporites (typically halite and gypsum) dissolve much more rapidly, up to 100 times faster than carbonates. They, therefore, produce a broader diversity of sinkholes occurring at a higher frequency, higher subsidence rates and are often larger in extent (Gutiérrez et al. 2014).

Sinkholes have been genetically classified into eight classes based on two terms: 1) geological conditions and 2) subsidence processes (Gutiérrez et al. 2014). The combination of these two terms results in a specific sinkhole's class as can be seen in Figure 2.1. The most important distinction for this study is between cover-collapse sinkholes and solution sinkholes (also called dolines). Solution sinkholes form where karst rocks are exposed, or close to the surface, and water flow is concentrated in high permeability areas leading to a lowering of the surface. These rarely constitute a hazard due to their slow development (De Waele et al. 2011). Cover-collapse sinkholes, on the other hand, are the most sensitive to human influence and cause the greatest damages (Gutiérrez et al. 2014). They form when the karst bedrock is covered by overburden and is prone to collapsing into cavities.

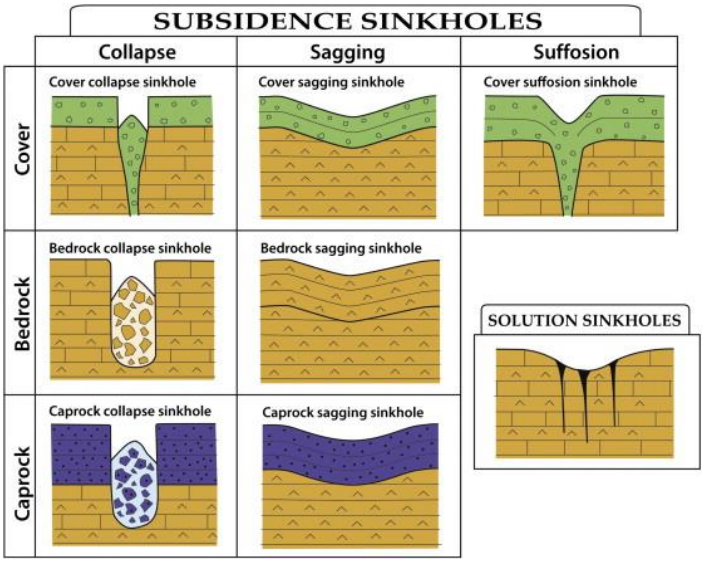

Figure 2.1 A widely used sinkhole classification system whereby a sinkhole is classified by its geological conditions (row) and its subsidence process (column) (adapted from Gutiérrez et al. (2014)).

Certain conditions are necessary for the formation of cover-collapse sinkholes. Firstly, the overburden must have enough inherent strength to form a roof, yet should be permeable and erodible. There must further be near-vertical walls or pillars of dolomite near the surface to support bridging material that, if failing, results in the sudden formation of cavities. If there is no bridging support or the overburden is too weak to form an arch, subsidence sinkholes will instead occur. Furthermore, hydrological action should be present. The water table should consequently be low, as percolating water has a higher erosive potential above the water table. Finally, receptacles are required to receive eroded material (Momubaghan 2012). These conditions are all present in the Gauteng dolomites (Trollip 2006).

2.1.2 Precursory deformation

It is known that roof failures of underground caverns, which lead to sinkholes, do not occur without warning signs. Detecting such signs may enable the prediction of ultimate collapse (Parise & Lollino 2011). In mining environments, for example, it is known that surface cracks are an important sign of impending collapse and finding them is an established part of “reading the ground” for hazard mitigation (Szwedzicki 2001). Such evidence manifesting on the surface before the collapse is the result of a phase of continuous underground erosion leading to upward cavity migration (Chang & Hanssen 2014). This process is illustrated in Figure 2.2. There are similarities between mining cavern collapse and sinkhole formation and the term “chimney caving” is used to describe the upward propagation of the underground cavity in mining (Augarde, Lyamin & Sloan 2003).

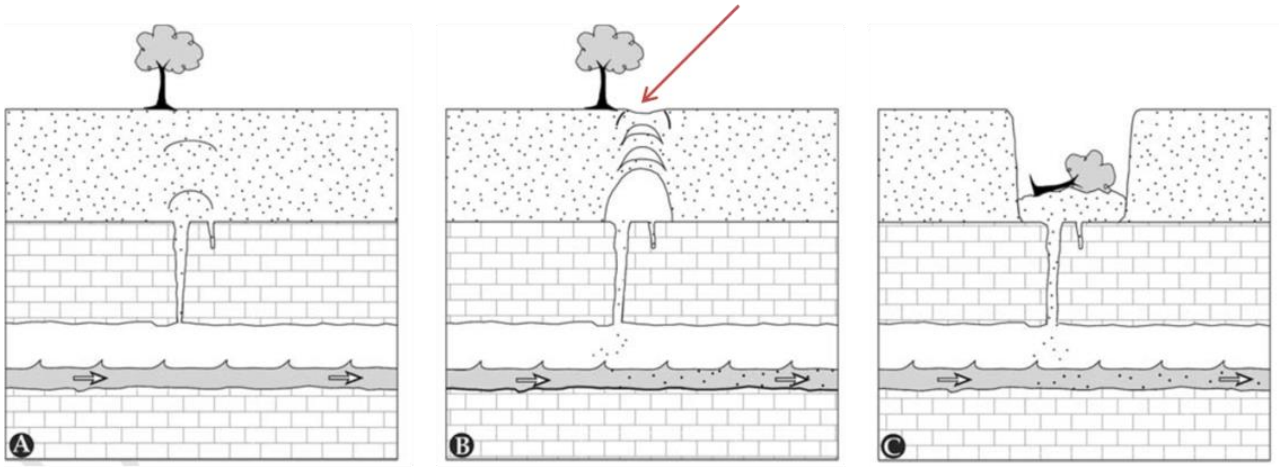

Source: Gutiérrez, Cooper & Johnson (2008)

Figure 2.2 Diagram illustrating the formation of a cover-collapse sinkhole due to subsurface erosion. Note the surface deformation due to underground cavity migration before the sinkhole forms which referred to as precursory deformation (indicated by the red arrow in block B).

Evidence of cavity migration on the surface includes tension cracks in the ground, walls or infrastructure, and shear movement along planes of weakness. Further development results in vertical, or sometimes horizontal, movement and visible subsidence basins forming (Parise &

Lollino 2011). Such signs are known to be able to develop rapidly in a matter of hours, or up to months and years (Szwedzicki 2001; Chang & Hanssen 2014). It has been noted that there has been very little focus on the geotechnical evidence of precursors in literature, in spite of their value as early warning signs (Szwedzicki 2001; Parise & Lollino 2011). There is, therefore, a lack of knowledge regarding the physical nature of sinkhole precursors to generate an accurate model of their spatial and temporal evolution (Vaccari et al. 2013; Boncori et al. 2015).

An important aspect of precursory deformation is how the size of the precursory deformation relates to the size of the eventual sinkhole. This is especially important due to limitations to detecting small-scale deformation using DInSAR discussed in Section 2.3. The potential size of sinkholes, or subsidence-affected areas, is currently determined in South Africa for finding a safe "potential development space" (Buttrick et al. 2011). This space is determined based on the depth of the cavity and the strength of the soil. Deeper cavities are expected to result in a larger sinkhole appearing (Day 2012; Avutia 2014). Some limited empirical evidence shows precursory deformation to be around four times larger than the actual sinkhole, yet this finding comes from limited studies that cannot be extrapolated to all sinkholes due to their diverse nature (Chang & Hanssen 2014; Intrieri et al. 2015).

Precursory deformation can be categorised into three stages of development according to Closson et al. (2005). First is "the nucleation and development of an underground cavity" stage, where a cavity forms underground yet no surface indications is present. These can be detected by techniques such as microgravimetry (Paine et al. 2012) and ground penetrating radar (Carbonel et al. 2013), yet the smaller and deeper the cavities are the more unlikely they are to be detected. The second stage is categorised by the development of subsidence areas (Closson et al. 2005). These basins are detectable by precise measurements techniques such as levelling, and potentially DInSAR (Stevanovic et al. 2015), yet do not yet manifest as cracks in the ground or infrastructure. The final precursor development stage is categorised by the appearance of circular cracks generally indicating a strong possibility of roof collapse and a sinkhole forming. It is again noted that these cracks can evolve within hours or over many years (Closson et al. 2005).

2.1.3 Sinkhole geology in the Gauteng province

Sinkholes in Gauteng are caused by hydrological action in the highly soluble dolomite and chert deposits of the Chuniespoort group, which forms part of the Transvaal Supergroup. Hydrological action can include both the ingress of water and the lowering of the water table. The Chuniespoort group is found over approximately 25% of the province leading to large areas of hazardous dolomite land prone to sinkhole formation (Buttrick et al. 2011). The term 'dolomite land' is used when dolomite occurs directly or at shallow (<100 m) depth. The Chuniespoort group is generally found under younger deposits from the Transvaal Supergroup (specifically the Pretoria group), the Karoo Supergroup as well as Cenozoic unconsolidated deposits (Buttrick et al. 2001). The

sinkholes in the study area are found in mainly four dolomite formations, namely the Eccles, Lyttelton, Monte Christo and Oaktree (in order of decreasing sinkhole occurrence overall). However, in Centurion nearly all the sinkhole events are found on the Monte Christo formation (Oosthuizen & van Rooy 2015). These four formations are part of the Malmani Subgroup of the Chuniespoort Group (Richardson 2013). These dolomites are approximately 2.2 Billion years old, up to 1400 m deep and have been weathered extensively since deposition (Momubaghan 2012).

Sinkholes form due to cavernous conditions in the bedrock due to the weathering in these formations, leading to widespread dolomite and chert topography (Trollip 2006). The vertical, top down, weathering process found in these dolomites results in the overburden being less dense deeper down. Depths to bedrock range from shallow to more than 30 m deep (Momubaghan 2012). Infiltrating water is, therefore, able to act on the low-density, deeper, material leading to cavities (voids) forming. The growth of these cavities, due to the erosion of the material into deeper receptacles, leads to a loss of support of the surface, shear failure of the competent erosion resistant karst residuum, and consequent sinkhole formation (Oosthuizen & Richardson 2011; Avutia 2014).

The dolomite in Gauteng is often overlain by highly weathered materials. This overburden generally consists of compressible Weathered Altered Dolomite (WAD) and chert gravels prone to differential leaching (Avutia 2014). WAD has little to no cohesion resulting in progressive tensile failure during cavity propagation. Chert is a prominent overburden material in the Monte Christo formation characterised by high shear strength values and therefore brittle failure modes. This implies that there may be little to no deformation prior to sinkholes for overlying chert bands. These instead suddenly fail due to the underlying erosion of WAD into receptacles (Avutia 2014). Collapse sinkholes in Gauteng often occur where WAD, overlain by chert, is progressively eroded until the chert fails suddenly due to a lack of support (Avutia 2014). The different failure modes between WAD and chert has important consequences for this study, as limited precursory subsidence will lead to challenges in an early warning system.

Human influence increases the chance of sinkhole formation. More than 98% of sinkholes in the study area can be attributed directly to anthropogenic causes such as leaking services, poor stormwater management and ponding of water (Buttrick et al. 2011; Richardson 2013). There is evidence that sinkhole formation in the study area is not caused by dewatering but rather due to the ingress of water. In particular, it has been found that the dolomite aquifers in the research area, which are at a depth of about 90 m, are not subject to dewatering presently (Buttrick et al. 2011). Buttrick et al. (2011) found that within a 3700 Ha area south of Pretoria 650 sinkholes developed between 1984 and 2004 of which 99% were due to poor stormwater management, leaking services and ponding of water. This percentage corresponds to a more recent finding by Richardson (2013) that 98% of events in Tshwane can be attributed to anthropogenic causes. In the Centurion CBD,

93% of sinkholes were identified to be directly due to anthropogenic ground disturbance (Oosthuizen & van Rooy 2015).

The size of sinkholes is a critical parameter for this study due to minimum detectable limits inherent in DInSAR (discussed further in Section 2.3). Sinkholes in Gauteng take a circular shape and can be up to 125 m in diameter with steep sides and up to 50m deep (Oosthuizen & Richardson 2011). Historical analysis of the major sinkhole prone areas of Gauteng showed that sinkholes in the West Rand tend to be large to very larger with diameters of 5m to over 15m. In Tshwane however, they tend to be between 2 m and 15 m in diameter. In total, it was found that 86.48% of sinkholes in Tshwane are smaller than 15m in diameter with the average being 8.5 m (Richardson 2013). In Centurion, in particular, the average sinkhole size was found to be only 5.1 m (Oosthuizen & van Rooy 2015).

Possible precursory deformation before sinkhole collapse in South Africa has been classified under “Subsidence formation” (as opposed to “Sinkhole formation”) as “partly developed sinkholes” (Oosthuizen & Richardson 2011). It was noted that this surface settlement resembles a subsidence basin but is the result of the incomplete development of a sinkhole, possibly due to the termination of subsurface erosion. Such subsidence can be regarded as sinkhole precursors since it is evidence of a sinkhole and continuation of subsurface erosion may lead to a sinkhole forming.

2.1.4 Sinkhole risk management in the Gauteng province

When a hazard such as a sinkhole is present, it can present a risk to society. This risk can either be avoided (by not developing on sinkhole prone land) or it can be mitigated (by ensuring geotechnical surveys, strict building codes and monitoring efforts) (Billi et al. 2016). Risk mitigation is important in Gauteng since risk avoidance measures were deemed not to be feasible or practical as most land is, or will be, extensively developed (SABS 2012; Potgieter, Pretorius & Walt 2016). Current risk assessment and reduction in South Africa is based on “Scenario supposition” concepts outlined by Buttrick & Van Schalkwyk (1995); Buttrick et al. (2001); Buttrick et al. (2011) and Watermeyer et al. (2008). Scenario supposition is based on three main regulations; (1) placing restrictions on land use, (2) ensuring appropriate development and (3) establishing requirements for the following: the management and monitoring of water systems, the construction of above and below ground water bearing services, and finally evacuation procedures for if an event occurs. Dolomite risk has been successfully managed in areas of Gauteng through the rigorous application of this strategy, initialised in 2004 (Watermeyer et al. 2008). Evidence of this success is a reduction in ground movement events from 50 per year to five per year after rigorous risk management strategies were put in place. This translates to a 90% reduction in the number of events (Buttrick et al. 2011). However sinkholes are expected to continue to pose a risk as the rate of sinkhole formation for the period of 2009 - 2019 is expected to be similar to the 2000-2008 period over the entire study area (11.5 p.a.) (Richardson 2013).

A national standard for construction on dolomite land has been published by the South African Bureau of Standards (SABS) as the SANS 1963 (South African National Standard) document. It is divided into three parts. The first two documents relate to general principles, geotechnical investigations and building design. The final document is important for this study since it discusses risk management on dolomite ground (SABS 2012). This document is also based on the scenario supposition methods discussed by Buttrick et al. (2001).

Monitoring of dolomite land in terms of a precursory deformation for early warning systems is not included in the SANS 1963 framework even though it may prove to be a highly valuable addition to mitigation strategies. Monitoring within this framework is currently focussed on infrastructure monitoring (Water-bearing service, buildings, roads, etc.) groundwater levels and ground surface monitoring. The guidelines for “ground surface monitoring” are currently not quantitative or useful for the monitoring of large scale areas and only include regular visual inspection of the surface (to identify cracks or water ponding). Furthermore, recent work has shown that guidelines for development on dolomite ground may be negatively influencing development due to being overly restrictive leading to a lack of innovation to solving the problem (Day 2011). It is important that recent advances in dolomite risk management and engineering methods that reduce the risk need to be considered for rational risk assessments (Oosthuizen & van Rooy 2015).

According to SANS 1963, areas in which subsidence has already been observed should be regularly inspected by visual or surveying methods – and the data should be stored in a single database (SABS 2012). The Council for Geoscience has played an important role since the early 1970s in assisting authorities with sinkhole risk evaluations (Stamper 2011) and is the current custodian of the National Dolomite Databank containing sinkhole inventories and stability reports in line with the SABS recommendations (Oosthuizen & van Rooy 2015). In recommendations made after a recent study of sinkhole records, the need for accurate and thorough reporting of sinkholes was highlighted to address current incomplete inventories (Richardson 2013). Yet, no mention of the potential of SAR technologies was made which is important given its potential and its global record of success in subsidence monitoring. In their recent review of geohazards in karst, Gutiérrez et al. (2014) state that monitoring, and warning systems can be used to reduce financial and personal losses due to sinkholes yet overlooks the possibility of using DInSAR technology. Even more recently, however, the potential of DInSAR to monitor sinkhole deformation in urban environments has been noted (Vaccari et al. 2013; Bruckno et al. 2015; Intrieri et al. 2015; Stevanovic et al. 2015; Ozden et al. 2016). Remote sensing methods are capable of systematically monitoring large areas of land for subsidence features and can be an effective, yet generally overlooked, capability for geohazard mitigation.

2.1.5 Current sinkhole monitoring techniques

Geological hazard monitoring is an established field and dedicated instruments have been developed to monitor them. Sinkholes are the exception to this and no specific tools have been created to monitor their formation (Intrieri et al. 2015). Sinkholes have been underestimated for a long time in comparison to other geohazards such earthquakes and volcanoes (Calo et al. 2011). However, due to the recent explosive population growth and urbanisation trends experienced worldwide, karst terrains are increasingly developed upon and the risk sinkholes pose is increasing (Gutiérrez et al. 2014). Populated areas susceptible to sinkhole formation need to be actively managed (Billi et al. 2016). Monitoring systems capable of detecting precursory deformation reliably, safely and cost-effectively is seen as a critical part of sinkhole hazard mitigation (Gutiérrez, Guerrero & Lucha 2008).

Current sinkhole monitoring techniques rely on three approaches: 1) the detection and monitoring of existing sinkholes, 2) the detection of subsurface cavities, and 3) the detection and monitoring of precursory ground movement. It should be noted that monitoring existing sinkholes and detecting subsurface cavities are outside the scope of this study and are considered only briefly.

The first sinkhole monitoring approach relies on detecting and monitoring existing sinkholes. This can be done by field investigations (GPS, levelling etc.), remote sensing or by examining topographical maps (often derived from remote sensing) (Galve et al. 2009; Intrieri et al. 2015). Remote sensing methods typically involve visual inspection of optical or thermal imagery. There has however been a general lack of success using these techniques as existing sinkholes are typically hard to identify visually (Kaufmann & Quinif 2002; Seale 2005; Joyce et al. 2014). Automated classification techniques such as object-based image analysis (Dou et al. 2015) and convolutional neural networks (Lee et al. 2016) are being explored. Analysing terrain variations on terrain models has been successful for finding sinkholes. LiDAR-based models have higher resolution and can be used to detect and quantify sub-metric geomorphic features, such existing sinkholes, and to further quantify sinkhole growth (Filin et al. 2014). Automated extraction of sinkholes features from LiDAR terrain models is also being explored (Wu, Deng & Chen 2016).

The second sinkhole monitoring approach relies on the detection of subsurface cavities. The presence of subsurface cavities indicates areas at high risk for sinkhole formation and these can be detected with various techniques. Ground penetrating radar (Batayneh, Abueladas & Moumani 2002), gravity surveys (Paine et al. 2012) and electric resistivity testing (Das & Mohanty 2016) are some of the non-destructive techniques often used to detect subsurface cavities. Destructive techniques include cone penetration and percussion borehole investigations that correlate penetration rate to determine the material strength (Avutia 2014). These techniques are however expensive, expose the operators to risk and cannot be used to monitor large areas.

The final sinkhole monitoring approach aims to detect and monitor precursory ground movement and is relevant to this study. Detecting and monitoring small-scale ground deformation prior to sinkhole formation has significant potential for providing an early warning of sinkhole formation. *In situ* or ground-based methods are able to measure small-scale subsidence, but cannot be used for large area monitoring. These methods can only measure small areas (often only point targets) periodically and at a high cost. *In situ* investigations also expose the surveyors to hazardous conditions in unstable areas. *In situ* ground deformation monitoring is generally done by levelling, differential GPS and related survey techniques. GPS and levelling are able to provide high-accuracy three-dimensional positional information (Quin & Loreaux 2013). These methods are highly accurate, with standard deviation height errors of less than 1 mm (Raucoules et al. 2009). GPS, in particular, can obtain an absolute position and detect abrupt changes due to a high temporal sampling frequency. This accuracy comes at price as these methods are time consuming and expensive. Furthermore, these provide only point based sampling with a sparse density and frequencies (Raucoules et al. 2009). The entire surface of a study area cannot be covered frequently and cost effectively as is possible with remote sensing (Ferretti et al. 2011).

A terrestrial-based remote sensing technique, known as Ground-Based-InSAR (GB-InSAR) is frequently used to monitor surface deformation with high accuracy. GB-InSAR is a technique whereby radar is installed to acquire surface measurements periodically. According to Crosetto et al. (2014), the most relevant applications for this technique include: 1) slope monitoring for operational early warning systems in open pit mines, 2) natural rockfalls, 3) landslides, 4) volcanos and 5) tracking glaciers. GB-InSAR can also be used to monitor infrastructure in urban environments including bridges and dam walls. It is however not ideal for sinkhole detection since the system is set up in a semi-horizontal looking angle. Recently, however, this technique was able to detect precursors to sinkhole formation on a road in an Italian town identified to be at a very high risk for sinkholes (Intrieri et al. 2015).

LiDAR is an active remote sensing technique that generates topographical information that can theoretically be used for monitoring deformation over larger areas than GB-InSAR. However, deformation monitoring with LiDAR is challenging as typical rates of subsidence are within the error limits of LiDAR collections (Joyce et al. 2014). Reaching the required accuracy requires the instrument to be within 10 m to 100 m from the ground, limiting its wide area applicability (Intrieri et al. 2015). Structure from motion (SFM) is another method of reconstructing three-dimensional terrain from images taken from different angles at a lower cost than LiDAR. It, therefore, has the potential to be used for mapping sinkhole dimensions however the accuracy is typically too low for precursor detection through elevation model subtraction (Clapuyt, Vanacker & Van Oost 2015). It should be noted that passive optical remote sensing techniques, specifically feature tracking, can successfully be used to detect ground movement due to large earthquakes (Leprince et al. 2007).

However, such techniques can only be used to detect significant horizontal movement and detecting vertical ground deformation due to sinkhole related subsidence is not possible.

Finally, interferometric SAR remote sensing, chosen for this study, is an attractive tool with a proven record of accurate measurement over large areas (Ferretti et al. 2015) and will be discussed in Section 2.2.1 below.

2.2 DInSAR for measuring surface deformation

This section will discuss the theory and application of differential SAR interferometry for measuring surface deformation, globally as well as in South Africa, with a particular focus on sinkhole investigations.

2.2.1 Synthetic Aperture Radar

Synthetic Aperture Radar is an active microwave imaging system with cloud-penetrating capabilities (Ferretti et al. 2007). SAR satellites illuminate an area of the earth with electromagnetic pulses in the microwave frequency. On-board receivers record the reflected amplitude, polarisation and phase information from the returning radiation. A two-dimensional image is created from the reflected radiation by using the travel time and amplitude information of the returning radar pulses in a process called focussing (Bürgman, Rosen & Fielding 2000).

A focused SAR image used for interferometry is a complex product called an SLC (single look complex) image. These contain amplitude and phase information. The amplitude is a measure of the returning wave energy, which depends on surface properties such as slope, roughness and dielectric (Bürgman, Rosen & Fielding 2000). Various ground interactions can result in surface or double bounce scattering. Some surface penetration may also occur, which results in volume scattering. Penetration depends on the wavelength and the properties of the surface. Considerable penetration into dry snow, ice, soil or vegetation is possible - especially for longer wavelengths (Moreira et al. 2013).

The measured phase information can be used for millimetre accuracy measurements of the earth's surface through Differential interferometry (DInSAR) processing algorithms as discussed in Section 2.2.2. Advanced processing techniques have been developed to improve basic concepts and are briefly discussed in Section 2.2.3. The current state of the art of DInSAR research in South Africa and applied to sinkhole precursors will be discussed in Section 2.2.4 and Section 2.2.5 respectively.

Seminal and detailed guides to SAR interferometry were published by Massonnet and Feigl (1998), Bürgman, Rosen & Fielding (2000), Hanssen (2001), Ferretti et al. (2007) and Moreira et al. (2013). These provide a valuable foundation of the theoretical and practical aspects of DInSAR processing and interpretation.

2.2.2 SAR interferometry

Differential SAR interferometry (DInSAR) is the measurement of the signal phase change over time. In the SAR image, the phase is directly related to the two-way travel distance between the ground and the sensor. The phase cycles between +π and -π as the wave propagates and the returning phase is measured precisely by SAR systems. If the ground surface moved in the line of sight (LOS) of the SAR between image acquisitions, it will result in a change in travel distance. This, in turn, results in a change of phase that can be identified by subtracting the phase information of one SLC SAR image from another image in a process called interferogram generation (Ferretti et al. 2007). Ground displacement results in signature “fringes” on the resulting interferogram which are patterns similar to contour lines formed by the phase cycling between +π and –π (Moreira et al. 2013).

Mathematically the interferogram is generated by cross-multiplying one SLC SAR image (referred to as the master) with the complex conjugate of a coregistered second image (referred to as the slave). This results in an interferogram in which the amplitude is the product of the amplitude of the two input images and the phase is the phase difference between the two images (Ferretti et al. 2007). This phase difference is directly proportional to the change in distance between the radar and the ground divided the wavelength of the radar.

Interferometrically compatible SAR images can be acquired at the same time, as with the Shuttle Radar Topography Mission’s (SRTM) boom antenna (Neumann et al. 2016), with bi-static SAR platforms (Krieger et al. 2013) or by the same system over different times (known as repeat-pass interferometry). The time difference between repeat-pass image acquisitions is referred to as the temporal baseline and is controlled by the orbital revisit time of spaceborne sensors. The relative distance between the SAR systems at the time of image acquisitions is the physical baseline. There are two main definitions of this baseline and is illustrated in Figure 2.3. The baseline in the plane perpendicular to the orbit is called the interferometer baseline. The more relevant measure for DInSAR is the perpendicular (or normal) baseline, which is the projection of the interferometer baseline perpendicular to the slant range (Ferretti et al. 2007). Larger perpendicular baselines are more sensitive to topographical variations further discussed in Section 2.2.2.1 below.

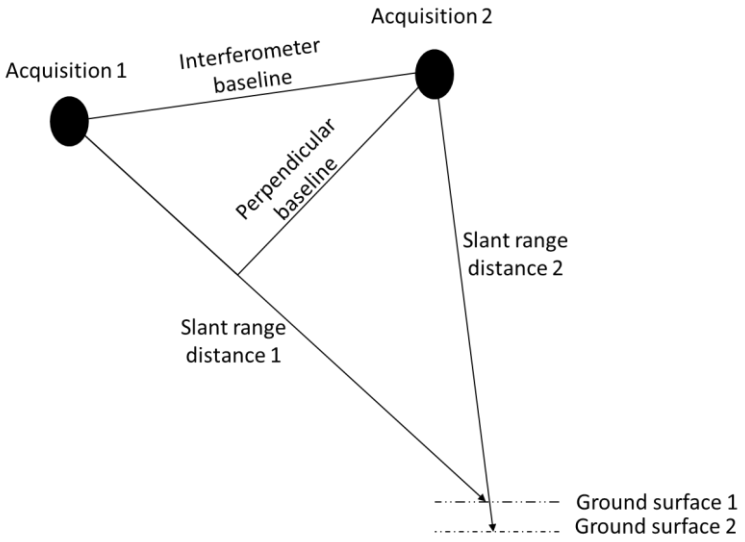

Figure 2.3 The geometry of repeat-pass SAR interferometry illustrating the different baselines. Note the exaggerated difference in incidence angles between acquisitions. In reality these are approximately equal due to the large distance between the satellite and the earth's surface.

2.2.2.1 Factors controlling differential interferometric phase

The concept of measuring the change in phase can be used successfully only when the radar target on the ground does not change its 'radar signature' with time. The surface area on the ground represented by a SAR pixel is typically represented by hundreds of distributed scatterers. Each of these contributes to the final phase through a complex combination of rotation and delay factors (Massonnet & Feigl 1998). This is known as a distributed scattering cell. Point targets occur if a single scatterer, like a corner reflector, dominates the cell (Ferretti, Prati & Rocca 2001). The final phase of a single SAR pixel is random since it is a sum of hundreds of unknown contributions. However, the phase return remains consistent between acquisitions as long as no change took place on the surface. Differencing the phase of a single pixel from different acquisitions may isolate specific contributions or changes to the pixel by eliminating the random contributions (Massonnet & Feigl 1998).

Interferometry allows for the measuring of the various contributions to the change in phase in a cell to isolate the displacement factor. Contributions to a change in phase found to be particularly important include: 1) orbital path differences between acquisitions, 2) flat earth, 3) topographical variations, 4) ground displacement, 5) atmospheric variations, 6) thermal noise and 7) changes in the target's dielectric properties (Osmanoğlu et al. 2015). In general, larger signals (atmosphere, deformation and topography) dominate and mask smaller signals (dielectric). These smaller contributions to a coherent phase change are generally assumed negligible in interferometry (Osmanoğlu et al. 2015).

The first four factors that cause a significant change in phase in the interferogram (labelled 1 to 4 above) are essentially due to a change in range between the two SAR acquisitions and the ground.

If the first two factors are modelled, it is possible to compensate for them and generate either a topographical map or measure ground displacement - depending on the application (Osmanoğlu et al. 2015). The orbital position of the satellite is generally precisely known and can be used to model and compensate for the orbital phase contribution. The flat earth and topographical phase contributions are due to the shape of the earth. Therefore, if an external DEM is available it is possible to compensate for these two contributions by considering the geometry between the satellite positions and the earth. An interferogram in which topography and flat earth are compensated for is called a differential interferogram (Moreira et al. 2013).

It is critical to emphasise here that the external DEM needs to be referenced to the same frame as the orbital data. Orbits are referenced to an ellipsoid. If the external DEM is relative to the geoidal height, the suitable geoid needs to be subtracted to obtain ellipsoidal height (Ferretti et al. 2007).

Errors in the orbital data, as well as the DEM, will lead to phase “residues” on the interferogram (Ferretti et al. 2007). Phase residues due to orbital data are very large in scale and not easily confused with small-scale deformation. Topographical phase residues can, however, be small in scale and be confused with ground displacement. The topographical phase is related to the perpendicular baseline, and these residues can be identified by monitoring the area over many interferograms with differing baselines. The topographical phase fringe rate over a certain change of height is known as the altitude of ambiguity. It is defined as the altitude difference on the ground that generates a change in phase of 2π (Massonnet & Feigl 1998). If the perpendicular baseline is very low, approximately less than <50 m, then the altitude of ambiguity becomes very large. The system’s sensitivity to topography is then said to be very low and deformation fringes can easily be identified even if topographical data is lacking. It follows that with a perpendicular baseline of ~0 m there can be no phase contribution from topography.

The atmospheric contribution to a change in phase is one of the biggest challenges in DInSAR research and is called the Atmospheric Phase Screen (APS) (Tang, Liao & Yuan 2016). The APS is due to attenuation of the speed of the microwave signals from the speed of light due to different atmospheric and ionospheric conditions. The contribution from the troposphere is due to the increased diffraction index of the atmosphere over empty space mostly as a result of water vapour (Bekaert et al. 2015; Yu, Li & Wang 2015). There is a less significant contribution to phase from the ionosphere which is due to microwave interactions with free electrons (Gomba et al. 2016). Ionospheric contributions to the phase are only a practical challenge for long wavelength (L-band) interferometry (Gomba et al. 2016). Tropospheric contributions are, however, not radar frequency dependent (Yu, Li & Wang 2015). Generally, acquisitions taken during the night are less susceptible to the APS due to less energy available for atmospheric perturbations due to convection and wind (Massonnet & Feigl 1998).

A common atmospheric effect is a phase fringe signature following topography and is due to the hydrostatic troposphere effect (Massonnet & Feigl 1998). This delay is said to be topography-like

since topography is required to reveal the signal, but the fringe rate will not be dependent on the perpendicular baseline as with typical topographical residue. These fringes are a result of the signal propagating through additional atmospheric layers if it returns from a lower elevation than from a higher elevation. A constant offset is therefore added around topographical variation resulting in fringes caused by topography but controlled by atmospheric conditions (Massonnet & Feigl 1998).

If very specific data regarding the atmospheric state during the time of acquisition can be acquired then attempts can be made to computationally compensate for this error source (Bekaert et al. 2015; Yu, Li & Wang 2015; Gomba et al. 2016). Otherwise, manual interpretation and pairwise analysis are used to identify the atmospheric effect by exploiting four of its identifying characteristics (Massonnet & Feigl 1998; Barra et al. 2016). Firstly, it is large in spatial scale. Secondly, its influence on phase is random between acquisitions. Thirdly, the APS imposes a phase delay during image acquisition and not between acquisitions. It is, therefore, present on all interferograms generated from a single affected acquisition, yet will not be present on interferograms covering the same period but generated from independent acquisitions. Finally, it may follow topographical variation. Therefore, large fringe patterns detected at the same place on interferometric pairs where a common image is used, or when topography is exaggerated even though an accurate topographical model was used, is likely due to the atmosphere (Massonnet & Feigl 1998).

2.2.2.2 From differential phase to displacement

A differential interferogram is an image that shows the changes in phase due to ground displacement (considering no atmospheric, orbital or topographical residues are present). However, further processing is necessary to “unwrap” the phase, calculate absolute displacement in metres and possibly calculate displacement in vectors other than the LOS.

The interferometric phase on a differential interferogram phase is still wrapped around 2π due to the sinusoidal nature of the radar wave. Unwrapping is the process of spatially adding the correct integer multiple of 2π to interferometric fringes to determine actual displacement. Unwrapping is a mathematical problem with no unique solution and many algorithms are available that attempt to solve it from different angles (Ferretti et al. 2007; Hooper & Zebker 2007). These algorithms can be divided into path independent and path following approaches. Path-independent approaches attempt to find a global solution by minimising errors between the wrapped and unwrapped data (Osmanoğlu et al. 2015).

Path-following methods are based on logically moving between pixels and minimising errors (Osmanoğlu et al. 2015). It can be visualised by “walking” up and down a phase “hill” using different paths yet ending in the same location. If the unwrapping was accurate then logically the

starting height will be equal to the ending height, otherwise, some error has occurred. Advanced methods use network cost that, for example, provides a higher priority to highly correlated pixels.

It is important to note here the maximum deformation gradient (further discussed in Section 2.3.1). If deformation exceeds half the wavelength between pixels, then unwrapping will not be possible, as it is not known how many phase cycles was exceeded (Massonnet & Feigl 1998; Sun & Muller 2016).

Finally, the displacement map can be calculated from the unwrapped phase. The unwrapped phase is relative and the absolute phase can only be calculated with *a priori* information such as a known point of no deformation or GPS measurements. Furthermore, the displacement is only known in the LOS direction. Displacement from another look direction is needed to calculate three-dimensional deformation. Otherwise, a displacement direction can be assumed based on knowledge about the phenomena (for example, the downslope direction would be valid for landslide deformation) (Osmanoğlu et al. 2015).

2.2.2.3 Coherence

Coherence is a statistical measure of the decorrelation between image acquisitions (Closson et al. 2005). For interferometry to be possible, it is critical that the individual scatterers in a cell do not change over time. This condition is generally met if two images are taken at the same time. If not, changes in the scatterers will result in decorrelation of the radar phase to differing extents. Coherence is estimated by calculating the local cross-correlation coefficient of a SAR image pair over a small moving window (Ferretti et al. 2007). Coherence is a value between zero and one with one being fully correlated and zero being total decorrelation. Understanding coherence is important as it describes the amount of change that has occurred in the scene. More importantly, it is a measure that relates to the quality of the phase information used for deformation measurement (Zebker & Villasenor 1992). Specular surfaces will provide little signal return and result in low coherence (Leblanc et al. 2015).

Coherence is related to four factors: 1) The SAR system's signal-to-noise ratio, 2) spatial decorrelation, 3) temporal decorrelation and 4) processing decorrelation (Zebker & Villasenor 1992). The first factor is related to systematic thermal noise. The second factor, spatial decorrelation, is due to the combination of individual scatterers (speckle) within the cell. It is sensitive to changes in look angle and therefore to the perpendicular baseline. Common band filtering is done to filter for shifts in the radar return due to this factor (Gamma Remote Sensing 2011). However, once the perpendicular baseline exceeds a certain distance, the phase becomes pure noise and coherence becomes zero. This distance is called critical baseline (Alberga 2004).

Temporal decorrelation, the third factor, is due to the land surface evolution between image acquisitions. Different scattering mechanisms on the ground, in particular volume and surface scattering, are susceptible to temporal decorrelation to different degrees. Volume scatterers lose

coherence the fastest. Further aspects influencing this include human activities, vegetation growth, rainfall and wind (Thiel & Schmullius 2016). A longer temporal baseline leads to a higher probability of change and reduced coherence (Engelbrecht et al. 2014).

Processing decorrelation is a factor that leads to a loss of coherence in an interferogram due to processing techniques and includes interpolation and co-registration errors (Hanssen 2001). Sub-pixel co-registration accuracy is needed for interferometric measurements. Generally, a registration accuracy of <0.2 is sufficient, this should ensure a loss of coherence of not more than 5% (Gamma Remote Sensing 2011). It should be noted that pixel registration accuracy as high as <0.0001 (in azimuth) is required for Sentinel-1 wide swath data (Prats-Iraola et al. 2015).

2.2.2.4 Accuracy assessment

Ground truth, ancillary data and background information remain a vital part of radar interpretation. Yet the properties of SAR techniques are such that ground truth is often not feasible to obtain. The most important properties are the extreme precision that DInSAR is capable of, as well as the large areas that are monitored over long timeframes. Another factor is the unpredictability of ground deformation due to phenomena such as sinkhole formation, which makes it difficult to set up precision levelling tools over the correct area before deformation takes place (Chang & Hanssen 2014). DInSAR uses data sets covering many years in areas where levelling/GPS data is not available or cost effective and many studies are done often in retrospect.

However, experimental and well-controlled field tests have been done to assess the accuracy of DInSAR techniques. Various DInSAR approaches were able to monitor deformation with sub-millimetre accuracy (Adam et al. 2009; Raucoules et al. 2009; Eineder et al. 2011; Ferretti et al. 2011; Hung et al. 2011; Quin & Loreaux 2013). However, many of these are based on advanced newer methods (discussed in Section 2.2.3). Hanssen (2001) emphasises that conventional repeat-pass differential interferometry is accurate in the sub-decimetre scale and that claims of millimetric precision should be treated with care, and accompanied by statements on coherence and meteorological conditions.

2.2.3 Advanced DInSAR techniques

Conventional DInSAR is considered to be a reliable and proven method of deformation detection (Cigna et al. 2012). However, particularly challenges related to the atmospheric phase screen and temporal decorrelation of ground targets were identified in the late 1990s as major limitations to the operational application of the DInSAR (Ferretti, Prati & Rocca 2001). Advanced DInSAR techniques have been developed to overcome challenges identified in conventional differential interferometry (Jia & Liu 2016). However, these advanced techniques have limitations that present challenges to sinkhole precursor detection (Castañeda et al. 2009). It is important to understand

the capabilities and requirements of these techniques, as future work in the field of DInSAR sinkhole precursor detection will explore these advanced techniques.

Advanced DInSAR is commonly referred to as multi-temporal InSAR (MT-INSAR), Persistent scatterer InSAR (PSInSAR) or Interferometric Stacking depending on specific approaches or software packages (Crosetto et al. 2016). These are all essentially data stacking techniques and can be broadly classified into two approaches: Small Baseline Subset (SBAS) and Persistent Scatter Interferometry (PSInSAR). These have distinct approaches to deal with decorrelation and the APS discussed in Section 2.2.3.2 and Section 2.2.3.3 respectively. Limitations of these techniques are discussed in Section 2.2.3.4. An interesting combination of the techniques is coherent point target (CPT-InSAR) which aims to integrate SBAS and PSInSAR methodologies (Zhang et al. 2011). Another technique has been developed that is not based on data stacking but instead on exploiting polarisation to handle decorrelation challenges and will be discussed in Section 2.2.3.1

2.2.3.1 Polarimetric interferometry (PolInSAR)

Polarimetric interferometry (PolInSAR) exploits the additional information that can be derived from polarimetric SAR systems. The main aim of PolINSAR is to separate scatters within cells based on their scattering mechanism, and then to use the most appropriate mechanism for interferometry (Papathanassiou & Cloude 2001; Neumann, Ferro-Famil & Reigber 2008). By identifying stable scatterers, it is theoretically possible to optimise coherence and increase the ability of DInSAR to measure deformation in low coherence environments. However, it has been found that PolInSAR coherence optimisation is not able to significantly improve deformation estimates in dense vegetation, particularly for shorter wavelengths (Engelbrecht & Inggs 2016)

2.2.3.2 Small Baseline Subset (SBAS)

SBAS is based on minimising the temporal and spatial decorrelation challenges identified in conventional DInSAR processing by limiting interferograms to acquisition pairs with small temporal and perpendicular baselines within a data stack (Gong et al. 2016). The atmospheric phase screen can furthermore be filtered out accurately since spatial and temporal information is available. The SBAS technique was first presented by Berardino et al. (2002) and was originally designed for monitoring very large areas but has since been modified to be able to analyse regional and local-scale phenomena (Manunta et al. 2011). SBAS is more capable than standard PSInSAR for monitoring areas characterised by lower coherence as it assumes that targets are characterised by distributed scattering mechanisms (Tomás et al. 2014). Nevertheless, SBAS requires downsampling and is generally not suitable for very small-scale deformation phenomena, such as sinkholes, where multilooking approaches are not favoured (Castañeda et al. 2009). The SBAS technique is based on a linear deformation model and is not able to detect non-linear displacement without *a priori* knowledge about the temporal behaviour of ground deformation. Processors able to

measure non-linear motion that is not reliant on a deformation model has become available and are being investigated (Gong et al. 2016).

Multidimensional SBAS is a further improvement, first presented by Samsonov & D'Oreye (2012), designed to overcome the limitations to the SBAS method. The M-SBAS approach allows the combination of all possible airborne and space-borne SAR data acquired with different acquisition parameters, temporal and spatial samplings and resolutions, wavelengths and polarisations. This method has many advantages, the most important of which is an increased spatial sampling frequency, reduced noise from most sources and the ability to derive three-dimensional deformation vectors (Samsonov, D'Oreye & Smets 2013). This approach is a powerful technique to characterise deformation accurately; yet, enough appropriate data is rarely available and this method is ideally suited only for very specific circumstances.

2.2.3.3 Persistent scatterer interferometry (PSInSAR)

Persistent scatterer interferometry is another widely used approach for dealing with the atmospheric phase screen and temporal decorrelation. Instead of focussing on interferogram pairs with high coherence, it relies on identifying pixels with a high coherence over the entire available data stack. PSInSAR uses the full resolution available to the sensor as well as all the available baselines to generate deformation time series (Crosetto et al. 2016). PSInSAR was first introduced by Ferretti, Prati & Rocca (2000) and Ferretti, Prati & Rocca (2001). PSInSAR relies exclusively on temporally stable targets with a high signal-to-noise ratio (SNR) found on a stack of SAR images - that are referred to as persistent scatterers (Schunert & Soergel 2012). Persistent scatterers are identified by statistical analysis pixels across the times series (Crosetto et al. 2016). In terms of the physical nature of these scatterers, they are point targets with a stable phase return over time often found on buildings, monuments, antennas, poles, conducts, exposed rocks or outcrops (Crosetto et al. 2016).

PSInSAR systematically distinguishes between atmospheric, topographic, deformation and residual components of phase observation based on their expected behaviour (Marinkovic, Ketelaar & Hanssen 2004). Atmospheric artefacts show a strong spatial correlation within SAR acquisitions but are uncorrelated in time. Topography shows a linear behaviour with the normal baseline while deformation motion is strongly correlated to time with various degrees of spatial correlation depending on the phenomenon (Prati, Ferretti & Perissin 2010). Modelling the predicted deformation phenomena enables the estimation of its deformation velocity over time (Jia & Liu 2016). A larger data stack results in a more reliable estimate of deformation and minimum stack sizes range from 5 to 25 depending on the data and method (Prati, Ferretti & Perissin 2010).

PSInSAR has been successfully applied for various applications including subsidence (Teatini et al. 2012; Del Ventisette et al. 2013; Yu et al. 2013) and landslide monitoring (Xia, Kaufmann & Guo 2002; Crosetto et al. 2013; Greif & Vlcko 2013). Experimental accuracy assessments have also

shown it to be theoretically capable of sub-millimetre accuracy (Marinkovic, Ketelaar & Hanssen 2004; Ferretti et al. 2007). Persistent scatterer techniques are being continually advanced after first introduced by Ferretti et al. in (2001). Important advances followed: Hooper et al. (2004) introduced the “Stanford Method for Persistent Scatterers”, an improved method of persistent scatterer pixel selection and processing which can reduce the required data stack from 15+ to ~6. Crosetto et al. (2008) introduced algorithms to estimate both the linear and non-linear components of deformation. Ferretti et al. (2011) introduced SqueeSAR, a PSInSAR technique that incorporates both point targets and relatively coherent distributed scatterers into processing. SqueeSAR leads to an increase in the spatial sampling density in terrains not characterised by point targets (like agricultural areas). And finally, Tomographic SAR, or 4-D imaging, the most advanced and effective interferometric technique capable of resolving scatterer location in three-dimensions as well as estimate their displacement over time (Fornaro et al. 2014).

Tomographic SAR essentially combines PSInSAR with three-dimensional focusing. By exploiting multi-baseline data stacks, it is possible to extend the synthetic aperture of the SAR not only along-track, but also across-track. It thereby enables focussing in the vertical domain as well as the horizontal (range, azimuth) domain. It is able to estimate extremely precise deformation velocities since it resolves individual scatterers within a pixel, even within layover (Fornaro, Reale & Verde 2013). It has proven to be capable of measuring metre scale urban infrastructure for effects as small as diurnal thermal dilation (Balz et al. 2012; Fornaro, Reale & Verde 2013). Tomographic SAR, however, relies on coherent point targets and data stacks with very specific baseline properties. A large total perpendicular baseline is required for a high resolution focussing in the vertical domain. The baselines should also be regularly spaced, a requirement generally more suited for aerial observation campaigns (Tebaldini et al. 2016) or tailored spaceborne platforms such as the future BIOMASS mission (Minh et al. 2015).

CAESAR is a recently introduced interferometric filtering concept, based on tomographic concepts and the covariance matrix from SqueeSAR (Fornaro et al. 2015). It is similar to PolInSAR as it attempts to discriminate between scatterers, but it exploits multi-baseline focusing, instead of polarimetry, to identify the scatterer. This technique may have interesting implications for interferogram filtering while preserving spatial resolution for small-scale deformation features. However, it should be noted that some spatial averaging is still applied.

2.2.3.4 Limitations to advanced DInSAR

Advanced stacking techniques have important limitations, especially in the context of detecting small scale, unpredictable sinkholes. Possibly a fundamental limitation for PSInSAR early warning systems is that PSInSAR, as well as SBAS, relies on a time series of data for processing. Collecting such a stack takes months to years using current satellite revisit times (Section 2.3.6). Once a baseline stack is collected it can be used for every new acquisition, however, this will

require reprocessing of the entire stack of images every time. PSInSAR processing is computationally expensive and time-consuming therefore limiting its early-warning capability. A related consideration is that only targets that remain stable over the acquisition timeframe (often years) can be utilised as persistent scatterers. If a sinkhole precursor occurs and results in a sinkhole forming within the data stack the area will lose coherence. It will likely be excluded from processing and *post hoc* precursor measurement will not be possible.

PSInSAR generally assumes linear deformation and therefore in cases where deformation is not linear there is significant uncertainty in the deformation estimates. Persistent scatterers are not identified if they are characterised by strong linear motion not modelled by *a priori* information (Crosetto, Monserrat & Crippa 2010). One of the most important limitations, therefore, is a lack of a physical model describing typical sinkhole precursor behaviour, especially in the study area (Vaccari et al. 2013). This is a challenge for not only PSInSAR but also SBAS. A robust understanding of sinkhole precursors is, therefore, an important requirement for these techniques. Generally, such models are derived from empirical and numerical assessment of the physical phenomenon (Augarde, Lyamin & Sloan 2003).

PSInSAR, just like conventional DInSAR is not able to measure deformation exceeding the maximum deformation gradient, which is half the wavelength of the sensor per scatterer between acquisitions (Crosetto, Monserrat & Crippa 2010). Increased revisit times, however, lead to the possibility of detecting faster deformation rates as discussed in Section 2.3.

Another limitation is that the location of persistent scatterers cannot be identified *a priori*, with the exception of the deployment of suitable corner reflectors. PSInSAR has therefore been described as an “opportunistic deformation measurement method” since deformation can only be monitored over scatterers eventually identified after processing (Crosetto, Monserrat & Crippa 2010).

It can be seen that for specific applications, such as detecting small-scale deformation of phenomena such as sinkholes, conventional interferometry remains an important and relevant technique. For example, conventional DInSAR, using the TerraSAR-X satellite, was recently compared to one of the most advanced time series algorithms, SqueeSAR, to monitor very fast mining subsidence. Conventional DInSAR was able to provide improved detection of rapid deformation compared to SqueeSAR, however with a lower accuracy (Przylucka et al. 2015). In the case of sinkhole precursors, it is more important to be able to detect rapid, unpredictable and un-modelled deformation than deriving precise deformation estimates. Conventional DInSAR was therefore expected to provide the necessary detection sensitivity to satisfy the objectives of this study.

2.2.4 The use of interferometry in southern Africa

South Africa does not experience the type of frequent, large-scale geological hazards such as volcanoes and earthquakes that have historically been investigated using DInSAR (Richards &

Brynard 2006; Zhou, Chang & Li 2009). Nevertheless, SAR interferometry has been used since the late 1990s with some success in the early 2000s (Doyle 2000). More recently, SAR has been used actively to specifically monitor mining-induced deformation, an important problem in the South African landscape and economy.

The first published investigation in southern Africa was the investigation of the Katse dam area for reservoir-induced crustal deformation with InSAR techniques (Doyle, Inggs & Hartnady 1997; Doyle, Wilkinson & Inggs 1999; Doyle, Stow & Inggs 2001). Due to inaccurate *a priori* modelling of crustal loading the resulting deformation were orders of magnitude smaller than expected, and below the limits of DInSAR. Nevertheless, an interferometric pair could be generated successfully despite challenging interferometric conditions, particularly related to topography. Interferometry was further used to create a DEM for a part of the Western Cape from C-band ERS data which highlighted atmospheric and geometric challenges to phase unwrapping (Doyle 2000). Following this Doyle et al. (2001) were able to map surface deformation after a magnitude 4.5 mining-induced earthquake that led to a rock burst in Welkom successfully.

DInSAR has been suggested as an option for monitoring soil erosion seen as a principle land degradation problem in the country (Roux et al. 2007). Kemp (2011) investigated DInSAR for monitoring erosion in South Africa using C-band ERS data. Interferometry was found to be unfeasible mainly due to high temporal baselines of the data set leading to low coherence conditions. It was concluded that interferometric coherence maps in this environment would be more suitable for land cover classification as a proxy for erosion.

Engelbrecht and Inggs (2011) showed the ability to detect mining induced subsidence using ERS imagery in South Africa. Temporal coherence was identified as a limitation to the technique and it was recommended that longer wavelength and fully polarimetric data should be explored to overcome this limitation. Engelbrecht and Inggs (2013) used L-band imagery and demonstrated that mining deformation could be monitored operationally using longer wavelength data. Further work focussed on polarimetric interferometry (PolInSAR) as a processing tool to overcome temporal decorrelation challenges in dynamic agricultural environments characterising much of the country (Engelbrecht 2013). It was found that despite increasing coherence significantly, PolINSAR was unable to overcome coherence limitations due to temporal decorrelation, particularly in the presence of vegetation. Further investigations revealed that PolInSAR coherence optimisation was more effective on L-band than C-band data (Engelbrecht & Inggs 2016).

More recently, there has been a specific focus on the measurement of Interferometric coherence, particularly over agricultural areas. The factors influencing coherence were analysed by Engelbrecht et al. (2014) and it was determined that temporal baselines and land surface evolution had the most significant effect. The value of pursuit monostatic X-band coherence for agricultural activity monitoring has also been investigated (Kemp & Burns 2016).

Geohazards occur frequently in South Africa and dolomite sinkholes and landslides are particularly important (Richards & Brynard 2006; Diop, Forbes & Chiliza 2010; Oosthuizen & Richardson 2011), yet there is limited regional DInSAR research into these geohazards. Furthermore, DInSAR processing techniques have evolved greatly since the first standard DInSAR workflows were developed (Crosetto et al. 2016). These advanced techniques discussed in Section 2.2.3, with the exception of PolInSAR (Engelbrecht 2013), have not been fully investigated yet. The full capability of SAR interferometry has not yet been realised in southern Africa, with the exception of intensive monitoring of mining subsidence, and there are many opportunities for future applications.

2.2.5 Interferometric detection of sinkhole precursors

SAR interferometry is regarded as a mature deformation monitoring technique and has been applied to monitor many important geohazards (Zhou, Chang & Li 2009; Ferretti et al. 2015). A particular development has been monitoring hazardous areas for precursors to geohazards such as landslides (Xie et al. 2016) and Volcanoes (Peltier et al. 2010). Yet there has been limited research into precursors to sinkhole formation (Intrieri et al. 2015). The nature of sinkhole precursors is relatively unknown, depending on the area of investigation. However, some case studies suggest that DInSAR techniques could be used for the detection of precursory deformation (Jones & Blom 2013; Nof et al. 2013; Chang & Hanssen 2014; Intrieri et al. 2015). The causes for the lack of major findings related to DInSAR for precursor detection may be due to the relatively recent advances in the resolution of the sensors (Sansosti et al. 2014) as well as the development of advanced techniques applied to the data (Prati, Ferretti & Perissin 2010). Alternatively, the unpredictability of sinkhole collapse events (Gutiérrez et al. 2008) or a lack of awareness of the growing scale of sinkhole hazards (Intrieri et al. 2015) may be the cause. Yet the hypothesis that precursory deformation occurs before sinkhole collapse can only be tested empirically and case studies need to be collected until the process is better understood (Augarde, Lyamin & Sloan 2003). DInSAR has recently been identified by many authors as a promising tool for detecting sinkhole precursors that can be used for a potential early warning system (Joyce et al. 2009; Bruckno et al. 2013; Nof et al. 2013; Vaccari et al. 2013; Intrieri et al. 2015; Parise 2015; Terwel & Hanssen 2015; Ozden et al. 2016). However, only a limited number of successful detections has been reported in the literature.

Colesanti et al. (2005) retrospectively analysed a major collapse event occurring at a mine in France using PSInSAR and reported that clear collapse precursor signs have been identified 10 months before the event. They also successfully used PSInSAR to overcome temporal decorrelation due to vegetation cover in their study area. In an experiment to identify and analyse precursors to collapse, researchers in France took the opportunity to monitor a cavern in a salt mine. It was expected to collapse due to overburden after the entire deposit was mined (Klein et al. 2008). A microseismic monitoring network, as well as levelling equipment, was installed around the cavern at various depths to measure ground activity. It was found that the rate and amplitude of

deformation increased considerably leading up to the collapse. Two processes affecting the rock were observed: diffuse failures that were linked to fracturing and failure of the roof, as well as rare, but massive, block avalanches causing pressure fields resulting in a measurable subsistence rate of up to a few millimetres a day. Based on these measurements the authors expected movements of a few centimetres before the generalised dolomite bed failure, which should be observable with SAR interferograms.

The Dead Sea is currently an important area of sinkhole-focussed subsidence research and is the location of likely the first sinkhole precursor detection through DInSAR (Nof et al. 2013). The primary cause for sinkhole formation in this area is the dissolution of a subterranean salt layer due to the replacement of hypersaline groundwater with freshwater in response to a drop in sea level (Nof et al. 2013). The water level is dropping at an increasing rate since the 1960s and is now exceeding one metre per year that in turn is causing regional lithospheric uplift which has been detected by DInSAR and GPS (Nof et al. 2012). The frequency of sinkholes has increased from 50 per year before 1999 to up to 380 per year in 2013. These have been the driving factors of research into ground deformation, subsidence, sinkhole formation and the search for the early detection of sinkhole precursors (Baer et al. 2002; Abelson et al. 2003; Closson et al. 2005; Filin et al. 2014; Nof et al. 2013).

Some of the early DInSAR research along the Dead Sea by Baer et al. (2002) was able to detect land subsidence and wide, shallow, subsidence features and relate these to sinkhole formation but was unable to identify specific sinkholes. The authors were also able to detect subsidence around sinkholes shortly after they formed but were unable to measure any subsidence that predated sinkhole formation. They concluded that gradual subsidence is unlikely to be directly related to sinkholes and that wide, shallow, subsidence features could not be used as predictable sinkhole precursors. This result should be considered with the local geology in mind since the solution of ancient salt layers is a very specific sinkhole formation type related to evaporite geology. The most important consideration is the fact that the sinkholes in the study by Baer et al. (2002) mostly formed before the SAR data was captured thereby making precursor detection impossible for most of the sinkholes. This reduces the certainty of their conclusion that no precursory deformation was found. The authors do state that precursors may be evident in new sinkhole occurrences in the future.

More work was done around the Dead Sea and precursory deformation was detected up to seven years before a newly built dyke collapsed, illustrating the potential for the technique, and the importance of knowing the ground stability before large construction projects (Closson et al. 2003). Precursory deformation was measured to be ~12 cm over seven years but the exact spatial scale of the deformation was not reported on. Closson et al. (2005) further elaborates on the potential of using SAR interferometry for precursory deformation monitoring and identify temporal loss of coherence as an important challenge to detection of sinkhole precursors. Moisture and surface

erosion were suggested as important factors leading to a loss of coherence, yet, specific conclusions could not be drawn due to a lack of fieldwork. More recent work by Closson et al. (2010) was able to show that sinkholes in the Dead Sea are related to earthquake activity.

Newer research from Nof et al. (2013) along the Dead Sea was able to detect millimetre scale precursory subsidence occurring over a period of a few months before the collapse of sinkholes. This study used high-resolution COSMO-SkyMed X-band satellite images and a LiDAR elevation model to compensate for topography. The authors state that a semi-automatic early warning algorithm is currently under development that will serve to identify future sinkholes. This study was the first to show clear precursory deformation prior to sinkhole formation although it was limited to three sinkhole events.

Investigations of a collapse sinkhole in Louisiana proved that precursory deformation in the shape of two lobes could be measured by an airborne L-band SAR system (Jones & Blom 2013). The researchers were able to detect precursory surface deformation of up to 260 mm one month prior to the ultimate collapse. Unexpectedly, for this collapse, the surface deformation was mostly horizontal. The relative absence of vertical movement is hypothesised to be due to weak surface material flowing toward a developing subsurface failure. The authors concluded that satellite-based DInSAR, preferably with an L-band (23.8cm wavelength) sensor, would be able to provide quantitative information that can be used to predict sinkhole size and growth rate. Jones & Blom (2014) further note that the radar temporal-coherence needed for their investigation would not have been possible based on X-band and C-band systems. It should be noted that many authors have used X-band data from newer systems successfully on ground deformation events (Sansosti et al. 2014; Przylucka et al. 2015), including sinkholes (Nof et al. 2013).

A case study illustrating the potential of advanced SAR technologies for early warning systems is the retrospective SAR time series analysis of a building in the Netherlands, which failed due to abandoned mine shafts collapsing 90m below it. Chang & Hanssen (2014) found that the driving mechanism of the collapse had a long lead-time that was significantly observable by PSInSAR for up to 20 years before the failure event. The authors claim that subsurface cavity migration can be detectable at a very early stage, even when it is occurring underneath buildings, and suggest an automatic detection algorithm over sinkhole prone areas as a feasible endeavour. The precursory deformation of the building was larger in scale, ~30 m, than the actual sinkhole event, ~8 m. This study illustrates the importance of exploiting historical archives to investigate unpredictable collapse events.

One of the most successful examples of interferometry providing sinkhole early warning was a precursor detected on a road through a ground-based DInSAR (GB-InSAR) system leading to precautionary road closure (Intrieri et al. 2015). Approximately 3 mm of deformation was detected between three acquisitions three months apart leading to a warning issued to local authorities. This led to the road closure before the sinkhole formed and mitigated further damages. There was a

period of accelerated deformation of ~7 mm over one month which might have led up to a sinkhole forming had preventative measures not been taken. Importantly, it was found that the deformation basin was approximately three times larger (10 m) than the actual sinkhole event (2.5 m). This is an important consideration since it points to small-scale sinkholes being detectable by precursory basins larger than they are. Another sinkhole occurred during the investigation that was 1.5 m wide that could not be detected. The system had a 1 x 1 m resolution, higher than the typical space-borne sensor and could detect deformation of 10 x 10 pixels. This corresponds to lower detection limits discussed in Section 2.3.2 and by Massonnet and Feigl (1998). This was the only detection of sinkhole precursors occurring in carbonate geology similar to the area under investigation (Section 2.1.3). This is in contrast to the other detections over evaporite rock characterised by a larger scale and higher subsidence rate (as discussed in Section 2.1.1.). It should be noted that GB-DInSAR systems are not directly comparable to spaceborne sensors since atmospheric and topographic effects are not a factor.

DInSAR has been investigated extensively in the evaporite karsts of the USA (Jones & Blom 2013). Conway and Cook (2013) successfully used conventional DInSAR on ERS-1,2 and ALOS data to monitor and map large-scale (~1km wide and ~10 m deep) subsidence basins due to evaporite karst activity in Arizona. These DInSAR results could be used by Rucker et al. (2013) to guide *in situ* geophysical investigations to better understand the future sinkhole risk of the area. In Texas, anthropogenic activities are leading to deformation hazards in evaporites. Continuous deformation surrounding sinkholes that have already formed have successfully been monitored using Sentinel-1 (Kim, Lu & Degrandpre 2016). This shows that DInSAR is not only able to detect precursory deformation but is also suitable for monitoring post-sinkhole deformation.

In spite of the general success achieved in monitoring precursors to deformation, some studies have failed to detect precursory subsidence. Paine et al. (2012) used interferometry to observe a large sinkhole that occurred on the flank of a coastal plain salt dome in 2008. It was determined that no detectable subsidence preceded sinkhole development which, according to the authors, indicated the sudden collapse once the upward migrating void reached a depth which allowed the overlying sediments to lose cohesiveness suddenly. Rucker et al. (2013) analysed a brine well collapse in New Mexico (USA) and could not detect precursor subsidence before the event. However, a very limited data set of three images covering a timeframe of less than a year, two years before the collapse was used to generate the interferogram. Therefore, the results are not conclusive in terms of the non-detection of precursors prior to the collapse of the brine well.

Advanced time series approaches have been used to investigate sinkholes. Tomographic 4-D imaging and the SBAS was reportedly used for the analysis of sinkhole phenomena in Italy (Calo et al. 2011). Large-scale deformation monitoring on C-band data was successfully done using these approaches, discussed in Section 2.2.3, and deformation likely related to karst processes could be detected. However, no specific sinkhole event was detected. This could be because these

techniques focus on stable, coherent, pixels that reduce the spatial sampling density. Furthermore, precursory deformation could have been removed from the displacement map due to SBAS processing which removes non-linear deformation (discussed in Section 2.2.3).

Spain's Ebro Valley is another karst terrain where intensive DInSAR research has been done. Important work from the Ebro valley karst showed deformation related to sinkholes and landslides in the area (Castañeda et al. 2009; Gutiérrez et al. 2011). SBAS DInSAR was used and found to be able to detect large-scale mining related subsidence. However, no small-scale precursory deformation could be detected. Three reasons were identified to explain the non-detection including 1) that SBAS processing results in reduced resolution interferograms unable to detect small-scale sinkholes, 2) a lack of coherence in rural areas, and 3) non-linear ground motion that is associated with sinkholes (Castañeda et al. 2009). Gutiérrez et al. (2011), however, showed that DInSAR has the advantage of accurate measurements of large areas with a high spatial and temporal resolution ideal for sinkhole identification.

Recently, Galve, Castañeda & Gutiérrez (2015) assessed sinkhole activity in the Ebro valley evaporite karst using advanced DInSAR techniques to analyse their effectiveness for sinkhole risk management. Galve et al. (2015) found that DInSAR could successfully improve sinkhole inventories by detecting non-inventoried sinkholes, revising sinkhole activity levels and refining sinkhole boundaries. The study, however, concluded that DInSAR could not be used in isolation for sinkhole inventories since the technique overlooked 70% of previously mapped sinkholes in their study area, an error they attribute mainly to decorrelation effects. They found the biggest source of decorrelation was vegetation in rural and agricultural areas where there is a lack of persistent scatterers. The most reliable results came from urban areas. Using artificial corner reflectors as persistent scatterers in areas with a low PS density, as done by Yu et al. (2013), may improve the monitoring of already inventoried sinkholes in areas of high decorrelation.

An important finding by Galve, Castañeda & Gutiérrez (2015) was the maximum subsidence rates that DInSAR (using C- and L-band data) is sensitive to (17 mm/year) is much less than some active sinkholes (110 mm/year). Sinkholes smaller than 2500 m^2 could not be detected during this study due to the low spatial resolution of the chosen SAR systems. ENVISAT ASAR and ALOS PALSAR with resolutions of ~30 m used. Both these restrictions can be partially lifted by the use of higher spatiotemporal data from second generation COSMO-SkyMed or TerraSAR-X satellites (Prati, Ferretti & Perissin 2010). COSMO-SkyMed, combined with necessary LIDAR elevation data, was successfully used two years earlier by Nof et al. (2013) on small-scale, high subsidence rate sinkholes. Galve, Castañeda & Gutiérrez (2015) suggest using artificial corner reflectors as well as differential GPS, precise levelling, tiltmeter arrays and horizontal extensometer in decorrelated areas with known subsidence. Finally, the authors suggest that DInSAR should not be considered an alternative to conventional mapping methods but rather as a useful complementary approach. It is important to note that this conclusion is related to the creation of sinkhole inventory maps rather

than monitoring of sinkholes and their precursors. Further work has shown that DInSAR is capable of monitoring railway deformation over active sinkholes accurately (Galve, Castañeda & Gutiérrez 2015).

Automated detection of sinkhole precursor detection is another important future requirement for a DInSAR based early warning system, yet very little work has been done to this end. Graph-cut segmentation was used for detecting subsidence basins in sparse point cloud displacement maps derived from SqueeSAR (Stuecheli, Vaccari & Acton 2012). This paper shows that successful automated detection is possible, yet challenging due to the sparse sampling nature of PSInSAR, even when distributed scatterers are incorporated into processing (Ferretti et al. 2011). Vaccari et al. (2013) detail another automated technique for detecting subsidence basins based on a spatiotemporal model being available for the deformation feature of interest. This highlights the need for an accurate understanding of the physical nature of sinkhole precursors and the challenges due to the low density of sampling using advanced scatterer selection.

Empirical research, in contrast to modelling and simulation, is an important method for understanding sinkhole precursors (Augarde, Lyamin & Sloan 2003). DInSAR is an important tool for such investigations as precursory deformation has been detected successfully using DInSAR. These reports show that subsidence may be detected in the weeks (Jones & Blom 2013), months (Colesanti et al. 2005; Nof et al. 2013; Intrieri et al. 2015) to years (Chang & Hanssen 2014) prior to ultimate sinkhole formation. The deformation rate is typically in the order of centimetres per month and may be larger in spatial extent than the final sinkhole (Chang & Hanssen 2014; Intrieri et al. 2015). Yet sinkholes are relatively small deformation features typically less than 100 m in diameter (Kim, Lu & Degrandpre 2016). Sinkhole precursors have been reported on in different environmental conditions. Sinkholes were typically detected in evaporite geology in Spain (Galve et al. 2009), the USA (Conway & Cook 2013) and Israel (Yechieli, Abelson & Baer 2015) yet carbonate sinkholes, similar to those in Gauteng, have also been detected (Intrieri et al. 2015). Precursory deformation prior to anthropogenic cavity collapse has also been reported on (Colesanti et al. 2005). There are examples of confirmed precursory deformation leading to ultimate sinkhole collapse (Nof et al. 2013; Intrieri et al. 2015; Jones & Blom 2013). Yet other studies report on subsidence occurring on sinkhole-prone land that may be precursors to future sinkholes, but have not yet resulted in sinkholes during the time of publication (Rucker et al. 2013; Kim, Lu & Degrandpre 2016). Ongoing deformation after sinkhole collapse has also been monitored (Jones & Blom 2015; Kim, Lu & Degrandpre 2016). Case studies of successful, but also unsuccessful detections are present in literature and precursory ground deformation has been shown to be a possible, but not always present feature of sinkhole collapse (Baer et al. 2002; Paine et al. 2012; Rucker et al. 2013).

Predicting imminent sinkhole formation based on precursor subsidence detected from space is now within reach of DInSAR. However, there is still an urgent need to develop this capability

further towards the ultimate goal of an automatic sinkhole early warning system. Karst terrain creates significant engineering difficulties and there is a need to predict and mitigate damages relating to sinkholes, especially in urban environments (Stevanovic et al. 2015). DInSAR, therefore, has great potential to be a cost-effective method of monitoring urban infrastructure for deformation (Ozden et al. 2016). It can lower the risk of damages and the cost of maintenance by enabling proactive remedial work on infrastructure prone to sinkholes (Vaccari et al. 2013). Integrating DInSAR monitoring into the management of karst terrain is therefore recommended (Bruckno et al. 2015).

2.3 **SAR system considerations**

SAR interferometric techniques are able to detect ground deformation accurately, yet there are important limitations that must be taken into consideration. These limitations are inherent to the properties of the SAR system chosen for data acquisition. The most important factors are wavelength (Section 2.3.1), spatial resolution (and swath size) (Section 2.3.2), revisit time (Section 2.3.3), polarisation (Section 2.3.4) and incidence angle (Section 2.3.5). Spatial resolution and swath size are particularly dependent on acquisition mode and are therefore discussed together.

2.3.1 Wavelength

SAR satellites can operate in various wavelengths of which longer wavelengths are generally more favourable for ground subsidence measurements since decorrelation effects are reduced (Engelbrecht 2013). Commonly used spaceborne wavelengths are X-band (~3 cm wavelength), C-band (~5.6 cm wavelength) and L-band (~23 cm wavelength). Longer wavelengths are able to penetrate objects such as vegetation and interact with the ground surface, thereby reducing temporal and volume scattering coherence loss and enhancing the ground signal (Engelbrecht & Inggs 2013). Rough surface scattering is also dependent on wavelength. Surfaces with height variations less than the radar wavelength will appear smooth and lead to a low return and *vice versa* (Ferretti et al. 2007). Some authors found that detecting small-scale subsidence in very challenging areas for DInSAR due to decorrelation, such as wetlands, is only possible with longer wavelengths to avoid temporal coherence limitations (Jones & Blom 2013). Nevertheless, X-band systems are widely used for deformation monitoring, due, in part to the high-resolution and rapid revisit time of current X-band systems that compensate for temporal decorrelation (Bonano et al. 2013; Sansosti et al. 2014).

There is, however, a trade-off between susceptibility to temporal decorrelation and sensitivity to deformation between the different wavelengths. Shorter wavelengths, such as X-band, are more sensitive to deformation than longer wavelengths (Bovenga et al. 2012). A displacement of half the wavelength will result in a phase variation of 2π on an interferogram. It follows that a reduction in wavelength will lead to an increase in differential phase variation. Since X-band is approximately half the wavelength of C-band it is theoretically nearly twice as sensitive to ground movement

(Prati, Ferretti & Perissin 2010). Advanced time series stacking techniques on X-band data is able to categorise even thermal expansion of structures in an urban environment (Tomás et al. 2014). This sensitivity to small-scale deformation is expected to be important for sinkhole precursor detection.

Another wavelength consideration important to interferometry is the maximum detectable deformation gradient (MDDG). This gradient is defined by the dimensionless ratio of the pixel size to half the wavelength (Massonnet & Feigl 1998). In other words, the phase difference between neighbouring pixels (or scatterers for PSInSAR approaches) cannot exceed half the wavelength of the sensor. If the ground deformation exceeds this gradient between image acquisition, conditions for coherent interferometry is lost and the deformation cannot be measured (Jiang et al. 2011). Furthermore, challenges to unwrapping deformation exceeding 0.5 fringes and coherence challenges limit deformation measurement to less than a quarter of the wavelength in practice (Sun & Muller 2016). High deformation-rate phenomena therefore need to be sampled frequently, at high resolution or with longer wavelengths to avoid exceeding this gradient (Massonnet & Feigl 1998). The gradient is small (maximum of 1.5 cm per 3 m pixel in this study) for X-band SAR systems, and a rapid revisit time is imperative for interferometry on short wavelengths. Longer wavelengths are not as limited by the deformation gradient, and interferometry on longer temporal baselines can be successful (Sharma et al. 2016). The high spatial- and temporal resolution of typical X-band stripmap acquisition modes (Section 2.3.2) reduces the maximum deformation gradient limit.

The cycle-slicing limit is another, less significant challenge related to wavelength. It describes the limit on how fine deformation measurements can be made on the phase before slicing it any further becomes meaningless. It is not based on the discrete number of bits captured by the sensor, as in optical imagery, as raw data is combined during focusing. It is rather based on the nature of the sum of coherent and incoherent scatterers. The cycle-slicing limit generally influences accuracy by less than one millimetre and longer wavelengths are more influenced by a reduction in accuracy than shorter wavelengths. L-band theoretically has a four times lower accuracy than C-band, and C-band accuracy is two times lower than X-band (Massonnet & Feigl 1998).

Different wavelengths are also influenced by the atmospheric path differently. All wavelengths are influenced by tropospheric delays. Yet only long wavelengths, L-band in particular, are significantly prone to ionospheric path delays (Gomba et al. 2016). Such atmospheric path delays can be confused with ground deformation signals but are characterised by a large spatial extent (Hanssen 2001). They are therefore not expected to be a significant challenge to sinkhole precursor detection.

Numerous commercial satellites operate at X-band and C-band. The only commercial satellite operating on L-band is the Japanese ALOS-2. The available SAR platforms are considered in Section 2.3.6. X-band radar was preferred for this study because sensitivity to small-scale

deformation was essential. Improvements to the cycle-slicing limit and susceptibility to ionospheric noise is advantageous. However, the susceptibility to decorrelation and the small deformation gradient limit are important considerations that require a high revisit time.

2.3.2 Acquisition modes (spatial resolution and swath size)

SAR sensors are capable of acquiring data in many distinct acquisition modes. These acquisition modes are generally a trade-off between swath size (and consequently revisit time), spatial resolution and the energy and tasking requirements of the mission. Modes can generally be divided into three types with differing characteristics: ScanSAR, Stripmap and spotlight (Roth, Huber & Kosmann 2004). ScanSAR modes (equivalent mode titled TOPS on Sentinel-1) provide large area coverage by scanning several adjacent swaths with different incidence angles. This mode generally has a reduced azimuth resolution. Stripmap mode is acquired by scanning a continuous ground swath at a fixed incidence angle resulting in an image with standard image quality in azimuth. This mode provides high resolution (< 10m) and relatively large swath sizes. Spotlight images are captured by continuously illuminating an area resulting in very high resolutions (less than one metre is possible) but with very small swath coverage (Roth, Huber & Kosmann 2004). Advanced experimental modes are also tested on platforms such as TerraSAR-X's along-track interferometry capability (Moreira 2014).

The spatial resolution of a SAR imposes a fundamental lower scale limit to interferometry, as successful deformation detection cannot be accomplished on a single pixel alone using conventional DInSAR algorithms. This is due to phase noise being incorporated in an unpredictable way and the agreement by several neighbouring pixels is required to confirm displacement. In fact, Massonnet and Feigl (1998) state that deformation signals may be impossible to recognise unless it is at least 10 x 10 pixels wide. Recent work through GB-DInSAR has practically shown lower levels of detection, and a 1.5 m basin could not be detected with a 1 m resolution system while a 10 m basin could be seen (Intrieri et al. 2015). For large subsidence features, low spatial resolution sensors are suitable for analysis but if small subsidence phenomena such as individual buildings or individual sinkholes are to be monitored, then very high-resolution data are required (Schunert & Soergel 2012; Nof et al. 2013). A high spatial resolution radar data was a guiding factor in platform selection in this study since the majority of sinkholes in the study area have historically been less than 15 m in size (Richardson 2013).

2.3.3 Revisit time (temporal baseline)

SAR can penetrate clouds and it is capable of achieving a more reliable revisit time than optical sensors as it is limited principally by orbital parameters (Ferretti et al. 2011). However, reliable revisit times are still a challenge in practice due to mission and system parameters. SAR systems are power-intensive and it is challenging to operate continuously (Massonnet & Feigl 1998). Missions are carefully planned as Stripmap and Spotlight modes occupy the SAR system implying

that nearby areas cannot be monitored simultaneously. Missions generally have priority background modes, and acquisitions can be missed due to recommissioning of sensors for disaster monitoring, reducing the acquisitions in other areas (Rosenqvist et al. 2007).

Short revisiting times are important as they result in a more accurate characterisation of the subsidence phenomenon, reduction in temporal decorrelation effects and avoid exceeding the maximum deformation gradient. In areas of high rates of change or non-linear change, as may be expected of sinkholes, it is important to use as high as possible sampling resolution (Crosetto, Monserrat & Crippa 2010).

2.3.4 Polarisation

Another consideration is the polarisation of the microwave signal. SAR systems are able to transmit and receive radiation in two polarisation channels, either vertical (V) or horizontal (H). Different systems have different polarimetric modes in which data is acquired based on the combination of these channels. Single polarisation systems are able to only send and receive either horizontally or vertically (HH or VV). The HH- and VV modes are referred to as co-polarised and some systems are able to alternate between these two modes. Dual-polarimetric systems are capable of sending in one channel and receiving in both channels simultaneously (HH + HV or VV + VH) thereby adding a cross-polarised option. Quad polarised systems are capable of collecting all four polarisations simultaneously, both co-polarised channels and cross-polarised channels (HH + HV + VV + VH) (Lee, Grunes & Pottier 2001).

Radar signals interact with the macro structure and dielectric properties of the earth surface, in contrast to visible light which is more sensitive to the properties on the molecular scale (Papathanassiou & Cloude 2001). Polarised radiation in general interacts with similarly structured structures. Vertical polarisation would, therefore, interact strongly with vertical crops and have a stronger backscatter in VV modes than other polarisations. Scattering from the ground surface furthermore does not result in significant de-polarisation. If the polarised signal is depolarised by the scattering mechanism, often due to volume scatterers, a stronger return can be expected from the cross polarised modes than co-polarised modes (Engelbrecht 2013).

Horizontal send and received polarisation (HH) is often best suited for interferometric surface monitoring since the signal has improved penetration capabilities through vertically orientated vegetation, and a strong return from the ground (Engelbrecht et al. 2014). Compared to VV, HH has been found to be less sensitive to surface roughness effects. Furthermore, it results in a slightly increased coherence in urban environments (Gernhardt et al. 2010). Most operational SAR systems offer dual or quad polarisation capabilities but HH polarisation was the most suitable for this study due to its increased interaction with the ground.

2.3.5 Line of sight (LOS) and incidence angle

Spaceborne SAR is a side looking system collecting data at a specific angle from *nadir*, called the incidence angle. SAR systems need to be side-looking to be able to resolve ground scatterers in range without ambiguity. Scatterers in range are resolved by the timing of the return pulse. If a SAR was downward-looking, signals returning at the same time from the left and right would be indistinguishable. Higher incidence angles lead to a higher resolution in range since overlap is reduced between returning pulses. There is also a slight increase in incidence angle from near-range to far-range in a Stripmap image. This side-looking geometry, however, imposes unique geometric artefacts on the data; the most common challenges are shadowing, foreshortening and layover. These are outside the scope of this review, for a more detailed description see Ferretti et al. (2007). However, it should be noted that shadowing due to the LOS being obstructed, could be a challenge for detecting small-scale deformation phenomena in an urban environment.

SAR interferometry can only measure the change in range in its line of sight. Since incidence angles from spaceborne systems are relatively high, the technique is generally very sensitive towards vertical displacements (Prati, Ferretti & Perissin 2010). Three-dimensional deformation components are likely in the field, yet cannot be resolved through single pass interferometry and assumptions of displacement direction based on *a priori* information are generally done (Intrieri et al. 2015). Landslides, for example, are assumed to move in the downslope direction that can be calculated from a DEM (Crosetto et al. 2013).

SAR systems are generally polar orbiting and right looking. The same area is therefore imaged from ascending and descending passes. Interferometry between these passes is not possible due to the geometrical properties of scatterers in the resolution cells (Massonnet & Feigl 1998). However, LOS displacement of the same pixels from opposing angles provide enough information to resolve the valuable three-dimensional direction of movement (Jones & Blom 2013).

2.3.6 SAR platforms

The most commonly used satellites for spaceborne interferometric applications capture data at X-band, C-band or L-band. These SAR systems have differing characteristics resulting in some being more suitable for specific applications than others are. A table summarising the most widely used and important SAR platforms used in research is provided in Table 2.1. X-band is currently the highest frequency operational SAR imaging wavelength used on spaceborne platforms. The centre frequency used is ~ 9.65 GHz (3 cm wavelength). This research used one of the most advanced operational X-band systems available, TerraSAR-X, to detect sinkhole precursors.

TerraSAR-X (TSX) was launched in 2007 (Pitz & Miller 2010) and was joined by TanDEM-X (TDX) in 2010 (Krieger et al. 2013). The joint operational lifetime of 5 years was reached in 2015 and the extended mission is expected to last until at least 2018 (Schättler et al. 2015). It is planned that the TerraSAR-X pair will be joined by a functional identical SAR titled TerraSAR-PAZ during 2016 to

ensure mission continuation and reduced revisit times (Airbus Defence and Space 2014). This mission however delayed by at least three years and no launch date has been specified during the time of writing (Clark 2016). The TSX/TDX pair is orbiting in a sun-synchronous 11-day repeat orbit (Pitz & Miller 2010). Fully polarimetric data can be captured in experimental modes. Data can be acquired in three general modes including, ScanSAR, Stripmap and Spotlight mode. ScanSAR can collect in normal or Wide ScanSAR modes with respective swath sizes of 150 km x 100 km and 200 km x (194km – 266km) as well as respective resolutions of 40 m and 18 m. Stripmap mode has a swath size of 50 km x 30 km and resolution of 3 m. There are four spotlight modes with swath sizes from 10 km x 10 km down to (2.5 km – 2.8 km) x 6 km and resolutions from 1.7 m to 0.24 m (in azimuth) (Schättler et al. 2015).

Table 2.1 Details of the most important SAR systems available for SAR research (adapted from Ozden et al. (2016)).

Satellite	Agency- Country	Year of Launch	Band	Resolution (m)	Polarization	Revisit Time (days)
ERS-1	ESA/Europe	1991	C	5, 25	VV	35
ERS-2	ESA/Europe	1995	C	5, 25	VV	35
JERS-1 SAR	NASDA/Japan	1992	L	6, 18	HH	44
ENVISAT-ASAR	ESA	2002	C	10, 30	dual	3
RADARSAT-1	CSA/Canada	1995	C	8, 8	HH	5
RARDASAT-2	CSA/Canada	2007	C	3, 3	quad	24
ALOS-PALSAR	JAXA/Japan	2006	L	5, 10	quad	7
ALOS-PALSAR-2	JAXA/Japan	2013	C	10, 100	quad	14
Cosmo-SkyMed (4)	ASI/Italy	2007	X	1, 1	dual	5
TerraSAR-X	DLR/Germany	2007	X	1, 1	quad	11
TanDEM-X	DLR/Germany	2009	X	1, 1	quad	11
RISAT-1	ISRO/India	2012	C	3, 3	quad	25
HJ-1-C	China	2012	S	5, 20	VV	31
Sentinel-1A	ESA/Europe	2014	C	9, 50	dual	12

Natural hazard response from spaceborne sensors is continually improving. More sensors are becoming available and data delivery times are decreasing leading to major opportunities for satellite based emergency mapping (Voigt et al. 2016). Emergency mapping relates to post-event assessment, yet the same advances in technology will also aid early-warning efforts. Several current and future SAR satellites missions (e.g., COSMO-SkyMed, RADARSAT and Sentinel-1) are designed as constellations of SAR sensors. Relative to single satellite systems, such constellations provide greater spatial coverage and temporal sampling. This results in higher revisit times and higher coherence between acquisitions (Milillo et al. 2015). Moreover, future-engineering advances are expected to lead to SAR characteristics at least an order of magnitude over current systems (Moreira 2014). This new generation of SAR satellites shows great potential for ground deformation measurements and novel applications such as sinkhole precursor detection (Bonano et al. 2013; Sansosti et al. 2014). The data and processing methods followed in this study to investigate sinkhole precursors will be presented in the next chapter.

Chapter 3
Data and methods

This chapter describes the SAR system selection criteria with particular reference to the SAR considerations outlined in Section 2.3 and the specific properties of sinkholes in the study area presented in Section 2.1.3. The primary data used are introduced in Section 3.1.1. A detailed description of methods for data processing follows (Section 3.1.2). Ancillary data used during processing and analysis is discussed in Section 3.2. Section 4.1 notes important considerations regarding the reliable interpretation of interferograms for identifying deformation.

3.1 SAR data and processing

This section describes the SAR data used in this study as well as the methods used for deriving interferograms and displacement maps from the data.

3.1.1 SAR data

The characteristics of available SAR sensors, including the wavelength, resolution, polarisation and revisit frequency were presented in Section 2.3. The selection of the optimal sensor and data for DInSAR monitoring of deformation prior to sinkhole development are governed by the characteristic properties of the deformation features expected. During this study, properties that would lead to the highest probability of detecting a sinkhole event, in the study area and during the observation period, were deemed critical.

The small size (<15 m) of typical sinkholes in the area under investigation implies that spatial resolution is a critical consideration for successful detection. Interferometric measurement on a single pixel is not meaningful (Section 2.3.1) and this imposed a major constraint on SAR data selection. Considering deformation events of 15 m or smaller in extent, a minimum resolution of 5 m or better would be required. An important finding to highlight here from recent sinkhole precursor detections (Section 2.1.2) has been that precursory deformation may be larger than the actual sinkhole event and 15 m serves as an estimate. Nevertheless, spatial resolution is a trade-off with swath size as discussed in Section 2.3.2. Since the exact location of sinkholes cannot be predicted and only locations of historical sinkholes and known dolomite (see Figure 1.2) were available a large swath size was important.

This study was constrained to a one-year observation period between January 2015 and January 2016. A rapid revisit time was important to ensure a high temporal sampling rate and to reduce the impacts of temporal decorrelation (see Section 2.2.2.3). Optimal wavelength was a more challenging decision as many factors are wavelength dependent (see Section 2.3.1). A high sensitivity to deformation was important since sinkhole precursor deformation has been found to have a small magnitude (see Section 2.2.5). However, expected deformation rates in relation to the

deformation gradient imposed by the sensor wavelength had to be considered. Furthermore, sensitivity to temporal decorrelation is wavelength dependent (see Section 2.3.1). Longer wavelengths would be more suitable in terms of temporal decorrelation and deformation gradient yet shorter wavelengths are more sensitive to deformation.

Ultimate selection was a trade off that weighed spatial resolution, appropriate swath size, revisit time and wavelength in the context of available satellites. The twin TerraSAR-X/TanDEM-X satellites were selected for this study to provide the greatest chance of detecting sinkhole precursors. Its main advantage was its high spatial resolution (3 m) and large enough swath size (50 km x 30 km) in Stripmap mode. It has a relatively high revisit time of 11 days. X-band furthermore is the most sensitive wavelength to deformation, however; increased decorrelation noise imposes limitations accurate measurement. The relatively high revisit time was expected to compensate for X-band's susceptibility to decorrelation. HH polarisation and a 40.9° incidence angle were used to ensure optimal ground scattering (see Section 2.3.4). The TerraSAR-X radar is right-looking radar and since data was captured on the descending pass, it was facing west. Data was captured at approximately 4 a.m., this is advantageous for avoiding atmospheric phase contributions since it is known that the atmosphere is more stable during the night (Massonnet & Feigl 1998).

Many other SAR platforms are currently available, as presented in Section 2.3.6. The most feasible systems that were decided against were ALOS PALSAR, RADARSAT-2, and Sentinel-1. Sentinel-1's background interferometric monitoring mode (TOPS) has a range-azimuth resolution of 5 m x 20 m. This implies that it will not be suitable for small-scale deformation phenomena. Although RADARSAT-2 fine beam data can be provided at slightly higher than 5 m resolutions resolution, it has a revisit time of 24 days, which makes it inadequate for early warning requirements. The ALOS-2 L-band system has a 14-day revisit time and resolutions of up to 3 m yet tasking the satellite within the time constraints of this study was not feasible.

Data were delivered in the "Single look Slant-range Complex" (SSC) processing level. Data were acquired for a full year from 29th January 2015 to 27th January 2016. Table 3.1 provide a full list of the acquisition dates from TerraSAR-X and TanDEM-X respectively. The acquisition footprint covers approximately 50 x 30 km^2 of the Pretoria urban area. A map of the footprint, as well as the location of known dolomite, is shown in Figure 1.2 in Section 1.5. It can be seen from the map that areas to the south of the footprint would be at the highest risk of sinkhole formation due to the presence of dolomite in proximity to built-up areas.

Table 3.1 The date and interferometric properties of the SAR images acquired for the study.

ID	Acquisition date	SAR Platform	Temporal baseline (days)*	Perpendicular baseline (metres)*
1	2015/01/29	TerraSAR-X	11	-217.0
2	2015/02/09	TanDEM-X	77	365.2
3	2015/04/27	TerraSAR-X	11	-342.0
4	2015/05/08	TerraSAR-X	33	23.7
5	2015/06/10	TerraSAR-X	11	41.1
6	2015/06/21	TerraSAR-X	11	10.3
7	2015/07/02	TerraSAR-X	11	69.2
8	2015/07/13	TerraSAR-X	33	14.4
9	2015/08/15	TerraSAR-X	22	3.7
10	2015/09/06	TerraSAR-X	11	-73.6
11	2015/09/17	TerraSAR-X	11	-4.7
12	2015/09/28	TerraSAR-X	11	-192.8
13	2015/10/09	TanDEM-X	11	-12.9
14	2015/10/20	TanDEM-X	11	295.8
15	2015/10/31	TerraSAR-X	11	-271.8
16	2015/11/11	TanDEM-X	11	176.4
17	2015/11/22	TanDEM-X	11	-184.7
18	2015/12/03	TanDEM-X	11	-71.7
19	2015/12/14	TerraSAR-X	22	57.3
20	2016/01/05	TanDEM-X	22	118.6
21	2016/01/27	TerraSAR-X	N/A	N/A

Note: *Relative to the following acquisition.

All the images were interferometrically compatible (same imaging geometry, see Section 2.2.2.1). Interferometric pairs were generated over consecutive intervals resulting in pairs with the shortest possible revisit time covering the entire period. The temporal-, as well as perpendicular, baselines for each image pair are summarised in Table 3.1.

The lowest temporal baseline was 11-days. Nevertheless, six image pairs were captured at longer temporal baselines, three pairs with 22-day temporal baselines, two pairs with 33-day temporal baselines and one pair with 77-day temporal baselines. The gaps in data acquisition were likely due to satellite tasking conflicts. The critical perpendicular baseline for TerraSAR-X single polarisation strip map scenes is approximately 6 km (Engelbrecht 2013) (see Section 2.2.2). All pairs had a short perpendicular baseline relative to the critical baseline with an average perpendicular of 172 metres and a maximum of 342 m.

3.1.2 Differential interferometry processing

Conventional differential interferometry (DInSAR) processing was used to derive interferograms, coherence images and surface displacement maps of the area under investigation. Processing was done using Gamma remote sensing programs (Gamma Remote Sensing 2011) within a dedicated automated script. This resulted in the reliable, systematic and efficient processing of the dataset. Consecutive master and slave acquisitions are the main input to the script. A high-

resolution (5 m) external DEM was the main ancillary data set needed for processing. Figure 3.1 illustrates the data processing steps, the main inputs, intermediate results as well as output maps.

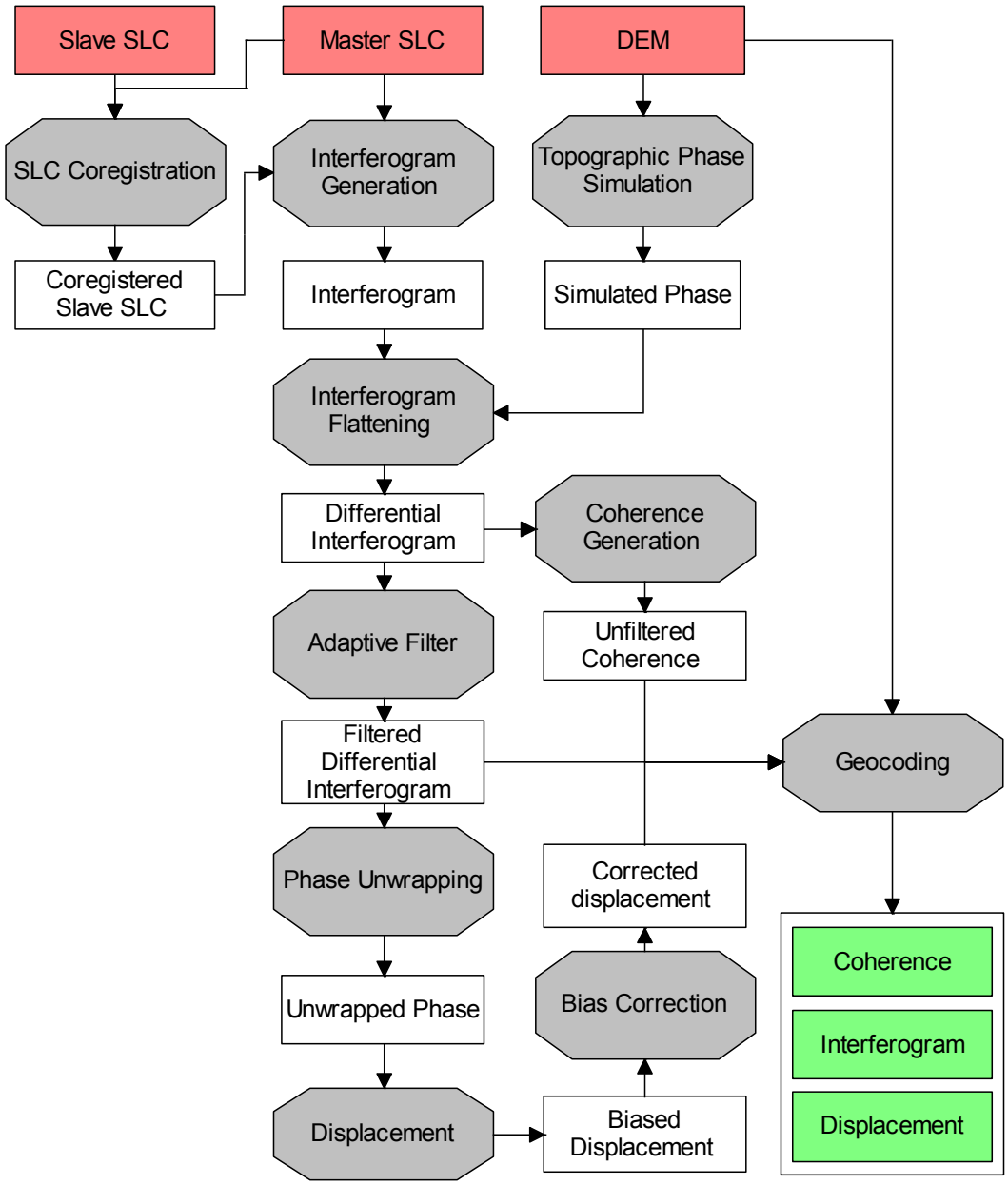

Figure 3.1 Automated processing workflow for two-pass differential interferometry used during this study.

During processing, the master and slave SLC images were imported into the Gamma processor. To maintain a sensitivity to small-scale deformation phenomena, full resolution interferometric processing was chosen and no multilooking (spatial averaging) was applied (Calo et al. 2011). Prior to interferometric processing, the master and slave images were co-registered to sub-pixel accuracy. A coregistration accuracy of less than 0.2 pixels is required to maintain interferometric phase coherence for deformation measurements (Hanssen 2001). An accuracy of 0.2 pixels would lead to a 5% loss of interferometric correlation (Gamma Remote Sensing 2011). The intensity cross-correlation accuracy achieved during processing was less than 0.1 pixels, for all interferometric pairs.

Following image co-registration, the interferogram was generated by calculating the complex conjugation of the phase components of master-slave pairs. The resulting interferogram contains a magnitude and phase component. The magnitude is the correlation between the two images and the phase presents the change in phase between the master and slave scenes. It is important to note that the interferogram at this stage of processing includes a phase contribution due to the curved earth, topography, surface displacements, atmospheric delays as well as phase noise (Section 2.2.2.1)

To remove the topographic and flat earth components, a process known as interferogram flattening was performed. The flattening process makes use of an external DEM to model the phase contribution to topography, which is known as the synthetic phase. This simulated image could was then subtracted from the interferogram resulting in a differential interferogram.

The differential interferogram was now a function of surface displacement, atmospheric delays (tropospheric and ionospheric) and phase noise (residual fringes from inaccurate orbits, thermal noise, temporal decorrelation *etc*.). Interferometric coherence was calculated to provide an assessment of the phase noise contained in the interferogram (see Section 2.2.2.3). Coherence maps were calculated from the unfiltered, instead of filtered, interferograms to preserve spatial resolution. Coherence was a secondary output used for interpretation of the results and was not directly needed for deformation detection.

The differential interferograms were then filtered using a Goldstein filter with adaptive window sizes to minimise speckle noise effects (Goldstein & Werner 1998). The resulting filtered differential interferogram presents the phase contribution due to surface deformation (assuming negligible atmospheric phase contributions) and is measured between $-\pi$ and $+\pi$. Phase unwrapping (explained in Section 2.2.2.2) was performed to calculate the correct multiple of π to convert the wrapped phase presented by the filtered differential interferogram to a continuous phase surface representing displacement. The minimum-cost flow unwrapping technique based on global optimisation of the solution was applied. The full details of the algorithm and the phase unwrapping process are available in Wegmüller et al. (2002).

Displacement maps were generated from the unwrapped interferograms considering the wavelength of the sensor. A phase ramp of 2π is equal to half the radar wavelength (1.5 cm for TerraSAR-X). It is important to note that the deformation is measured in the Line of Sight (LOS) direction of the satellite. Therefore, the LOS deformation vector was converted to a vertical deformation vector. This is based on the assumption that deformation expected for local precursory deformation would be primarily in the vertical direction due to the subsiding nature of sinkholes, resistant roof strata, as well as the relatively shallow depth of susceptible dolomite in the study area (see Section 2.1.3).

During the phase unwrapping, prior to displacement map generation, an arbitrary point was selected as the zero displacement starting point to enable automated processing. Since all deformation will be relative to this point, it was important that this pixel itself did not undergo deformation to enable absolute displacement measurement. However, this arbitrary origin selection led to a constant displacement bias in certain image pairs that led to possible minor discrepancies in displacement magnitude calculation between pairs. This bias was corrected by assuming that the average displacement of the entire acquisition footprint is zero. This is believed to be a valid assumption since no large-scale deformation is known to be present in the study area. It was found that the total frequency distribution of the displacement maps follows a Gaussian distribution and that the distribution can, therefore, be normalised by subtracting the mean from the entire scene. The resulting unwrapped phase images were thereby corrected from relative to absolute deformation. For most cases, the mean was centred on zero and it did not affect the results significantly. In the extreme cases, the bias was in the order of fewer than 2 centimetres. The discrepancies were likely due to the low coherence of the arbitrary starting point, or influence from the atmospheric phase screen (see Section 2.2.2.1).

Geocoding of the main products using the external DEM was the final step of the processing script. Geocoded interferograms were the primary output of processing as these were investigated for deformation fringes. Geocoded displacement and coherence maps were also created. Geocoding resulted in square pixels with a 2.7 m resolution. Due to TSX's precise orbital information pixels are absolutely georeferenced to within 0.5 m – 1 m (Wegmüller et al. 2008) and the spatial location of deformation was known to a high degree of accuracy.

3.2 **Ancillary data**

The result of primary data processing included three geocoded products, namely the filtered differential interferograms, coherence generated from the unfiltered interferograms and the bias-corrected vertical-displacement maps. The interferograms were visually inspected systematically for fringe patterns due to deformation. To determine if DInSAR techniques could detect precursors to sinkhole development, the results were considered in conjunction with the known sinkhole events recorded in the CGS inventory by overlaying their locations within a Geographic Information System (GIS) (Table 3.2).

An accurate, high resolution DEM is important during interferometric processing for the removal of the topographic phase, as discussed in Section 2.2.2.1, as well as geocoding. The Stellenbosch University Digital Elevation Model (SUDEM L2) (Van Niekerk 2014) was used for processing. The DEM has a 5.3 m resolution, 10.2 m vertical RMS error and is an integration of the SRTM-1 and the South African national contour, point height data sets (Van Niekerk 2014). The SUDEM is referenced to the WGS1984 ellipsoid with the EGM96 geoid added and, since it is the convention for satellite orbital vectors to be referenced only to an ellipsoid, it had to be transformed (Leprince

et al. 2007). The EGM96 Geoid was therefore subtracted. Geoid removal is an essential requirement for the external DEM used during interferometry to ensure that the same reference frame is maintained between satellite orbit data and ancillary spatial data.

The Council for Geoscience (CGS) maintains a sinkhole inventory database with recent sinkhole events reported by various authorities. This database was used to guide analysis and assess the accuracy of deformation detection. Events from the sinkhole inventory coinciding with the acquisition footprint and timeframe is presented in Table 3.2. The inventory provides both the approximate location of sinkhole events and, where available, the date and size of the sinkhole and the associated triggering mechanism. It should be noted that the records in this inventory are frequently incomplete due to limited access to the site location or incomplete observations. Specific limitations are noted in the "comments" column provided in Table 3.2. Sinkhole location and frequency data are sensitive information mainly due to the possible negative effect on property values (Oosthuizen & van Rooy 2015). The sinkhole inventory is therefore not available to the public, and conversely, it is expected that some events were not documented in the inventory. Additionally, due to operational sensitivity sinkhole coordinates are not shown.

Table 3.2 Sinkhole inventory for the study area between January 2015 and February 2016.

Unique ID	Date	Type	Possible cause	D_x (m)	D_y (m)	D_z (m)	Comments	Source data
A1	Mar 2015	Sinkhole	Leaking pipe	N/A	N/A	N/A	N/A	Martin Van Der Walt
A2	2015	Subsidence	Leaking pipe	16	4	0.2	N/A	A. Sudu (CoT), CGS site visit 23 November 2015
A3	2015	N/A	Leaking pipe	N/A	N/A	N/A	Could not see past the fencing	A. Sudu (CoT), CGS site visit 23 November 2015
A4	2015	Subsidence	Leaking pipe	N/A	N/A	N/A	N/A	CGS site visit 21/01/2016
A5	3 Jan 2016	Sinkhole	Leaking pipe	20	13	9	N/A	J. van der Merwe. CGS site visit 21/01/2016
A6	Jan 2016	Sinkhole	Leaking pipe	6	3	2	N/A	A. Sudu (CoT), CGS site visit 3 February 2016
A7	29 Jan 2016	Sinkhole & Subsidence	Leaking sewer pipe	N/A	N/A	N/A	Have not verified position	A. Sudu (CoT)

Source: Council for Geoscience

Notes: "D_x" is the length of the major axis, "D_y" is the length of the minor axis and "D_z" the depth of the deformation. "CoT" is the City of Tshwane municipality. Information not provided is marked as not available (N/A).

A timeline is provided in Figure 3.2 to provide an overview of the timing of the sinkhole events recorded in the inventory and data acquisition dates. The uncertainty ranges describe the possible period of occurrence for the sinkhole, based in the uncertainty in the recorded dates. It is apparent that there are significant uncertainties regarding the date of sinkhole formation recorded in the sinkhole inventory. The exact date of only two sinkhole events from the inventory is known (indicated as diamonds on Figure 3.2). The uncertainty range for the events without exact dates is illustrated by the dotted bars. The ranges are dependent on how well constrained the recorded "date" was and considers the date of "field visits", if noted, as the latest possible date of the event. The timeline further reveals the SAR acquisition frequency achieved over the study. SAR data were not frequently acquired during the first 5 months of acquisitions with only four images available. However, reliable acquisitions, separated by the minimum revisit time of 11 days, were collected after June with the exception of July and August, when only three images were captured.

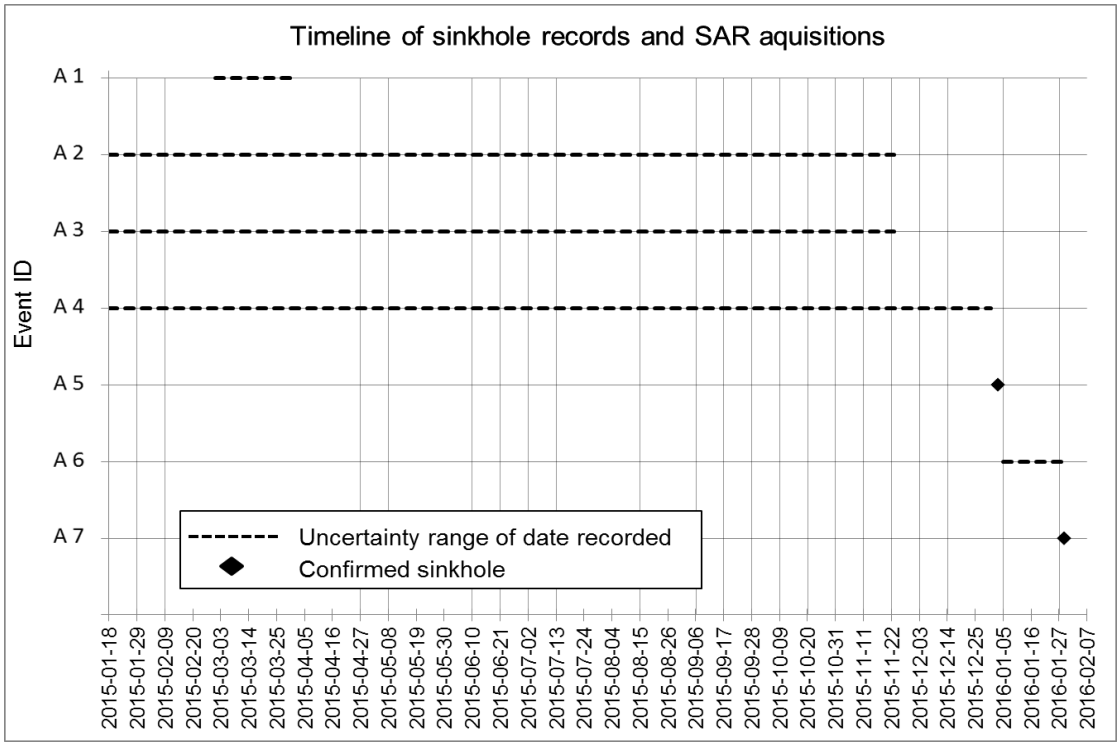

Figure 3.2 A timeline of data acquisitions and sinkhole events. Events A1 to A7 correspond to events discussed in Chapter 4. SAR acquisition dates are represented by vertical bars.

Ancillary data used to aid interpretation of the interferometric results will briefly further include a geological map, rainfall data, enhanced vegetation index (EVI) time series and high-resolution optical imagery. The geological map indicating the location of known dolomite was acquired from the Council for Geoscience (CGS) to aid in acquisition footprint selection and visual deformation detection. Daily rainfall data for the period January 2015 to January 2016 were acquired by the South African Weather Service at the Pretoria UNISA station. This station is located approximately in the centre of the southern part of the footprint between Pretoria and Centurion as shown in Figure 1.2. It is assumed that the station at UNISA provides a suitable approximation of rainfall

events during the study period. The EVI time series is based on monthly MODIS data spanning January 2015 to January 2016 and was generated through the WAMIS web-based application (Meraka 2016). EVI is a vegetation index sensitive to chlorophyll as well as canopy structural variations providing an indication of the vegetation phenology of the area. EVI was calculated for a 500m pixel in a naturally vegetated area in the Groenkloof nature reserve. This reserve is located in close proximity (<5km) to the rainfall station used and serves as an indicator for the area's vegetation phenology. The high-resolution aerial imagery was accessed through the ArcGIS Online service and used for providing an indication of the surface conditions. This optical data (natural colour data captured at the visible red, green and blue wavelengths) was originally collected by the National Geospatial Institute during airborne campaigns between 2008 and 2012 and has a resolution of 0.5 m (South Africa 2016).

Chapter 4
DInSAR results

This chapter presents the results of the DInSAR analysis (Objective 1) and the comparison of detected deformation with known sinkhole events (Objective 2). The chapter is broadly divided into three parts. Section 4.1 outlines considerations for the correct interpretation of the DInSAR results to identify the deformation phase component. Section 4.2 presents the deformation results associated with each of the confirmed sinkhole events in the CGS database. In Section 4.3, deformation events not captured in the database but detected during this study are shown.

4.1 Interpretation of DInSAR outputs

The theory behind the factors contributing to a change in phase on differential interferograms is discussed in Section 2.2.2.1. This however, has practical implications for identifying deformation on the DInSAR outputs, which will be outlined in this section with an example from the results. The differential interferograms, in theory, contained only the phase contribution due to surface displacement. However, residual phase contributions due to errors in the input digital elevation model, as well as atmospheric phase delays could also affect the results. The atmospheric phase screen is characterised by spatial extents larger (+ 100 m) than the deformation related to sinkholes investigated in this study and did not impose significant challenges. With the exception of possible contribution to the slight global displacement bias that had to be corrected for, noted in Section 3.1.2. However, topographical phase was often encountered and will be discussed briefly.

A discrepancy between the terrain model used and the interferogram can lead to fringes on the interferogram similar to deformation fringes (as discussed in Section 2.2.2.1), and a thorough understanding and analysis was therefore needed to identify it. Residual topographical phase contributions could be identified by considering the suspected area over the entire time series of interferograms. The topographic phase location and spatial extent remain constant over the temporal stack while the fringe frequency on each interferogram depends on the baseline of the pair (see Section 2.2.2.1) (Massonnet & Feigl 1998). The recent aerial imagery could also be used to identify topographic features, such as hills or quarries, and correlate their extents with interferometric fringes and confirm their relation to topography.

An example of a false positive detection due to topography is shown in Figure 4.1. There is a phase fringe feature occurring over the full-time series of interferograms. Four of these interferograms over the same are shown as an example. A fringe pattern is visible with the same spatial extent throughout the time series. The interferograms span from 2015/04/27 to 2016/01/27 and are in order of increasing baseline with increments of ~ 100 m (A to D). The perpendicular baseline is shown on the images. The fringe frequency increases as the baseline increases. Note how the feature is still detectable in the very noisy (due to a low coherence) 2015/01/05 to

2015/01/27 interferogram (B). Upon inspection of the area through aerial imagery and a comparison with the SUDEM's hillshade, it can be seen that a mine tailings dam has been built here resulting in a topographical contribution to phase not modelled in the SUDEM.

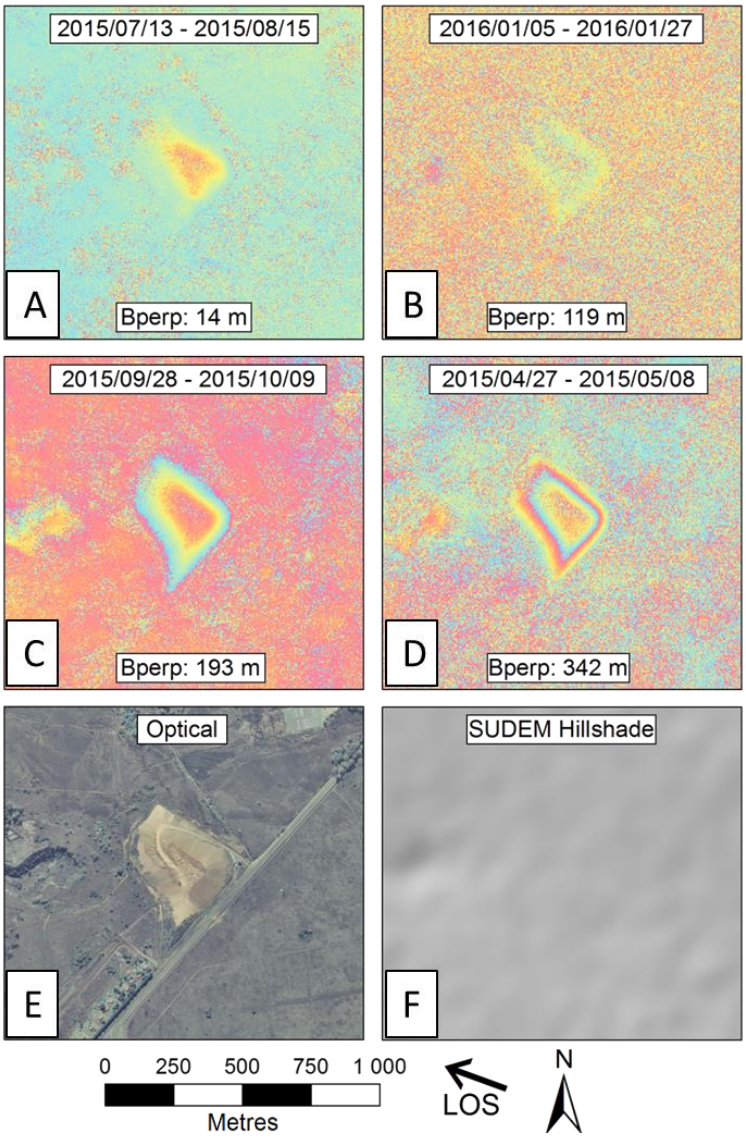

Figure 4.1 An example of baseline-dependant fringe pattern on interferograms characteristic of topographical phase residue (A, B, C & D). In this case, the fringe pattern is due to topographical variation not modelled in the DEM (F). Inspection of the aerial imagery shows that this is the result of a mine tailings dam (E).

This example illustrates the topographical sensitivity of DInSAR and its relationship to perpendicular baselines. Furthermore, it is shown how a time series of interferograms and ancillary data was important to reliable interferogram interpretation. Once phase contributions from sources other than deformation were known, it was possible to identify phase changes related to deformation reliably. The most important characteristics are that deformation phase is not related to the perpendicular baseline and is unlikely to be present in the same spatial extent across the entire interferogram stack. It was also expected to be similar in size to known sinkhole events in the study area, and therefore much smaller than typical atmospheric features.

4.2 Sinkhole inventory events and DInSAR observations

During the DInSAR observation period, seven sinkhole events, A1 to A7 as outlined in Table 3.2, were recorded by the Council for Geoscience. It should be noted that in some cases the size of the sinkhole or subsidence feature could not be recorded due to a lack of access to the site where the incident occurred. There are also significant uncertainties associated with the exact date of the incident as shown in Figure 3.2. Where the exact position of the feature could not be verified by field observations, approximate locations were provided. For each of the sinkhole events, the DInSAR results were examined to determine if precursory deformation could be observed. The time series of interferograms prior to and following each of the sinkhole events along with relevant ancillary data are provided in Sections 4.2.1 to 4.2.7 below.

4.2.1 Event A1

Event A1 was triggered by a leaking water pipe and occurred on the road in a residential area. The sinkhole was observed in March 2015, although the exact date of the incident was not indicated. The sinkhole dimensions were also not reported. Three SAR scenes covering the approximate period prior to, and during, sinkhole formation were available and were captured on 2015/01/29, 2015/02/09 and 2015/04/27 respectively. However, no scenes were captured in March 2015, the period during which the sinkhole formed. The differential interferograms, created between 2015/01/29 and 2015/02/19 as well as between 2015/02/19 and 2015/04/27 are presented in Figure 4.2 A and B respectively. The differential interferograms revealed that no deformation-related fringes were observed near the sinkhole location. However, the irregular temporal frequency of data acquisitions created significant uncertainty. The earliest data was only captured approximately a month before the event was recorded and precursory deformation could have occurred earlier than the first acquisition on 2015/01/29. Furthermore, since no data was captured during the month of March 2015 there was no measurement possible immediately prior to the event. It is hypothesised that, if SAR data between 2015/02/09 and 2015/04/27 would have been available, precursors may have been detected.

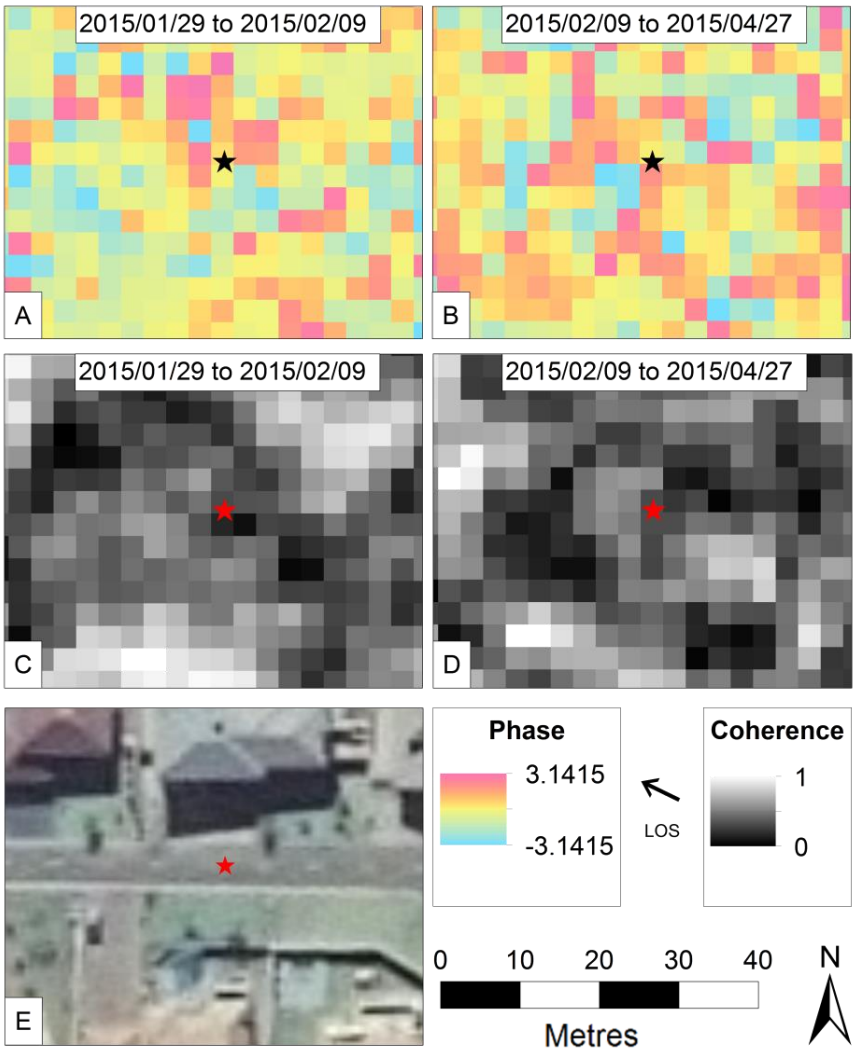

Figure 4.2 Interferograms of data available prior to, and during, event A1's sinkhole formation show no deformation fringes (A & B: differential interferograms; C & D: associated coherence maps; E: aerial photo). Coherence maps of the same area (C and D) provide an indication of phase return stability over the period. Aerial imagery (E) of the area of interest before the sinkhole occurred is shown for context.

The interferometric coherence, displayed in Figure 4.2 C and D, reveals that coherence was spatially and temporally variable over the area. The sinkhole was recorded on the road, and the immediate area where the sinkhole was recorded had a consistent coherence of less than 0.3. The high-resolution aerial photograph of the area (Figure 4.2 E) revealed that the area was relatively clear of vegetation that could cause signal decorrelation. Therefore, the low coherence could be attributed to low radar signal returns from the relatively smooth paved road. In the case of the 2015/02/19 and 2015/04/27 interferometric pair, the high temporal baseline (77 days) may also be responsible for temporal decorrelation leading to low observed coherence values.

Furthermore, since the dimensions of the event were not reported, it is possible that the precursory deformation was too small in spatial extent to be detectable by DInSAR. Further information obtained from an insurance company revealed that geotechnical drilling and excavations of the surrounding area were performed in the months after the sinkhole event (see a photo of the works

in Figure 4.3). The area affected by this operation covered approximately 30 m^2. Drilling further revealed a 30 m deep cavity located just 2 m under the surface.

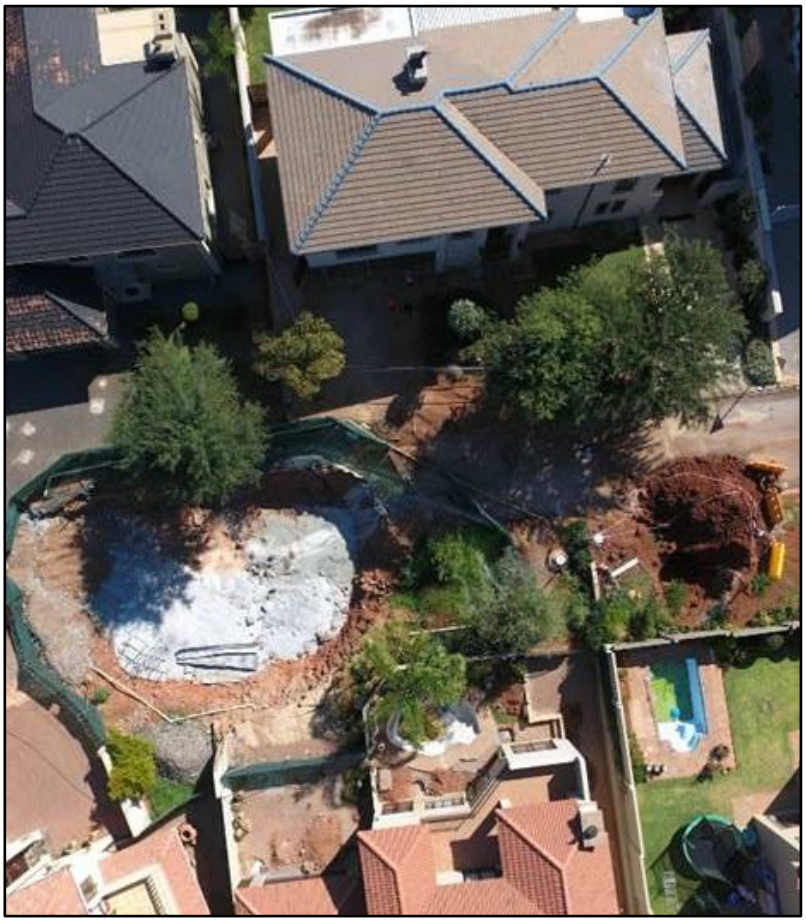

Photo: OUTsurance

Figure 4.3 Aerial imagery captured after the sinkhole event A1 formed showing the extensive excavation works done on the surrounding area following the sinkhole event.

4.2.2 Event A2

Inventory item A2 was a subsidence event 0.2 m deep and 16 m by 4 m in diameter, along the major and minor axis respectively. The specific date of sinkhole formation is unknown although it was recorded during a field visit on 23 November 2015 suggesting formation before 23 November 2015. A leaking pipe is suspected of causing the subsidence. Figure 4.4 is a high-resolution aerial photograph indicating the approximate location of the event as a red circle. The position of the event is indicated to be at a street intersection with some large trees immediately to the south and east of the feature. The look direction of the sensor, also indicated in Figure 4.4 suggests that it is possible that the trees are obstructing the direct line of sight to the area of interest on the ground.

Figure 4.4 Aerial imagery indicating the location of sinkhole event A2 with a red circle. The circle's diameter corresponds to the reported major axis of the event.

The time series of interferograms from January 2015 to 3 December 2015 is provided in Figure 4.5. No deformation-related fringes are observed on these interferograms. Since the exact period of the subsidence event is not provided, an assessment of the potential causes of non-detection of precursory deformation is difficult. It is possible that the deformation took place over a period where interferometric coherence was low. Furthermore, the presence of trees in the line-of-sight of the sensor may be obstructing the view of the surface, leading to vegetation decorrelation. If this is the case, the situation can be avoided by using longer wavelength radar to penetrate foliage. However, since the sinkhole is location is also associated with a road surface, low radar backscatter return resulting in low interferometric coherence could also be expected (similar to event A1). In this case, the low signal return due to smooth paved surfaces would be exacerbated if long wavelength data were used.

The spatial extent of the recorded event adds a further challenge to DInSAR detection. The deformation basin is an oblong shape with the length of the major and minor axis being 16 m x 4 m. The interferogram resolution is 2.7 metres and since deformation detection relies on corresponding neighbouring pixels, the fringe pattern would only be detectable on the major axis and not the minor axis. This would not result in a fringe pattern characteristic of deformation and would be indistinguishable from noise.

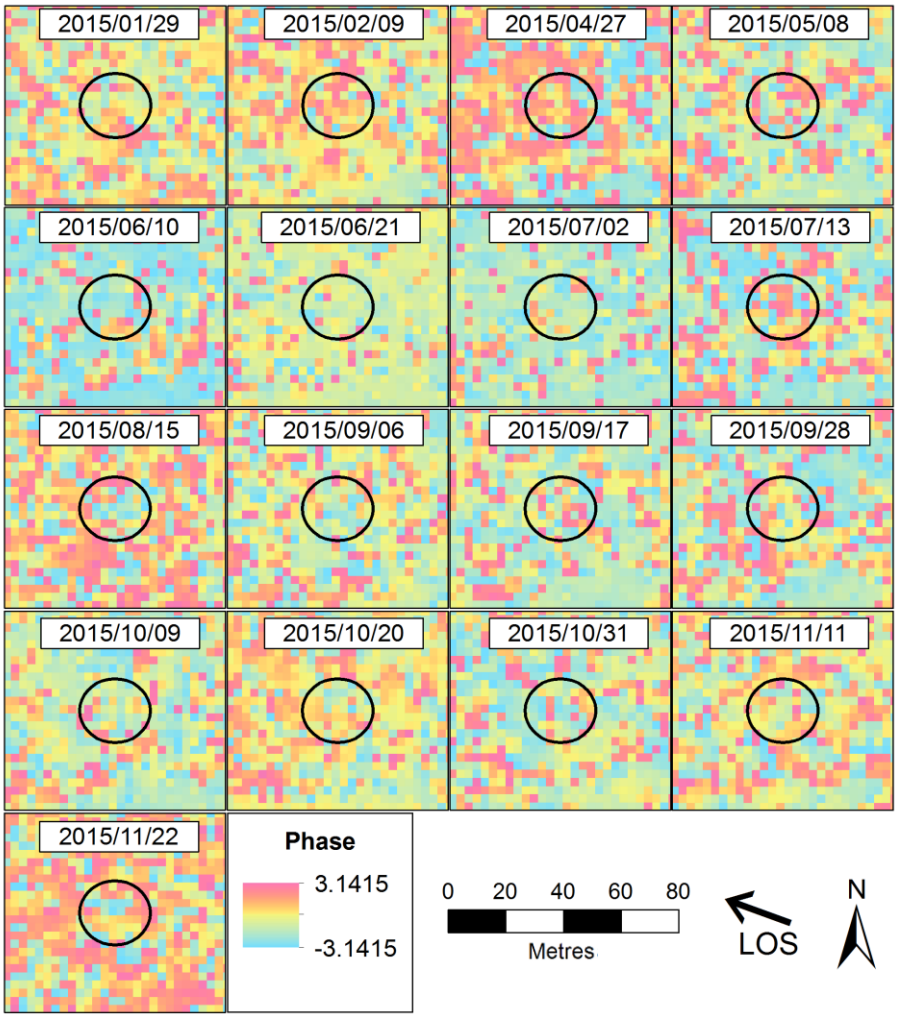

Figure 4.5 Interferograms for the area round event A2 with the sinkhole and its approximate extent indicated with a black circle. Only the master date for each image pair is provided, the slave date of each image corresponds to the master date of the following image. The final slave date for the interferogram with the 2015/11/22 master is 2015/12/03.

4.2.3 Event A3

Inventory item A3 was recorded by the Council for Geoscience after a City of Tshwane site visit on the 23rd of November 2015. The specific date of the event is not specified although it is believed to have occurred during 2015 as the result of a leaking pipe. The records indicate that access to the site was not possible and, consequently, the size and depth of the feature were not recorded.

High-resolution aerial photographs (Figure 4.6) of the area suggest that the event occurred in an established residential suburb with lush trees. The time series of interferograms for the event is provided in Figure 4.7. Similar to event A2, no deformation related fringes could be observed. The uncertainties associated with the location, magnitude, spatial extent and timeframe of the deformation makes it difficult to investigate the cases of the non-detection of deformation related to the event. However, it is probable that the trees that are prevalent in the area are limiting the signal interaction with the surface. X-band radar interacts primarily with the vegetation canopy and is

consequently unable to penetrate foliage sufficiently. Since the majority of sinkhole events in Gauteng are less than 15 m in size (Section 2.1.3), it is also possible that the dimensions of the deformation feature were smaller than the 10 x 10-pixel limit imposed by conventional DInSAR measurements.

Figure 4.6 Aerial imagery indicating the approximate location of sinkhole event A3 (red star). The SAR line of sight (LOS) direction is also provided.

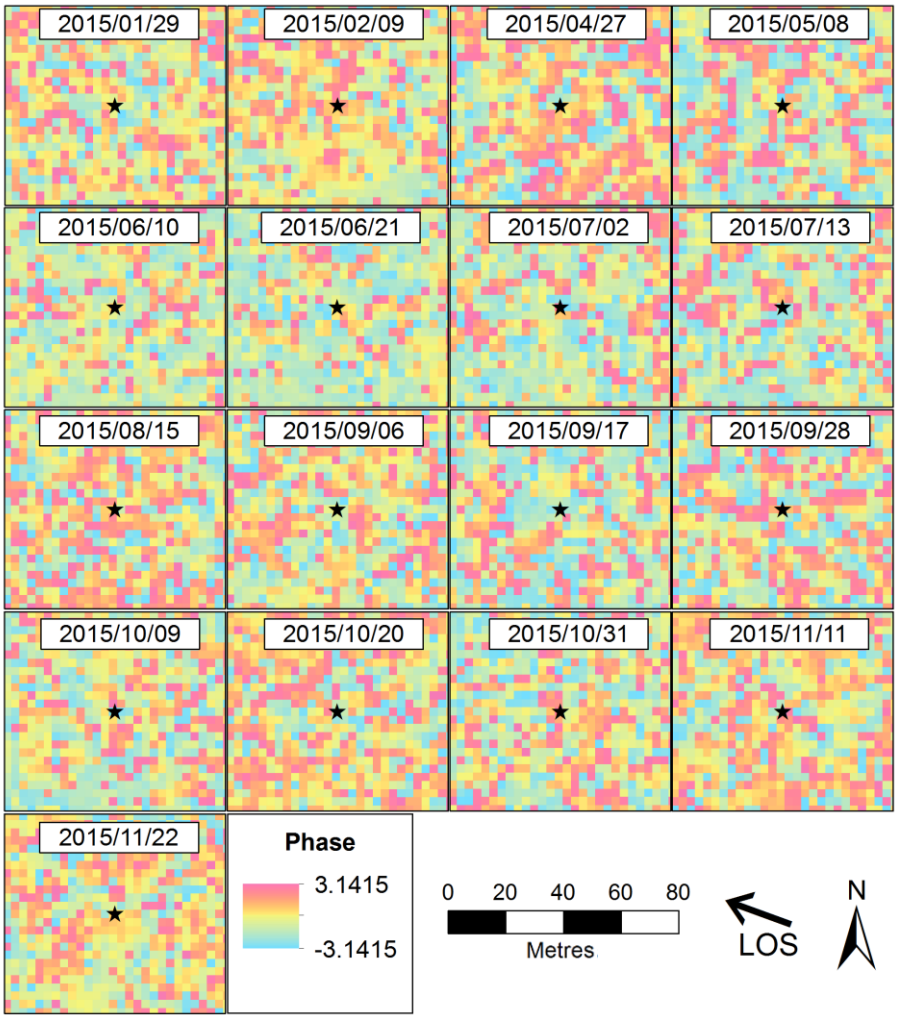

Figure 4.7 Interferograms for the area round event A3 with the approximate location reported as the black star. Only the master date for each image pair is provided, the slave date of each image corresponds to the master date of the following image. The final slave date for the interferogram with the 2015/11/22 master is 2015/12/03.

4.2.4 Event A4

Sinkhole inventory item A4 was a subsidence event that occurred during 2015 although the exact date of the event is not available. The high-resolution aerial photograph (Figure 4.8) shows that the event took place in the driveway of a residential building and that the area lacks significant vegetation. The time series of interferograms for the area of interest is provided in Figure 4.9. All available interferograms are shown due to the unknown exact date of the event. The results suggest that no precursory deformation was observed. The lack of vegetation that could have obstructed the line of sight suggests that temporal decorrelation by vegetation is not the cause of the non-detection of deformation. However, since the date of the event is not known, it is possible that the deformation took place before SAR data acquisition started. As in event A3, due to the lack of further information, DInSAR detection challenges relating to spatial extent and magnitude cannot be excluded.

Figure 4.8 Aerial imagery indicating the location of sinkhole event A4. The SAR line of sight (LOS) direction is also provided.

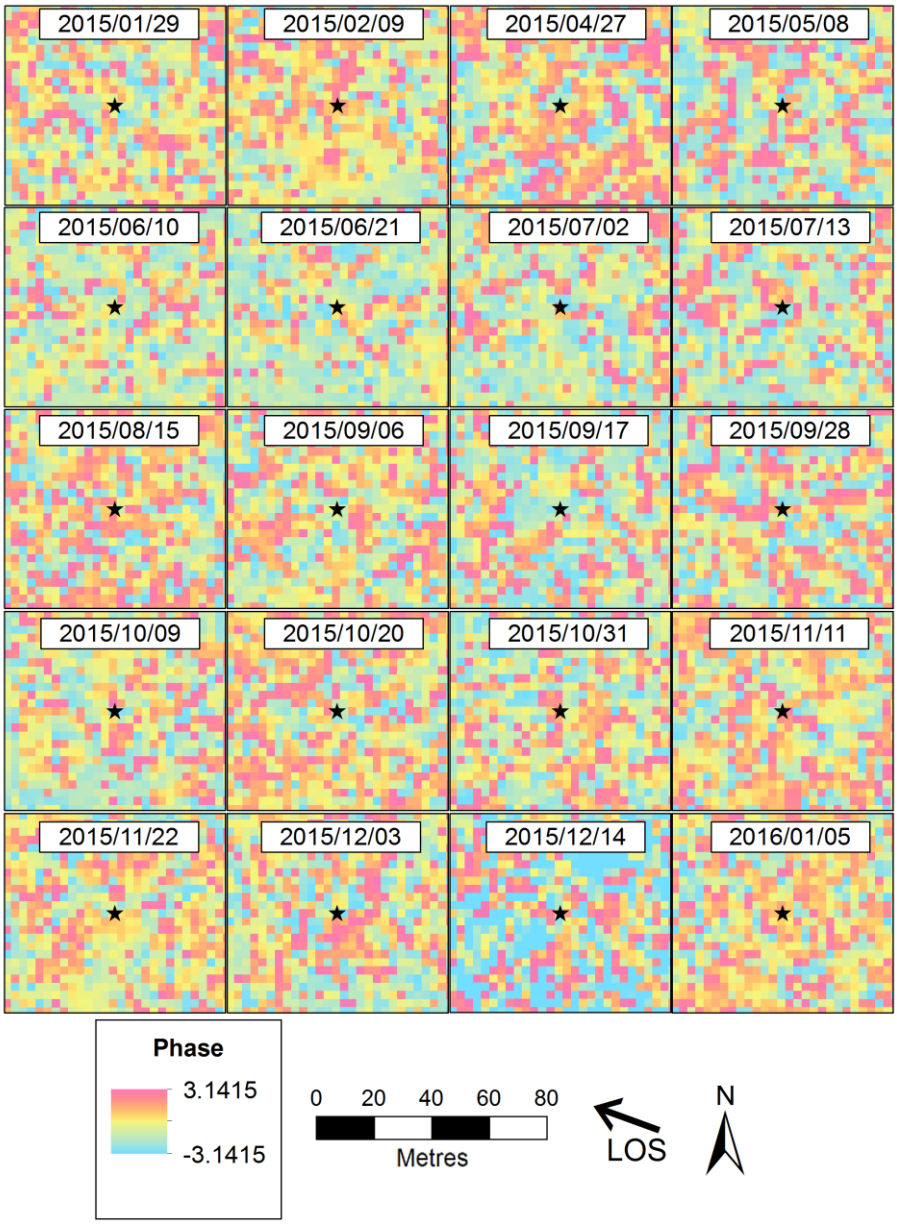

Figure 4.9 Interferograms for the area round event A4 with the approximate location reported as the black star. Only the master date for each image pair is provided, the slave date of each image corresponds to the master date of the following image. The final slave date for the interferogram with the 2016/01/05 master is 2016/01/27.

4.2.5 Event A5

Event A5 in the inventory occurred on 3 January 2016. The event was publicised in the local media (Kruger 2015). The sinkhole, measuring 20 m along the major axis, 13 m along the minor axis and 9 m deep, took place next to a road and very close to a telecommunications tower. The sinkhole resulted in damage to the road surface as well as the surrounding the telecommunications infrastructure (see Figure 4.10 A). The high-resolution aerial photograph indicating the location and approximate spatial extent of the sinkhole is also provided in Figure 4.10 B. This sinkhole event

was well documented, occurring nearly a year after the start of data acquisition, and had the largest spatial extent of all the recorded events leading to a high probability of precursor detection.

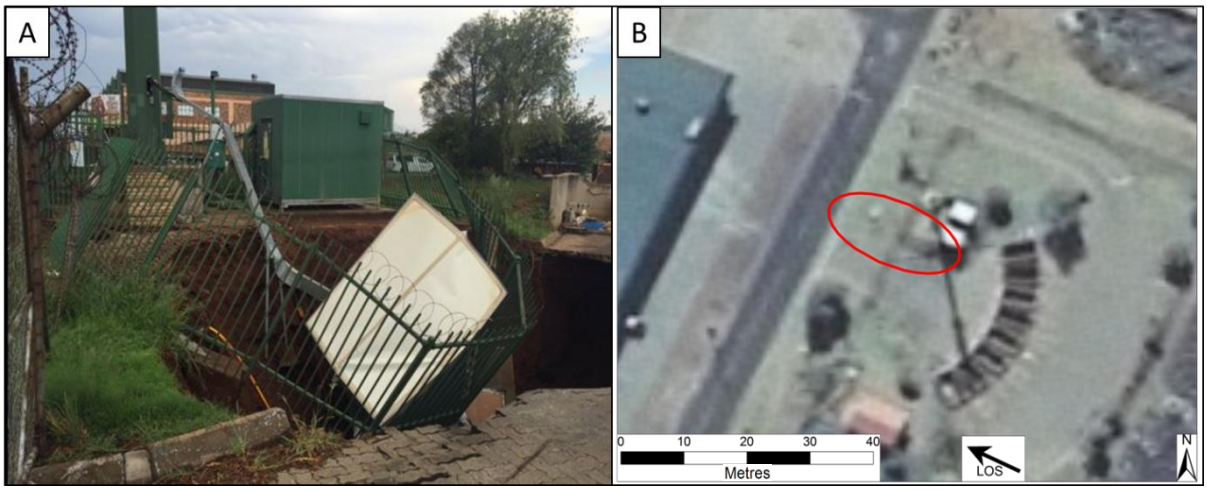

Photo: Yusuf Abramjee

Figure 4.10 (A) Field photograph of event A5 showing the sinkhole and resulting damages to the cell phone tower infrastructure. (B) An aerial image of the area where the sinkhole occurred with an approximate outline of the sinkhole (event A5) based on field observations. The SAR line of sight (LOS) direction is also provided.

The full-time series of interferograms for the location is provided in Figure 4.11. Despite the lack of vegetation that can cause decorrelation of the signal as well as ample data to cover the date of sinkhole formation, no deformation signals were observed prior to sinkhole development. It is expected that precursors to this sinkhole event, if present, would have been detectable.

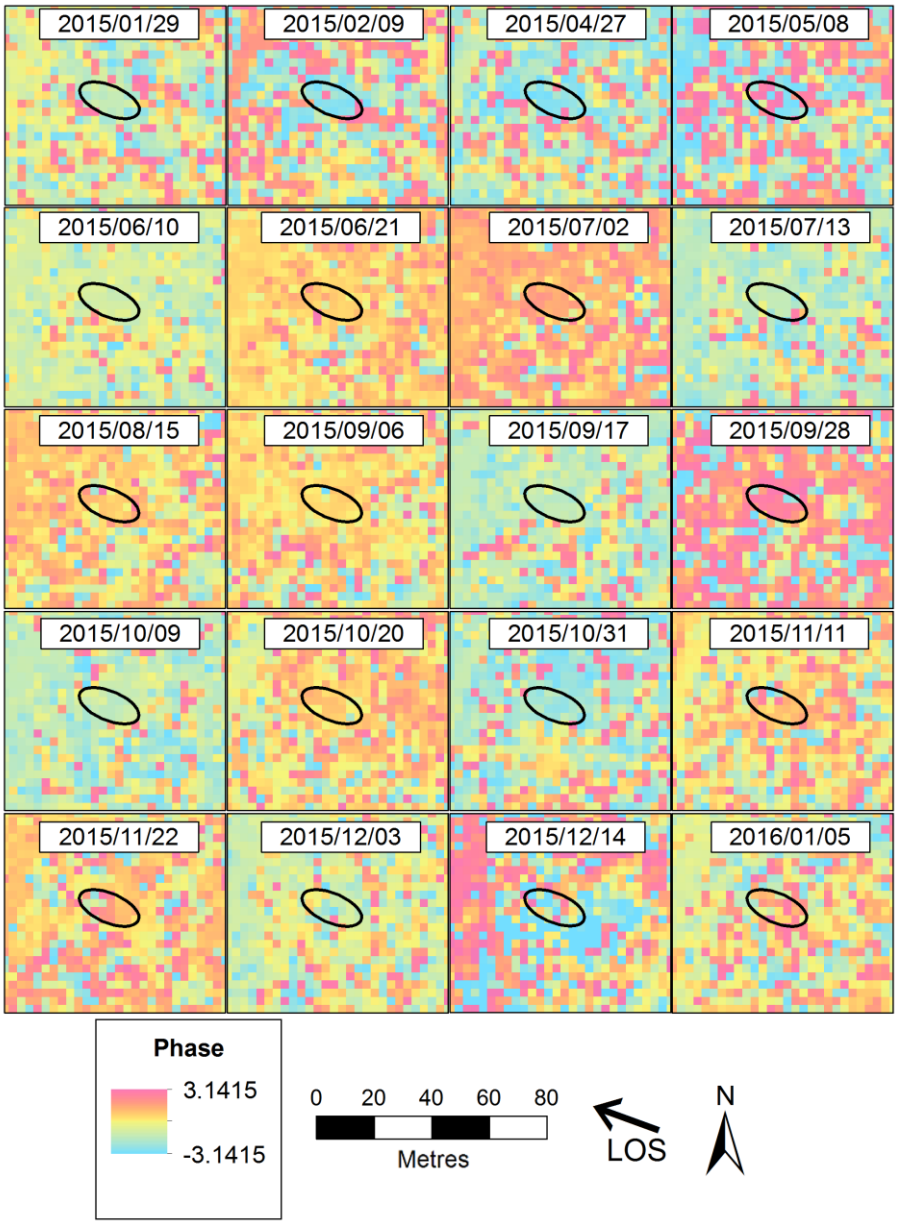

Figure 4.11 Interferogram time series over the entire study period from the 29th January 2015 to the 27th January 2016. The approximate location and extent of Event A5 are shown as a black oval. Only the master date for each image pair is provided, the slave date of each image corresponds to the master date of the following image. The final slave date for the interferogram with the 2016/01/05 master is 2016/01/27.

The area where the sinkhole occurred exhibited high coherence over the observation period (Figure 4.12). A reliable phase return and deformation measurement could be expected. However, the lack of detection, under conditions of high coherence, could further imply that deformation did not actually precede sinkhole formation in this case. This observation, however, depends on the non-detection not being a result of spatial and temporal challenges discussed earlier. An interesting further observation relating to coherence is the expected drop of coherence during and after the sinkhole event, visible on the last two images of Figure 4.12, likely due to the major change of the surface due to the sinkhole.

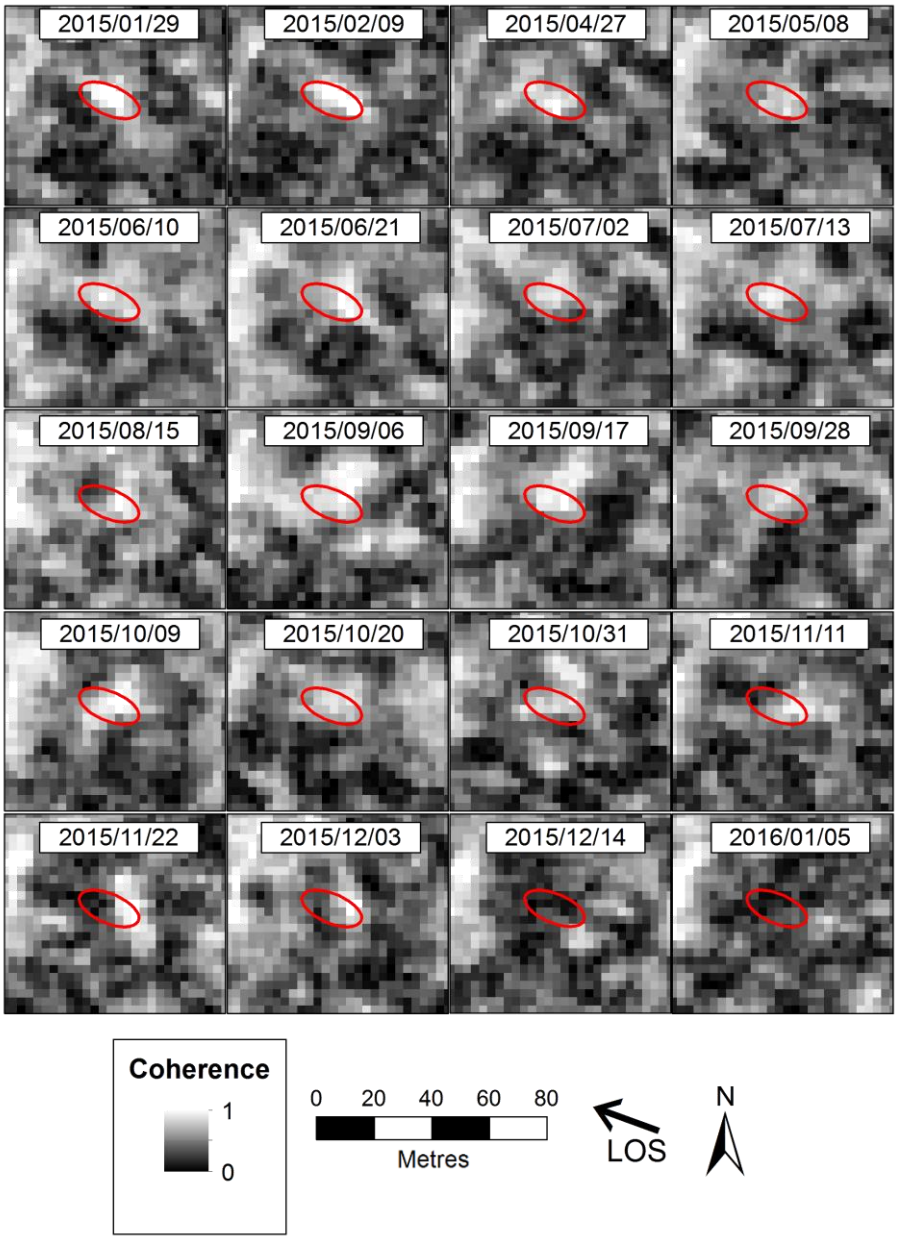

Figure 4.12 A time series of all the coherence images over the approximate location of event A5 showing the loss of coherence associated with the sinkhole can be seen on the final two images. Only the master date for each image pair is provided, the slave date of each image corresponds to the master date of the following image. The final slave date for the interferogram with the 2016/01/05 master is 2016/01/27.

The nature of precursory deformation is not well understood, particularly in the study area, and it is possible that small scale movement before sinkhole development does not always occur (see Sections 1.5 for a discussion of this based on the study area, Section 2.1.2 for the current geological understanding and section 2.2.5 for DInSAR based global results). In the case of event A5, several scenarios could have resulted in an inability to detect precursory deformation. Firstly, precursory deformation may not have occurred at all and the only deformation would have been due to the actual sinkhole collapse. This could be caused by the built-up nature of the area providing a surface resistant to deformation until catastrophic collapse. No precursors would have been recordable, irrespective of the data processing or deformation monitoring technology used. In

the second scenario, precursory deformation could have taken place prior to the SAR data acquisition period. In this scenario, a longer period of data acquisitions may have enabled the detection of surface movements. In the third scenario, precursory deformation could have taken place within a period of fewer than 20 days before sinkhole collapse. The interferogram spanning the sinkhole date (2016/01/03) used the 2015/12/14 and 2016/01/05 acquisitions dates as master and slave images respectively. Consequently, the sinkhole occurred 20 days after the master image acquisition. If precursory deformation took place in this 20-day window, it would not have been observable. If the temporal baseline of 22 days could be reduced to 11 days that would have reduced this period of uncertainty from 20 days to 9 days.

4.2.6 Event A6

Sinkhole inventory item A6 occurred in January 2016 next to a road in a residential neighbourhood. The high-resolution aerial photograph, provided in Figure 4.13 A, indicates the approximate location of the sinkhole event. The sinkhole, also seen in Figure 4.13 B, had recorded dimensions of 6 m along the major axis and 3 metres along the minor axis and a depth of 2 m. A leaking water pipe was believed to be the triggering mechanism. The time-series of interferograms for the area of interest is provided in Figure 4.14. No deformation-related fringe patterns can be observed on the interferogram. However, the recorded size of the event suggests that the deformation is smaller than the minimum detectable feature of approximately 9 m x 9 m that can be achieved on 3 m resolution TerraSAR-X data (see Section 2.3.2). The SAR acquisition temporal resolution may also have been a challenge as only one interferogram covers the period from 2016/01/05 to 2016/01/27 and precursory deformation could have taken place within the 22-day observation period.

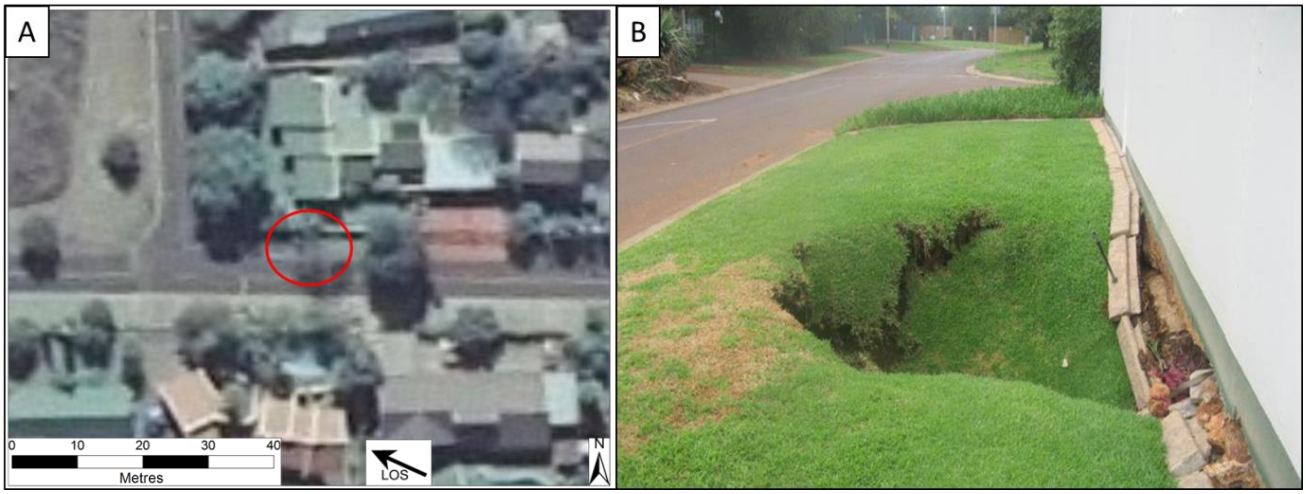

Photo: OUTsurance

Figure 4.13 (A) Aerial imagery indicating the location of sinkhole event A6 as well as a field photograph of the sinkhole (B).

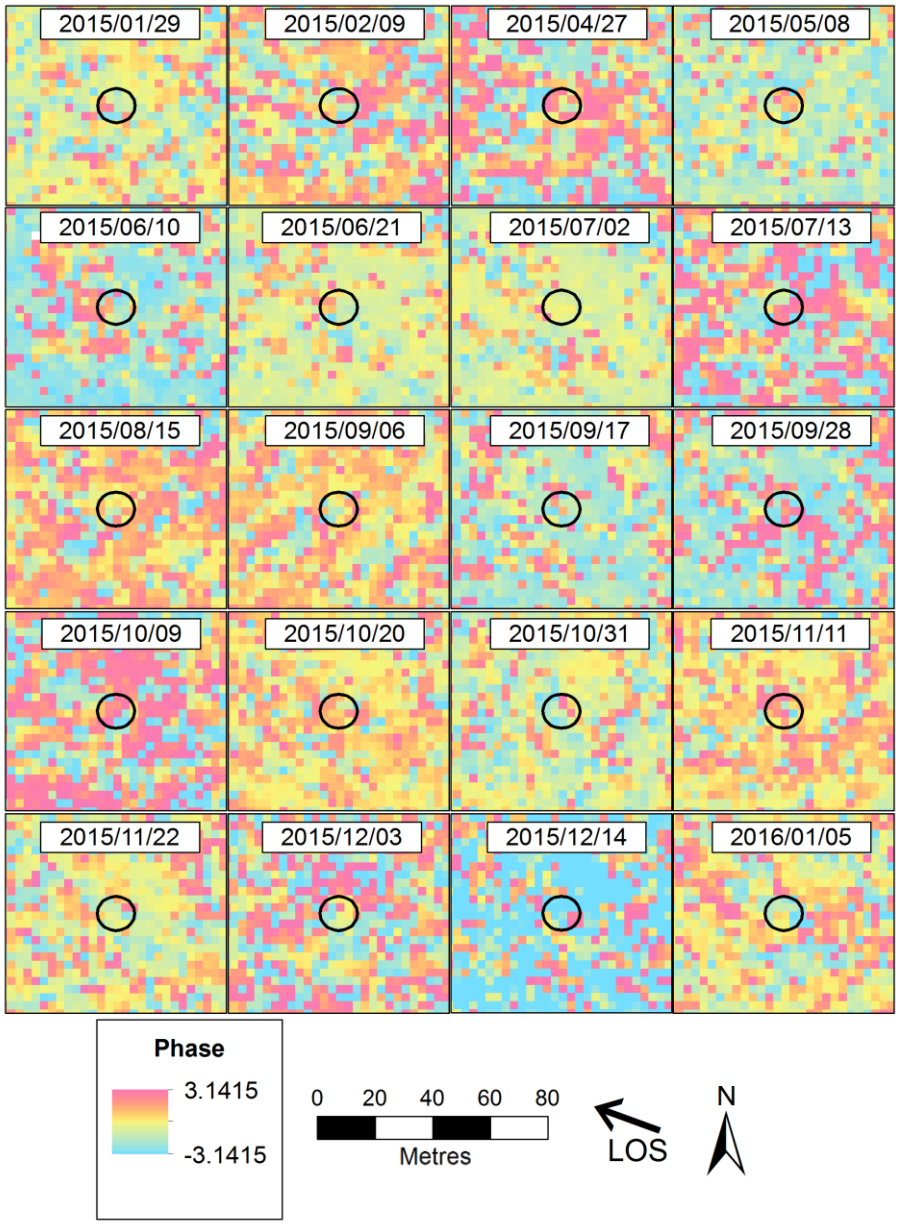

Figure 4.14 Interferograms for the area round event A6 with the sinkhole and its approximate extent indicated with a black circle. Only the master date for each image pair is provided, the slave date of each image corresponds to the master date of the following image. The final slave date for the interferogram with the 2016/01/05 master is 2016/01/27.

4.2.7 Event A7

Sinkhole inventory item A7 was regarded as a sinkhole and subsidence event caused by a leaking sewer pipe and formed on 29 January 2016. The exact position of the sinkhole remains uncertain since it has not been verified. Furthermore, the size of the feature was not recorded. It nevertheless remained an opportunity to test DInSAR's ability to detect deformation. The high-resolution aerial photograph of and approximate sinkhole location is provided in Figure 4.15. The area is located in a residential neighbourhood with relatively sparse vegetation. The time series of differential interferograms for the area of interest is provided in Figure 4.16. No deformation-related

fringe patterns were observed for the event. The event occurred two days after the final data acquisition and it is, therefore, possible that precursory deformation took place in the two days leading up to the sinkhole event. On the other hand, if precursory deformation occurred earlier than two days before the event, the data set would have been ideal since the decorrelation caused by the actual sinkhole formation would not have been an issue. Although insufficient field observations are available to draw accurate conclusions, possible limitations include a small spatial extent or a deformation gradient exceeding the gradient limit of the sensor.

Figure 4.15 Aerial imagery indicating the location of sinkhole event A7. The SAR line of sight (LOS) direction is also provided.

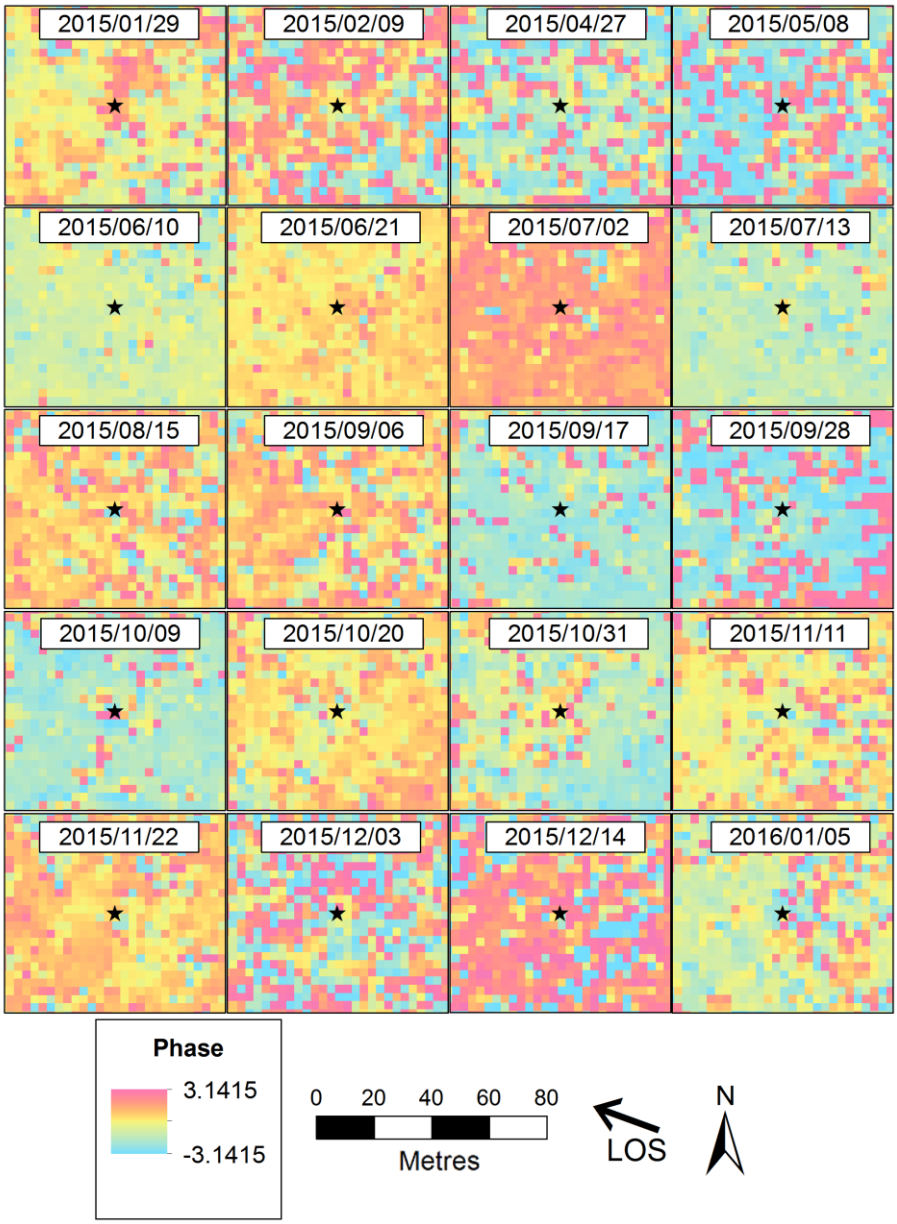

Figure 4.16 Interferograms for the area round Event A7 with the sinkhole indicated with a black star, the exact location is uncertain, however. Only the master date for each image pair is provided, the slave date of each image corresponds to the master date of the following image. The final slave date for the interferogram with the 2016/01/05 master is 2016/01/27.

4.3 DInSAR deformation observations

DInSAR techniques were unsuccessful in detecting precursory deformation prior to sinkhole development for the recorded sinkholes in the sinkhole inventory provided by the Council for Geoscience. Possible reasons for the non-detection of precursory deformation will be explored in Chapter 5. However, several deformation-related fringe patterns were observed in the area under investigation. One of these events, labelled B1 and described in Section 4.3.1, eventually led to sinkhole formation while deformation associated with two additional events remain unverified and

has not been associated with collapse by the time of publication. The details on these two events, labelled B2 and B3, are provided in Section 4.3.2 and Section 4.3.3.

4.3.1 Event B1

The DInSAR results revealed two deformation basins approximately 10 m from each other that occurred two months apart. These basins are shown in Figure 4.17. The first was observed between 21 June 2015 and 15 August 2015 (55 days) and was ~100 m in diameter. The second basin was detected between 20 October 2015 and 11 November 2015 and was ~ 40 m in diameter. Furthermore, on 17 December, one month after the last detection, a high-pressure pipe burst in between these two deformation basins. A high-resolution aerial photograph, indicating the location of the deformation features is provided in Figure 4.17. This section will present evidence and analyses of these two deformation basins in the form of interferograms, displacement maps, coherence maps and field photographs.

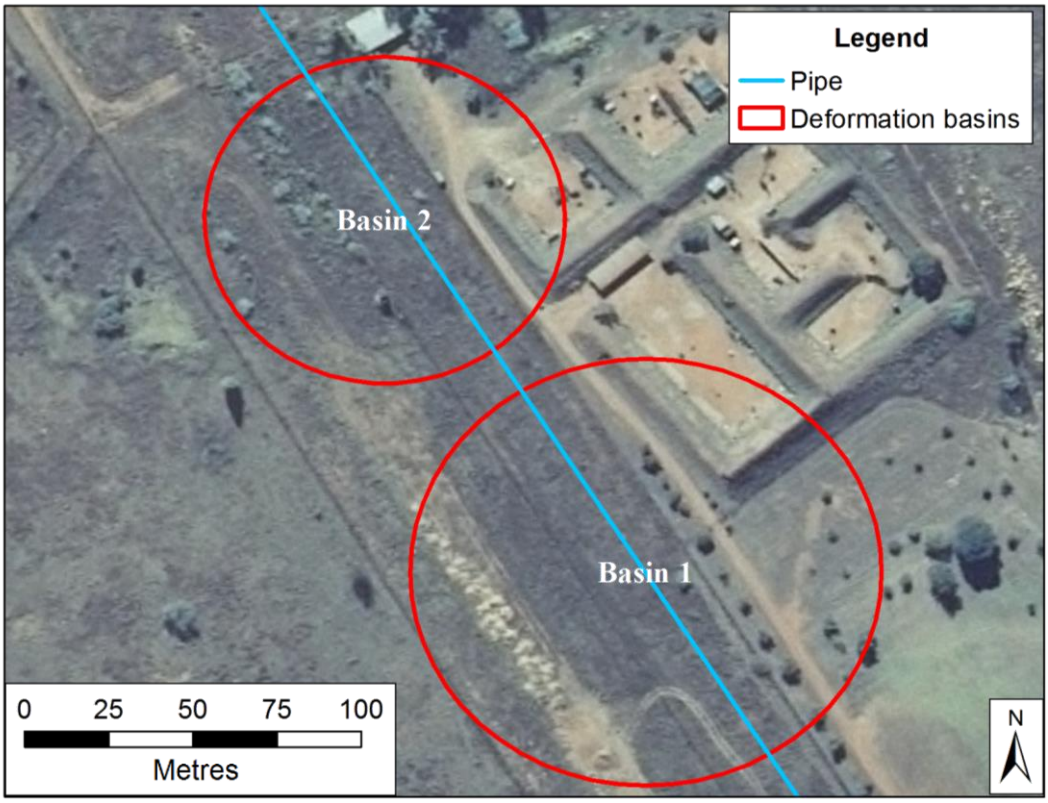

Figure 4.17 Aerial imagery indicating the approximate maximum extent and location of the deformation basins and pipe (blue line) discussed as event B1. Basin 1 represents the June to August detection while Basin 2 circle represents the October to November detection.

4.3.1.1 Basin 1

The time-series of differential interferograms for the area of interest is presented in Figure 4.18. The deformation fringes were observed on three interferograms starting on the 2015/06/21 – 2015/07/02 interferometric pair and remained visible on the 2015/07/02 – 2015/07/13 and

2015/07/13 – 2015/08/15 pairs (Figure 4.18). These fringes are not visible on interferograms before or after this period. To rule out residual phase the nature of the deformation measured and perpendicular baselines of the datasets were considered using a pair-wise logic (Massonnet & Feigl 1998). Residual atmospheric phase could first be ruled out due to the feature's small scale and persistence within the time series. Atmospheric phase fringes would not remain stable between four acquisitions as is seen in this series since the atmosphere changes randomly between acquisitions. Furthermore, atmospheric fringes are generally characterised by a larger spatial extent.

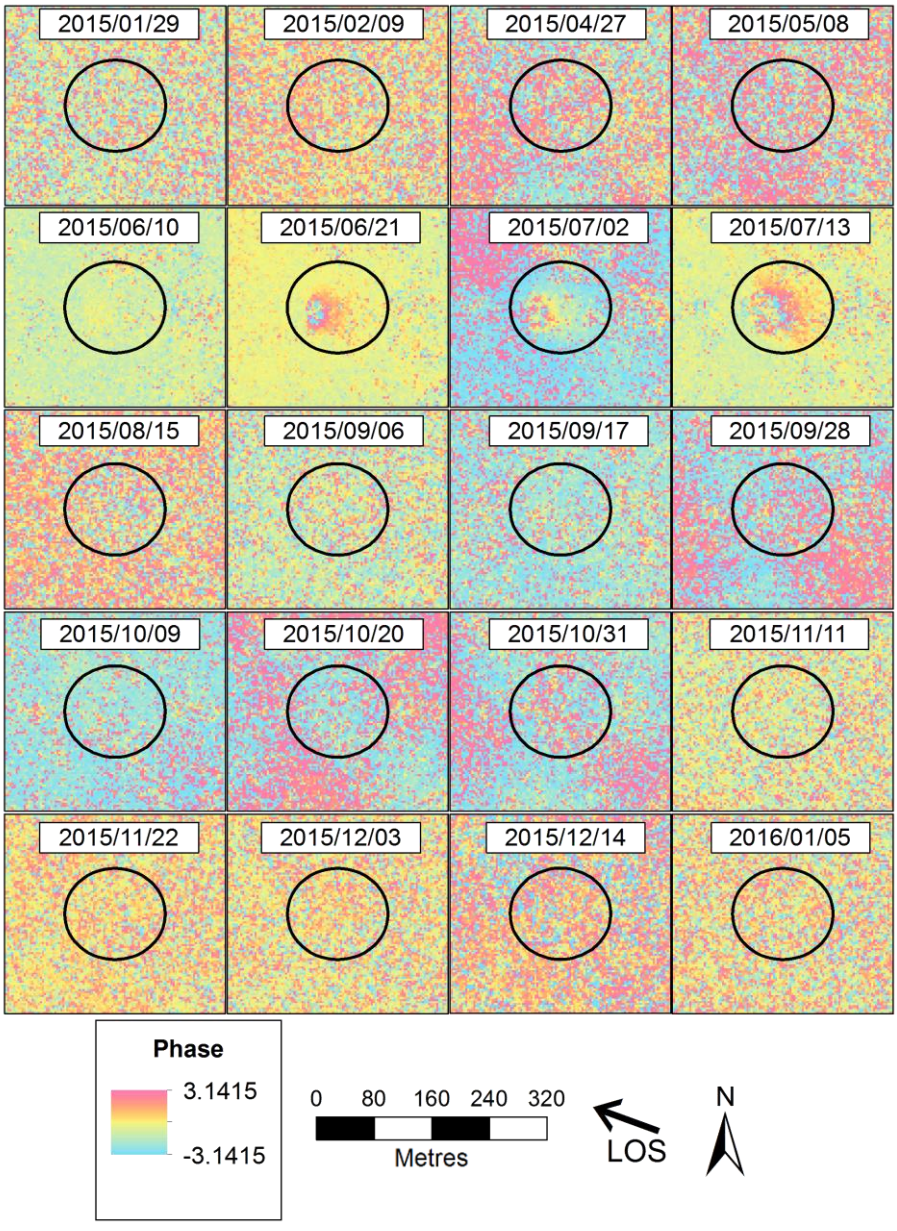

Figure 4.18 Interferograms for the area round event B1 with the subsidence and its approximate extent indicated with a black circle. Only the master date for each image pair is provided, the slave date of each image corresponds to the master date of the following image. The final slave date for the interferogram with the 2016/01/05 master is 2016/01/27. Deformation is observed between interferogram master dates: 2015/06/21 and 2015/07/13.

Residual topographic effects could also be ruled out since very low relief is associated with the area. In fact, there is less than 1 m change in elevation across the feature. Furthermore, the topographic sensitivity of the interferometric pairs used for the detections is very low due to their small perpendicular baselines. In fact, the perpendicular baselines of the three images where deformation was detected correspond to ambiguity heights of 453 m, 98 m and 393 m for the three pairs respectively. This means that an elevation change of hundred(s) of metres across a feature would be necessary before it would contribute a phase change corresponding to a single fringe on the interferogram. This case is therefore regarded as a detection of true ground deformation rather than atmospheric of topographic in nature.

A summary of the relevant measurements derived from the displacement maps is presented in Table 4.1. The maps are presented in Figure 4.19. The first subsidence observation between 2015/06/21 and 2015/07/02 revealed a basin of approximately 65 m x 60 m in extent with a maximum deformation of 22.4 mm observed. Between 2015/07/02 and 2015/07/13, the area that was still deforming decreased and was approximately 60 m x 50 m in extent with a maximum of 17.3 mm of deformation observed. Finally, the period between 2015/07/13 and 2015/08/15 was associated with an increase in the extent of the deformation basin to an area of approximately 75 m x 55 m with a maximum of 42.2 mm of subsidence observed. It should be noted that the temporal baseline of the final displacement maps (2015/06/21 and 2015/08/15 respectively) are longer (33 days) compared to the two initial pairs with day difference of 11 days, thereby explaining the perceived increase in extent and magnitude of the deformation. The observed deformation basin reached a total extent of 80 m x 75 m over a period of roughly 2 months with a maximum vertical subsidence of 66.7 mm observed.

Table 4.1 A summary of the physical dimensions of the first basin of Event B1 detected between June and August 2015 along with appropriate interferometric properties.

Interferogram date	Subsidence (mm)	Major axis Diameter (m)	Minor axis Diameter (m)	Temporal baseline (days)	Perpendicular baseline (m)
2015/06/21 to 2015/07/02	Mean: 8.4 Max: 22.4	60	55	11	10.3
2015/07/02 to 2015/07/13	Mean: 6.3 Max: 17.3	60	50	11	69.1
2015/07/13 to 2015/08/15	Mean: 20.3 Max: 42.2	70	75	33	14.4
Total displacement stack	Mean: 10.7 Max: 66.7	80	75	55	n/a

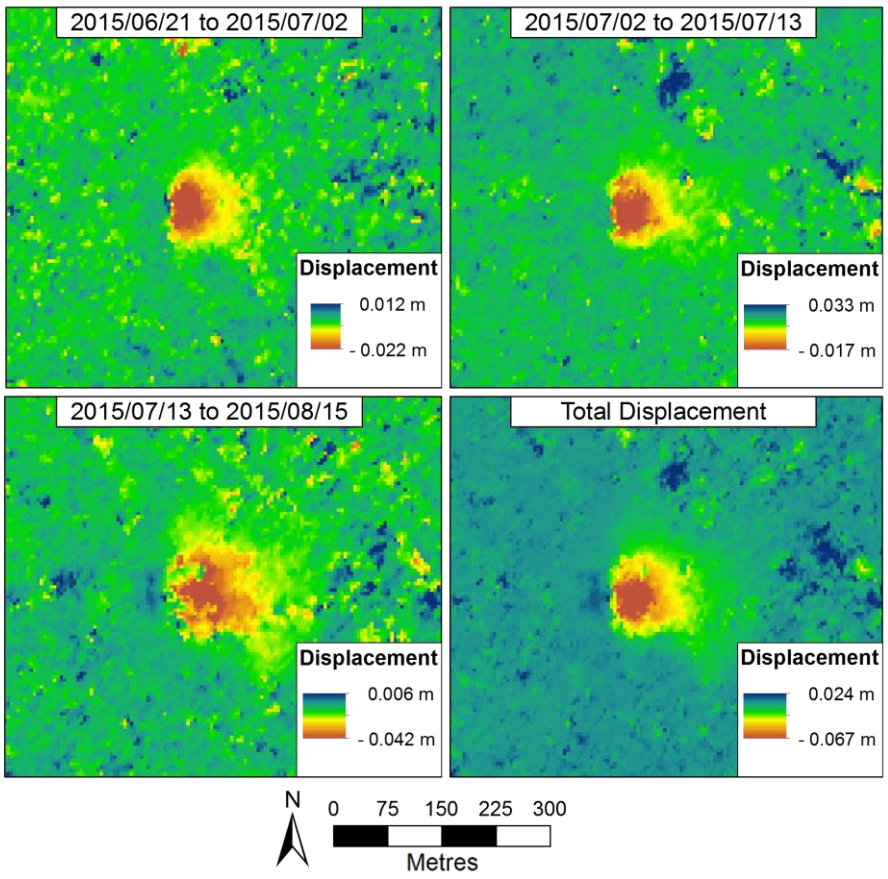

Figure 4.19 Displacement maps of the deformation event B1 derived from three interferograms as well as the sum of the three maps showing the total deformation detected over the period.

The deformation basin was an oval shape approximately 80 metres in diameter over the time series as is seen in Figure 4.19. The western periphery of the basin has a sharper boundary than the other sides and appears to be constrained, possibly by some surface feature or subsurface geology. The three-dimensional cross section of the sum of deformation across the entire period reveals that the deformation basin is asymmetrical between its eastern and western periphery (see Figure 4.20). The deformation gradient on the western side is steeper than the eastern side.

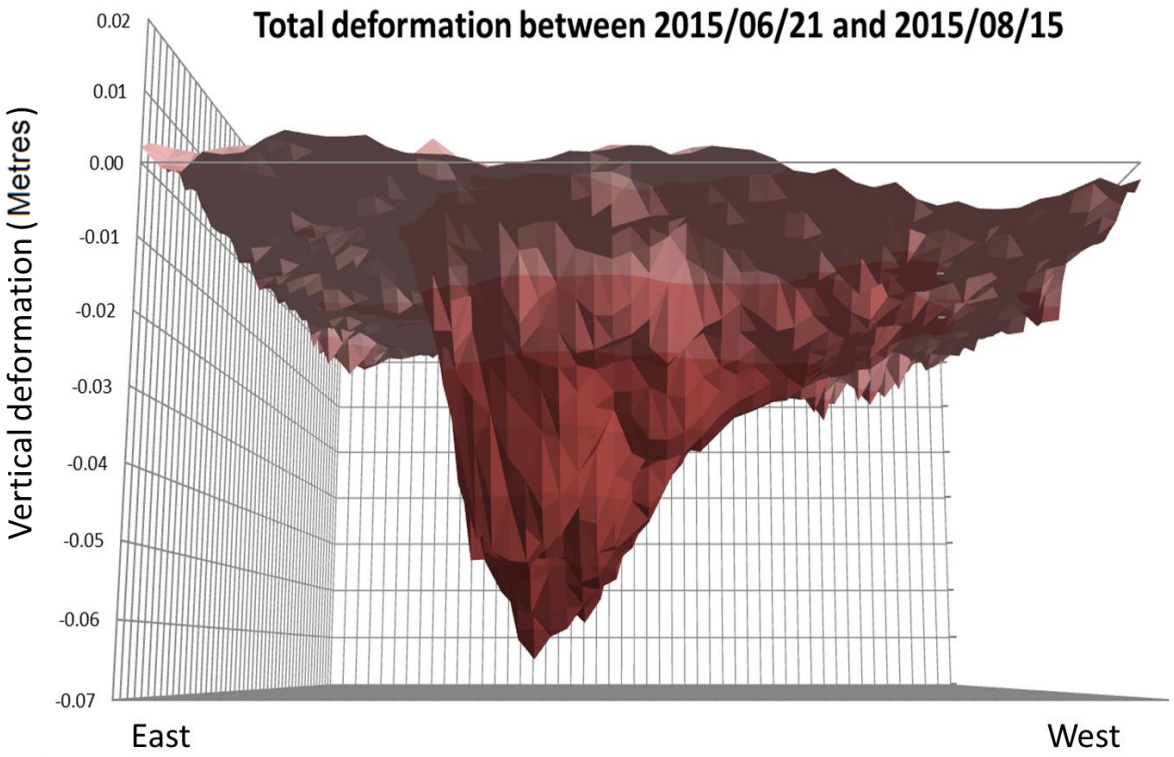

Figure 4.20 A three-dimensional representation of the total deformation detected over event B1. Note the exaggerated vertical deformation axis. The deformation basin is distinctly asymmetrical in gradient between the east and west.

4.3.1.2 Basin 2

Further investigation of the interferogram stack for the area revealed the possibility of a small-scale deformation feature present on the 2015/10/20 – 2015/10/31 interferogram. This feature is approximately 40 m in diameter and can be seen in Figure 4.21 A on the southeast part of circle 1. Additional subsidence is observed between on the second interferogram spanning 2015/10/31 to 2015/11/11. These two deformation measurements were not considered as high confidence measurements due to the similarity of this fringe patterns to common interferogram noise patterns. However, their proximity to the known deformation in Basin 1 (Section 4.3.1.1) and the subsequent sinkhole event indicated that the detections could be related.

To increase the likelihood detecting any small-scale deformation of this area, a 22-day interferogram was processed to cover the period between 2015/10/20 and 2015/11/11. The 22-day interferogram is presented in Figure 4.21 E & F. The deformation basin can be identified with higher certainty than on the shorter temporal baseline results. An increased temporal baseline could result in an increase of deformation observed in that period. The resulting stronger fringe pattern is more suitable for deformation detection. Furthermore, it was found that the perpendicular baseline of this 22-day interferogram was only 24 m, making less sensitive to topographical phase residue. It should be noted that the longer temporal baseline did not result in significantly more phase speckle as could be expected due to a loss of coherence.

The basin was found to be irregular in shape and larger in extent (40 m in diameter) than the basin revealed on the first 11-day interferogram in Figure 4.21 A (2015/10/20 – 2015/11/11). The maximum vertical deformation of the basin was 2.2 cm. This detection would likely have gone unnoticed were it not for the larger deformation basin close by. The close proximity of this deformation basin to the ultimate sinkhole event (discussed in the following section) provides strong evidence that the fringe pattern observed was not due to erroneous phase contributions or random noise.

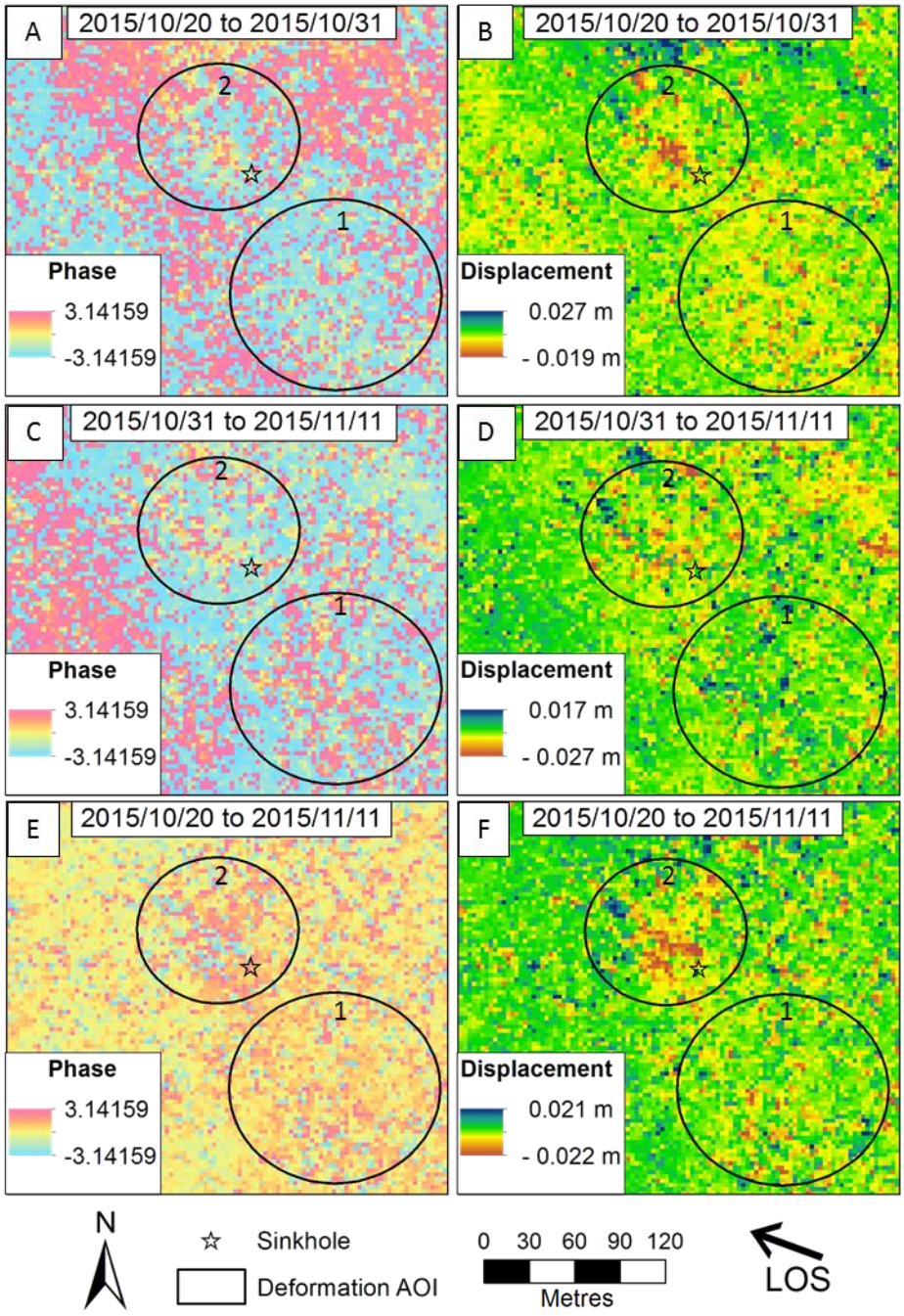

Figure 4.21 Interferograms (left) and vertical displacement maps (right) of the second deformation detection period of event B1. A - D shows subsequent 11-day interferograms while E - F shows the encompassing 22-day interferogram. Circle 2 encompasses the second deformation event detected presented in this section while the circle 1 shows the extent of the earlier deformation basin with no deformation apparent.

4.3.1.3 Further investigation and sinkhole event

No further deformation was detected on the data preceding and following the two deformation detections. This observation does not necessarily constrain deformation to these periods since deformation could have remained undetected due to various reasons related to DInSAR limitations and the environmental conditions. A loss of coherence could lead to the inability to detect subsidence events.

Figure 4.22 shows the time series of the coherence. The coherence does not remain stable over time. The coherence was low during the start and end of acquisitions since this was in January during the rainfall season. It steadily increased and remained high over the dry season with two notable exceptions. Coherence was sharply reduced after the 2015/08/15 and 2015/11/11 acquisitions. This coincides with the end dates of the two detected deformation basins. Deformation of the first basin was detected from 2015/06/21 and was observed until 2015/08/15 while the second basin was detected from 2015/10/20 to 2015/11/11. It is possible that deformation continued past the last detection but remained undetected due to a loss of correlation. Nevertheless, the starting date can be constrained more confidently due to more favourable coherence conditions. A further discussion of the factors that influenced coherence in this study, rainfall, vegetation growth, temporal baseline and the perpendicular baseline is provided in Section 5.1.5.

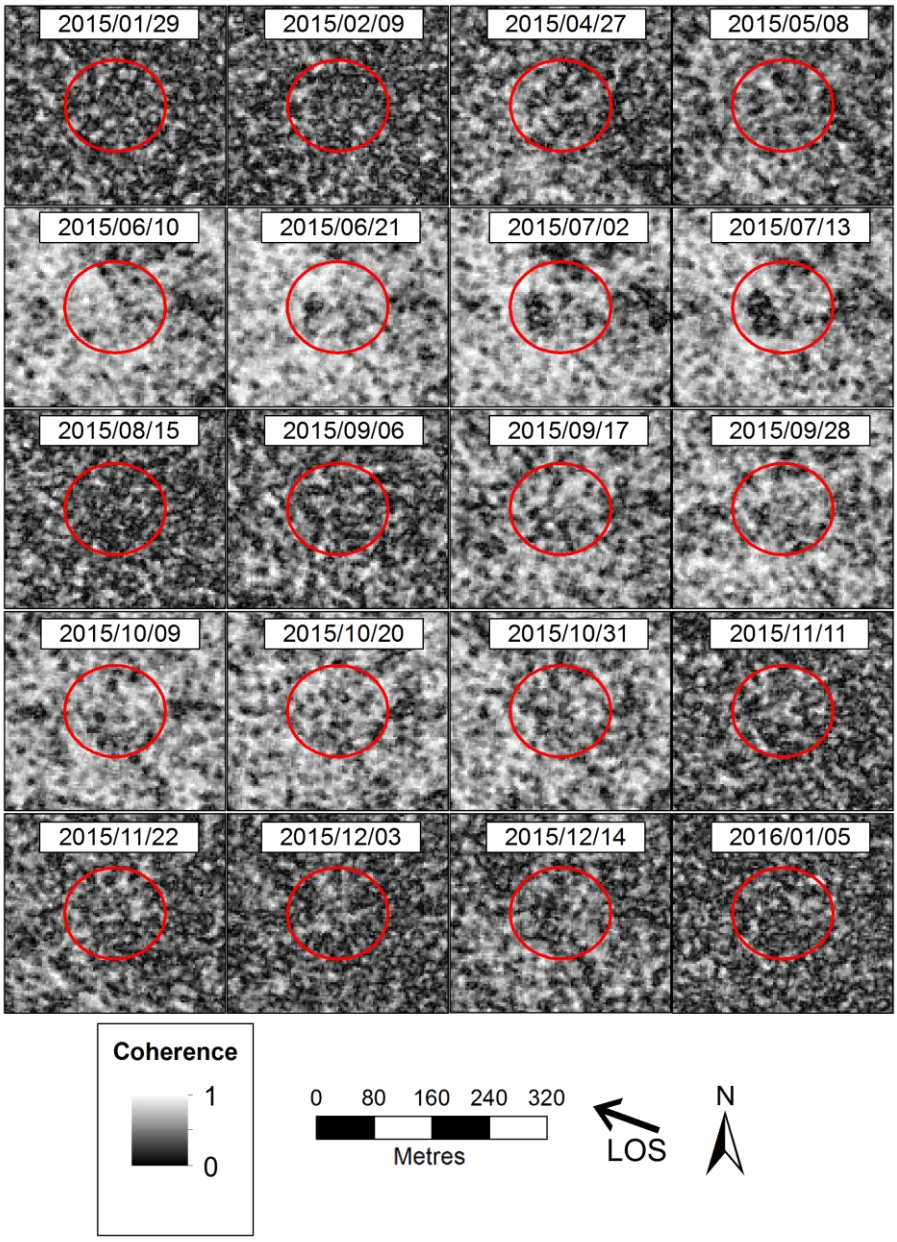

Figure 4.22 A time series of all the coherence images showing the first basin of event B1 (red circle). Only the master date for each image pair is provided, the slave date of each image corresponds to the master date of the following image. The final slave date for the interferogram with the 2016/01/05 master is 2016/01/27. A coherence of one indicates total phase stability of the pixel over all the interferometric pairs over the study period while zero indicates a total loss of phase stability.

The area where deformation was detected was visited on 17 December 2015 to gather field evidence that could be used to verify that deformation has taken place. Field observations confirmed that the deformation occurred on a private property on a corridor established for municipal water pipelines. The area has a gentle slope and sparse dry grassland vegetation cover with a frequently used jeep track running through it. Two high-pressure pipelines run less than one metre underground connecting two water reservoirs (blue lines in Figure 4.17). The property owners confirmed that one of the high-pressure water pipelines had been leaking since January

2015 in an area upslope of where the deformation occurred. This led to a constant stream of water flowing downhill. This stream flows through the middle of the detected deformation feature and had created a temporary wetland along its path (see photograph D in Figure 4.23). Field observations also revealed the presence of tension cracks (see photograph A and B in Figure 4.23), a common secondary effect of surface subsidence occurring on the edges of deformation basins. The tension cracks were approximately 20m in length, at least 20 cm deep and up to 5 cm wide. The tension cracks were found along the eastern periphery of the basin, corresponding to the area where the steepest deformation gradient was detected.

On the morning of the 17th of December 2015, a water-filled hole in the ground of 0.5 by 1.0 m in diameter was observed in the field. The hole intersected a high-pressure pipeline running through the area and was probably caused by a leak in the pipeline. The location of the hole was in close proximity to the second deformation basin that was detected between October and November 2015 and was approximately 20 m from of the first deformation feature detected between June and August. Hours later, the pipeline burst which resulted in a jet of water up to 10 m high (the jet of water is visible in the background of Figure 4.23 B). This event is regarded as being related to both DInSAR-detected deformation basins since it occurred between the two basins, and very close to the second detection. The first detection started six months earlier and deformation was ongoing until at least four months earlier. The second event was detected two months before the pipe burst and ended one month before. Since the surface deformation was observed during a period associated with very little rainfall (a more detailed discussion of the rainfall associated with this event is provided in Section 5.1.5), it is postulated that the water supply pipeline was leaking for a period of several months prior to the deformation observations. The leaking servitude resulted in the formation of a cavity in the underlying dolomite. The surface subsidence observed using DInSAR observations was likely the result of the subsurface erosion of the roof strata into the cavity leading to localised surface instabilities. The eventual rupturing of the water supply pipeline was likely due to the increase of stress in the pipeline due to the ground deformation on both sides of the pipeline.

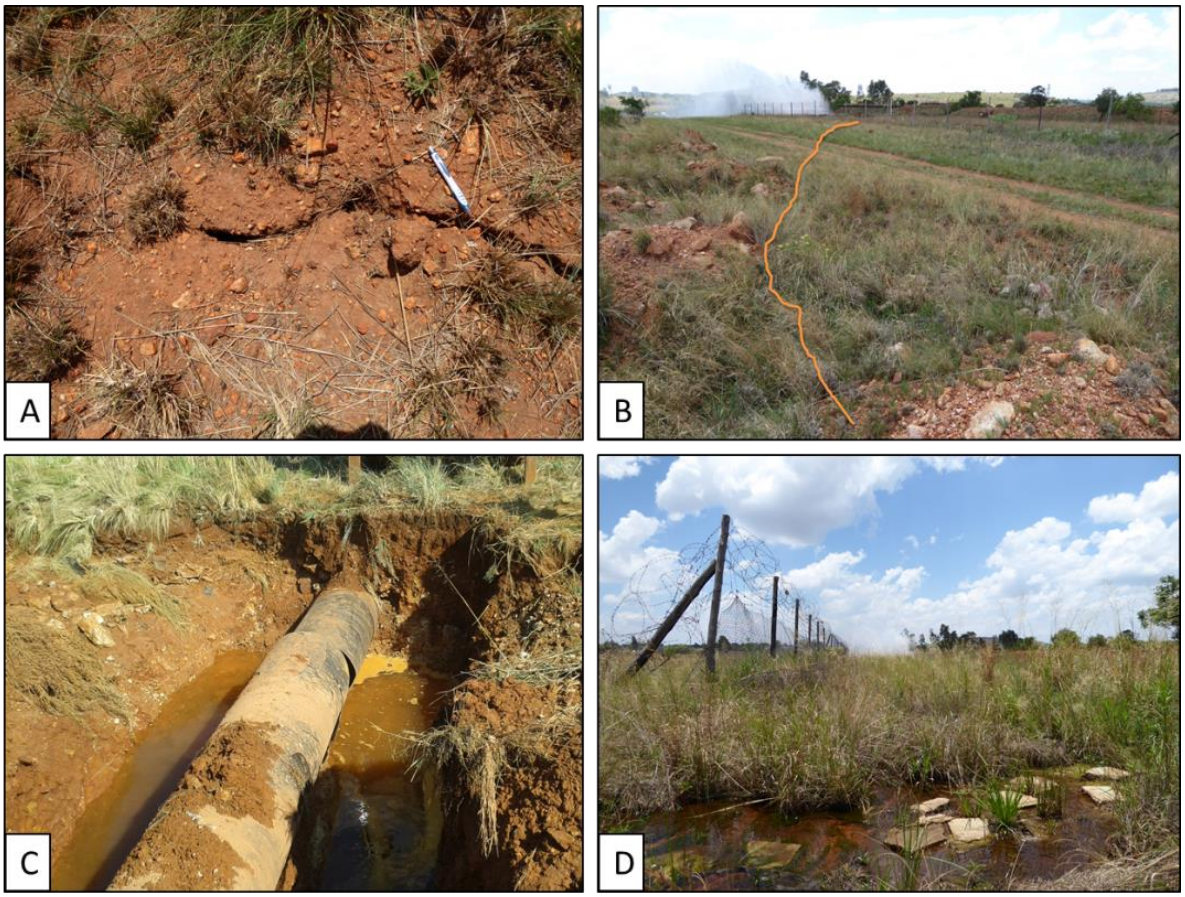

Photo: Author

Figure 4.23 Field observations of Event B1. Image A shows tension cracks observed on the north-eastern periphery of the deformation basin. Image B shows the length of the tension crack. At the back of the image, the water spraying out of the burst pipe (shown in image C) can be seen. Image D shows the wetland that formed over approximately a year, providing evidence that the pipes have been leaking for an extended time.

4.3.2 Event B2

A deformation feature was observed in the area shown in Figure 4.24, over two separate periods with no deformation detected during the 11 days separating these periods. The land cover of the area is residential with houses, walls, swimming pools and large trees. The interferogram time-series showing the detections is presented in Figure 4.25. The detected deformation was initially positive, indicating uplift (2015/06/21 to 2015/07/02), and then negative, indicating subsidence (2015/07/13 to 2015/08/15). No deformation was detected on the pair between these two pairs (2015/07/02 to 2015/07/13), yet a faint fringe outline can be seen on this pair.

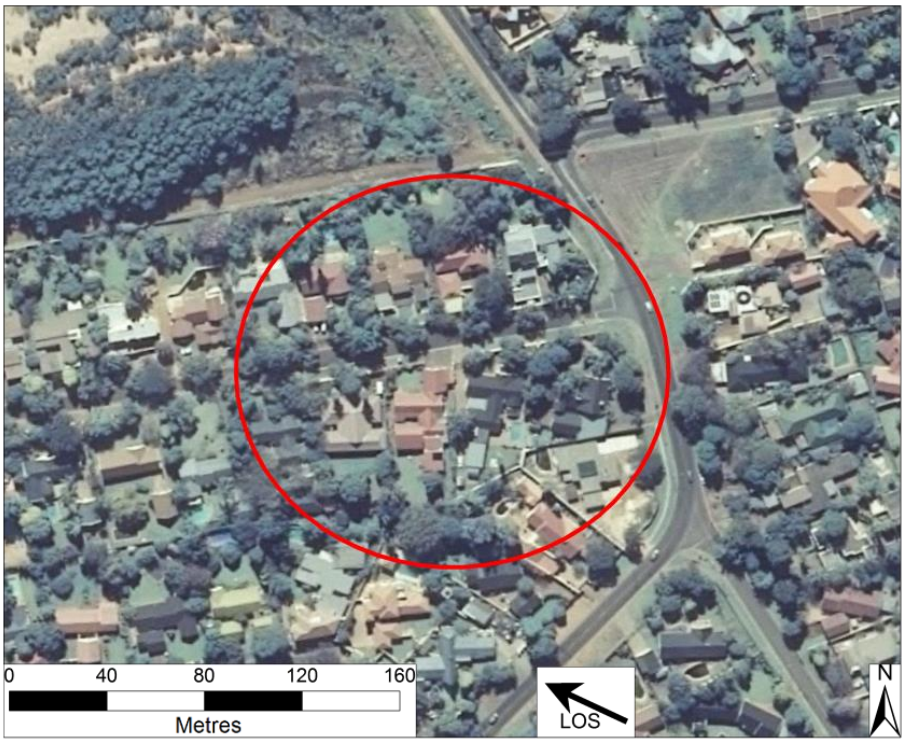

Figure 4.24 High-resolution aerial image indicating the location and approximate extent of deformation event B2. Note the complicated land cover found in residential areas due to open fields, roads, houses, swimming pools and large trees.

This feature presented uncommon deformation characteristics: a relatively large scale, a pause in deformation as well as the positive and negative uplift detected. Therefore, associated interferometric factors that could have influenced this particular event were analysed. The fringe pattern seen in Figure 4.25 is not due to residual topographical phase since the area has essentially no topographical variation with only a 1m change in elevation across the feature. Furthermore, the perpendicular baseline of the interferometric pairs was also very low (10.3 m and 14.4 m respectively) leading to a low sensitivity to topography. Atmospheric phase delay might also be responsible for such fringe patterns. As discussed in Section 4.1 the APS can be identified by its spatiotemporal signature. This signature is essentially a large fringe pattern that is identical in extent in all interferograms sharing acquisitions affected by the APS. However, the signature will result in a positive magnitude in one interferogram and an identical, yet negative, magnitude in the other. The deformation pattern was detected over three successive interferograms using four image acquisitions. The feature was most pronounced in the first and last interferograms, which do not share a common acquisition that could have led to the atmospheric residue. Furthermore, the deformation basin is seen in the first and last maps in Figure 4.26 have differing spatial extents. However, fringe contributions due to the APS cannot entirely be excluded for this event.

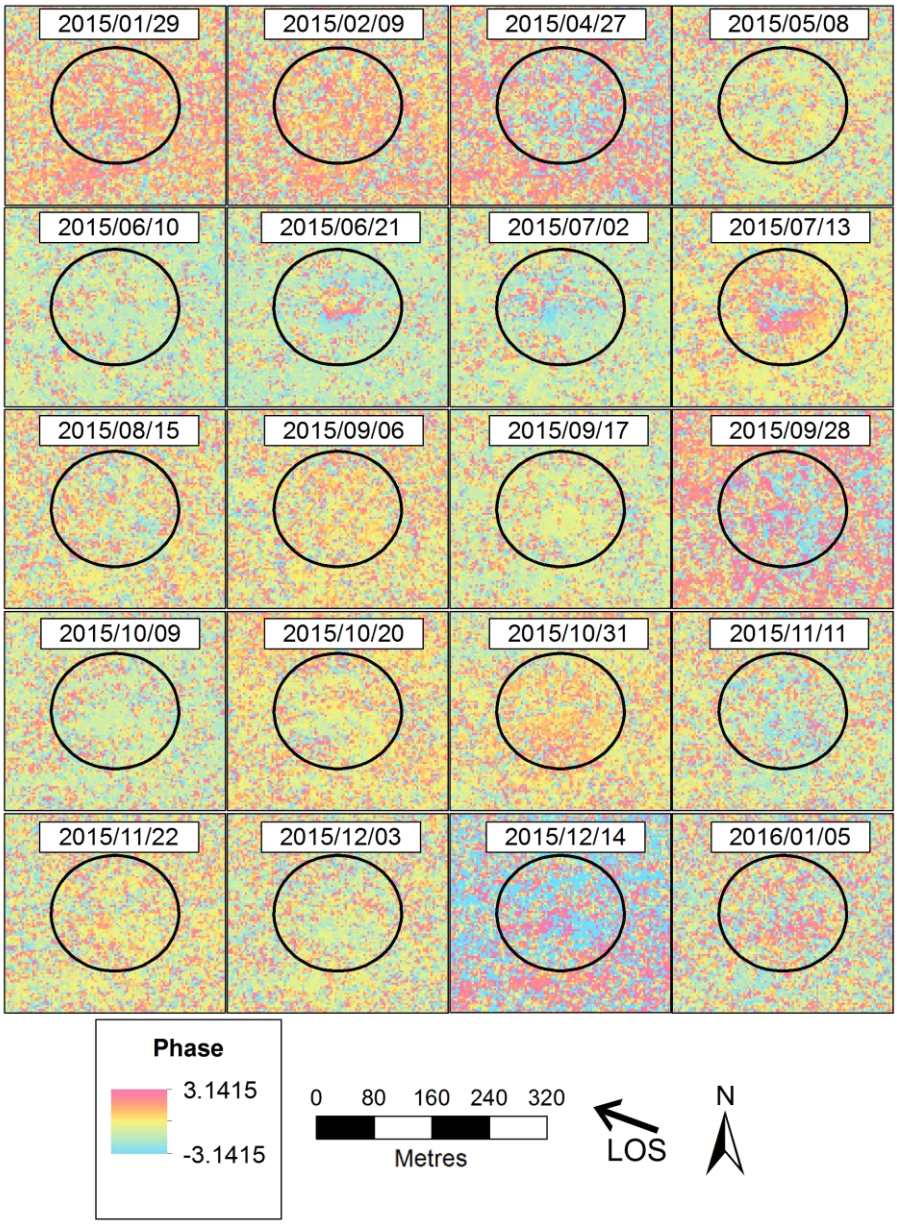

Figure 4.25 Interferograms for the area round event B2 with the subsidence and its approximate extent indicated with a black circle. Only the master date for each image pair is provided, the slave date of each image corresponds to the master date of the following image. The final slave date for the interferogram with the 2016/01/05 master is 2016/01/27. Deformation is observed between interferogram master dates: 2015/06/21 and 2015/07/13.

When analysing the vertical displacement maps generated from these interferograms (Figure 4.26) it was found that the initial uplift reached a maximum of 2.2 cm over the 11-day period between 2015/06/21 and 2015/07/02. The deforming area was approximately 50 m in diameter. No deformation was visible on the interferogram subsequent to the uplift yet faint uplift patterns remained (2015/07/02 to 2015/07/13). Following this, strong subsidence was detected on the final pair (2015/07/13 to 2015/08/15). Here, a maximum subsidence of 4.4 cm was observed occurring over the 33-day period. The subsidence basin was approximately 90 m in diameter. No deformation could be detected on the following interferograms after the deformation detection on

2015/08/15 to 2015/09/06. It has to be noted that this pair had a reduced coherence that may be masking deformation related signals. On the other hand, the interferometric pair (2015/06/10 to 2015/06/21) preceding the first deformation detection had a high coherence and deformation would likely be detected here making it possible to constrain the date of initial uplift to after 2015/06/21. At the time of publication, no further deformation was observed, by DInSAR measurements nor by in-situ observations. However, the deformation is associated with areas of known dolomite occurrence and the observed deformation could be an indication of potentially dangerous dolomite instability.

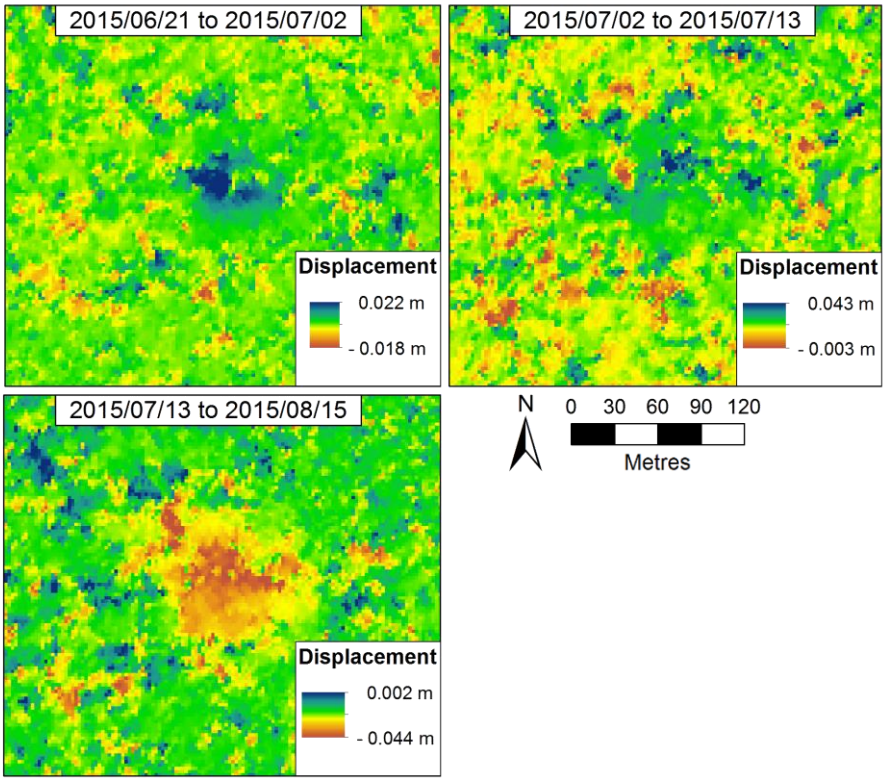

Figure 4.26 Vertical displacement maps of the area around Event B2, generated from the interferometric pairs where deformation was detected.

4.3.3 Event B3

An uplift feature was detected on an island between two roadways as is indicated by the aerial image in Figure 4.27. The deformation feature was detected over two interferograms, 2015/06/10 to 2015/06/21 and 2015/06/21 to 2015/07/02 (see the entire time series in Figure 4.28). Both interferograms span 11 days. As with previous detections, there is no significant topography found under the area of uplift that could lead to topographical fringe residues. The topographic sensitivity of the pairs is very low, 41 m and 10 m. Atmospheric residue could also be ruled out using the pair-wise logic approach (Massonnet & Feigl 1998).

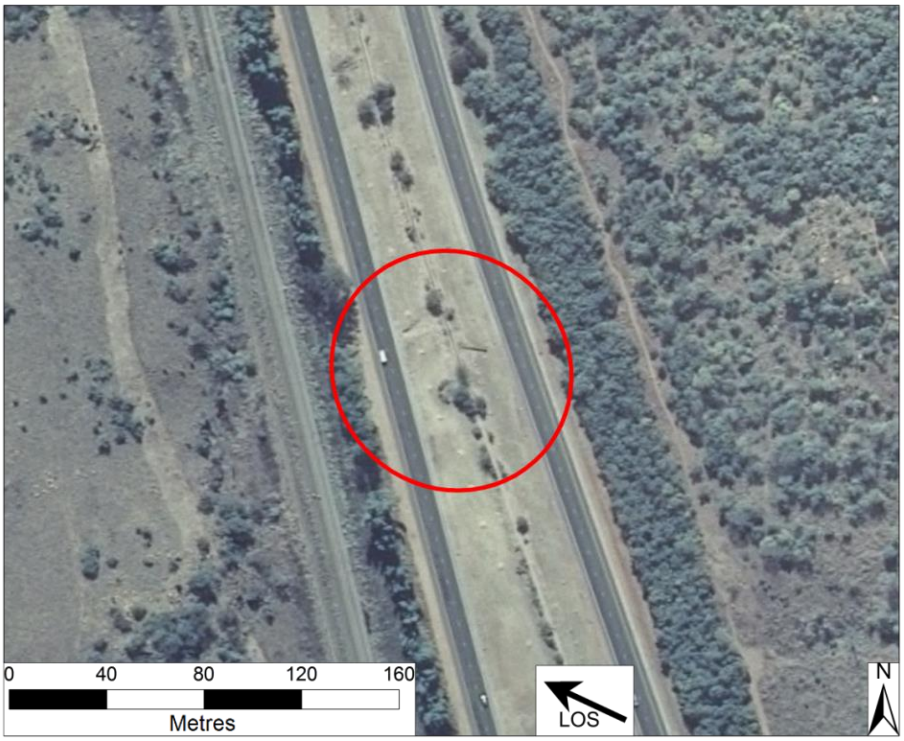

Figure 4.27 High-resolution aerial imagery indicating the location of event B3 between two roadways.

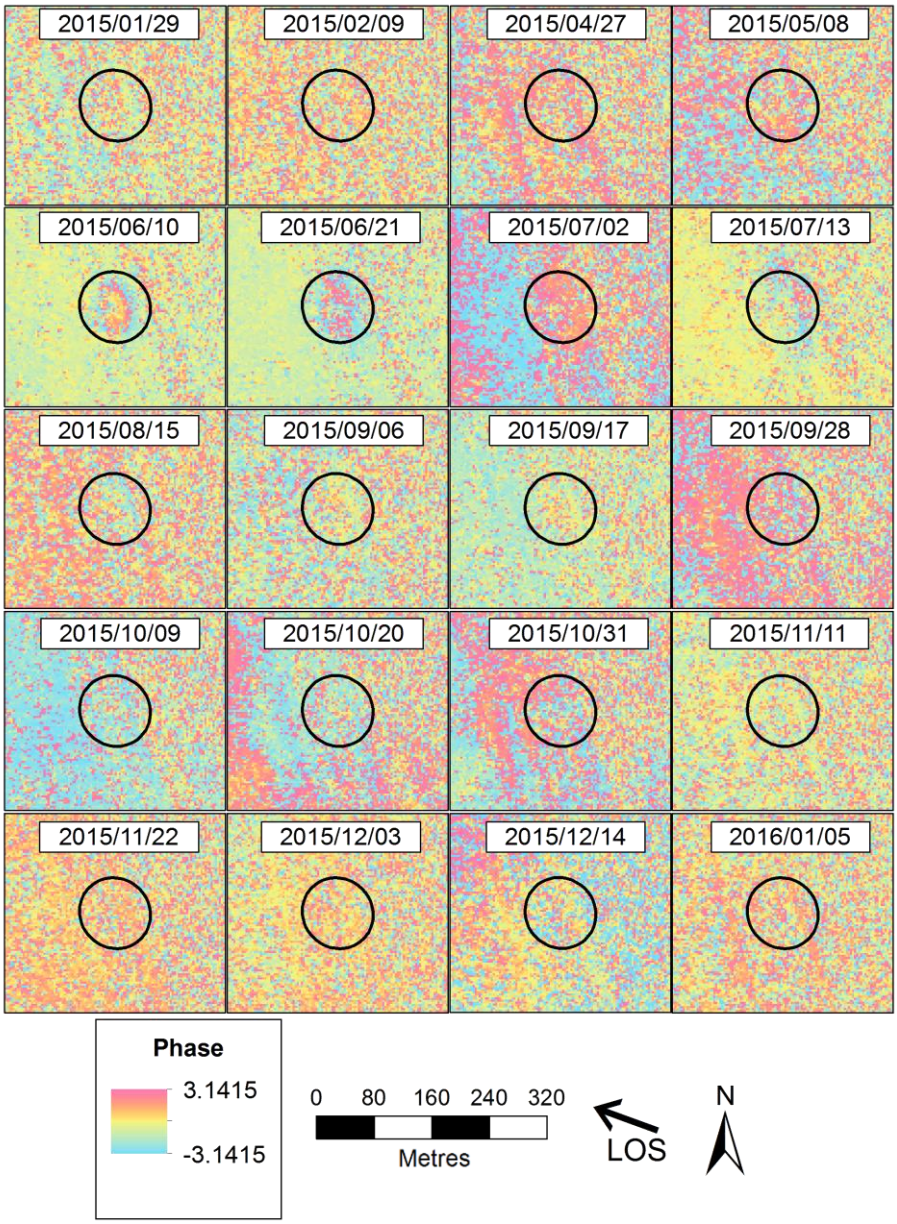

Figure 4.28 Interferograms for the area round event B3 with the subsidence and its approximate extent indicated with a black circle. Only the master date for each image pair is provided, the slave date of each image corresponds to the master date of the following image. The final slave date for the interferogram with the 2016/01/05 master is 2016/01/27. Deformation is observed between interferogram master dates: 2015/06/10 and 2015/06/21.

Displacement maps are shown in Figure 4.29. These reveal that deformation was most pronounced during the first interferogram period (2015/06/10 to 2015/06/21) with a maximum uplift of 6.1 cm while 2.1 cm was detected over the second interferogram between 2015/06/21 and 2015/07/02. The deforming area is approximately 85 metres long and 30 metres wide and it appears as though its width is constrained by the paved roadway.

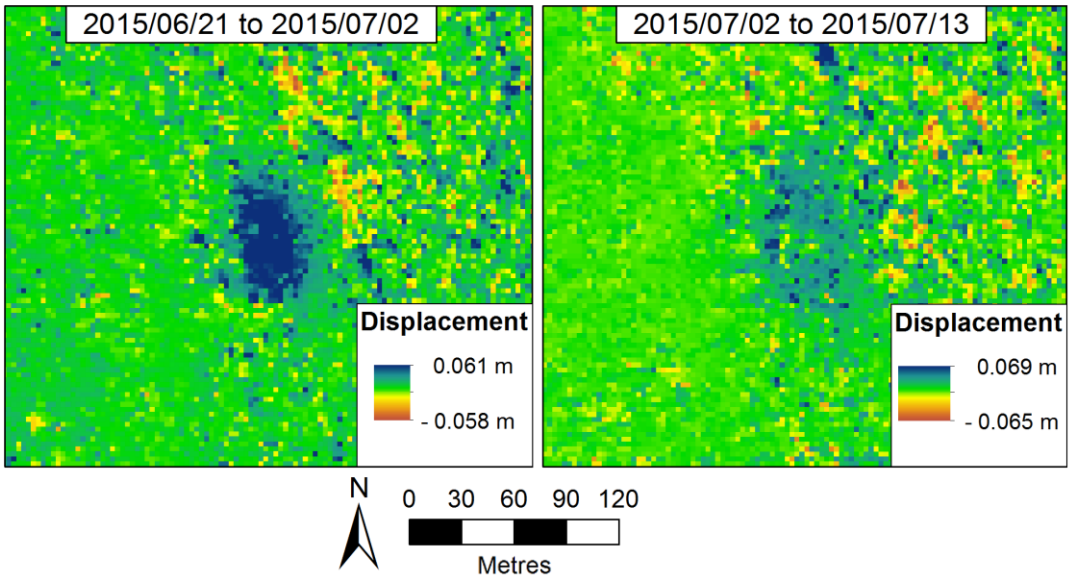

Figure 4.29 Vertical displacement maps of Event B3. Displacement was entirely positive and relate to the uplift of the ground surface. The most pronounced uplift (approximately 6 cm) occurred between the first acquisition pair.

The area was investigated by the Council for Geoscience during January 2016 and no signs of deformation were seen on the surface. Field photographs (Figure 4.30) reveal that the roadside vegetation has recently been cut which could have destroyed evidence. The investigation further revealed storm water culverts with actively growing vegetation within, indicating that water is present here. These culverts are in the centre, and running parallel to, two roadways. There are smaller culverts feeding perpendicularly into the main culvert from the road. The main land cover type is grassland with larger bushes found within the stormwater culverts. Uplift in an area of known dolomite, especially when water is actively channelled in the area, can indicate potentially hazardous conditions. An increase in underground cavity water pressure, for example, can lead to surface uplift. However, the uplift occurred during the dry season. No rainfall events that could have resulted in large volumes of water flowing through the culverts were expected during this season (see Section 1.5). Nevertheless, other wet services could be associated with the area and additional site investigations were recommended. No sinkhole had formed in the area by the time of publication.

Photo: Council for Geoscience

Figure 4.30 Field photograph of the area where the uplift was detected for Event B3. Note the road, recently cut roadside vegetation and green vegetation found within culverts indicating the presence of water.

Chapter 5
Discussion of DInSAR for sinkhole precursor detection

This chapter discusses the implication of the research results discussed in Chapter 4 in context of sinkhole precursor detection. Event B1 (Section 4.3.1) was the most important result of this study as evidence was provided of the successful detection of ground deformation before sinkhole related infrastructure damage. Such a single event detection and analysis is significant since only a few events have been described in literature (Colesanti et al. 2005; Jones & Blom 2013; Nof et al. 2013; Chang & Hanssen 2014; Intrieri et al. 2015). Two more possible deformation basins were detected. These results support the initial research statement that SAR Interferometry is able to monitor ground deformation related to sinkhole development in the study area. Comparisons between interferometric results and the sinkhole events that were recorded on the ground (see the sinkhole inventory in Table 3.2) revealed challenges to detecting sinkhole precursors in the study area. Not one of the reported sinkhole events or associated precursory deformation could be identified on the interferogram stack. While this reveals major limitations to this technique, it also provides the opportunity to assess the limitations of the technique to guide further investigations. Limitations to DInSAR for sinkhole detection could therefore be identified through case studies of unsuccessful and successful detections presented in Section 4.2 and Section 4.3 respectively. The success of detection depended on two broad sets of considerations, the first was related to SAR system parameters and the second to the physical properties associated with sinkhole development. These are interrelated, yet distinct, and will be discussed in Section 5.1 and Section 5.2 respectively.

5.1 SAR system and processing considerations

Successful SAR interferometry is dependent on specific considerations that relate to the properties of the SAR system as well as processing techniques applied to the data. There are various important parameters, the most relevant of which are discussed in Section 2.3, that need to be considered to investigate particular physical processes. Published DInSAR sinkhole precursor investigations are based on different SAR systems, platforms and processing techniques. Generalised conclusions can therefore not be drawn and specific approaches are not necessarily relevant to conditions elsewhere. SAR platforms used by other researchers include ground-based (Intrieri et al. 2015), airborne (Jones & Blom 2013) and spaceborne (Nof et al. 2013) platforms. Previous investigations proved that precursors could be detected using all three common SAR wavelengths including X-band (Nof et al. 2013), C-band (Chang & Hanssen 2014) and L-band (Jones & Blom 2013). Conventional DInSAR processing is often used (Nof et al. 2013), yet SBAS (Galve, Castañeda & Gutiérrez 2015), PSInSAR (Chang & Hanssen 2014), SqueeSAR (Stuecheli, Vaccari & Acton 2012) and 4-D Imaging (Calo et al. 2011) have been investigated with limited success.

Based on the results of this investigation, particular parameters that are essential for successful sinkhole precursor detection could be identified. These are discussed in Section 5.1.1 to Section 5.1.5.

5.1.1 Resolution and swath width

It is important that small-scale deformation patterns be identified on interferograms if DInSAR is to be used operationally. Sinkholes in Gauteng are generally small which could make them difficult to differentiate from typical interferogram noise (Kim, Lu & Degrandpre 2016). It has been noted that deformation smaller than 10 x 10 neighbouring pixels will be difficult, if not impossible to detect (Massonnet & Feigl 1998). TerraSAR-X was chosen in part for its very high spatial resolution and pixel sizes of ~3 m were achieved during this study. This translates to a theoretical minimum deformation basin of approximately 30 m x 30 m (Massonnet & Feigl 1998). Approximately 86% of sinkholes in the study area are less than 15 m in diameter, with the average being 8.5 m in diameter. Only 14% of sinkholes that occur in Tshwane are larger than 15 m. (Richardson 2013). Considering this, it is apparent that most of the sinkholes fall in the range that will be very challenging to detect on an interferogram.

Comparing deformation basins that were detected through DInSAR with the sinkhole events reported in the study area shows that all deformation basins detected through DInSAR were larger in spatial scale than the recorded sinkhole events (Section 4.2). The successful DInSAR deformation detections, events B1 to B3, were between 40 m and 100 m in diameter while the recorded sinkholes in the inventory were between 6 m and 20 m along their widest axis. The largest sinkhole that was reported in the inventory was 20 m in diameter (event A5), and no deformation could be detected associated with this event (Section 4.2.5). Both deformation basins associated with event B1 (section 4.3.1), as well as deformation recorded for events B2 and B3 (section 4.3.2 and 4.3.3 respectively), were small in scale, less than 100 m wide. The second detection of Event B1 was particularly small-scale, being only ~40 m wide. This is comparable to the smallest sinkhole related deformation detections reported in the literature. This includes the 20 m – 40 m wide deformation detected in the Netherlands using medium resolution ERS-1,2, ENVISAT and Radarsat-2 data (Chang & Hanssen 2014) the recent Sentinel-1 detection of salt mine collapse related sinkholes ~110 m and 500 m wide (Kim, Lu & Degrandpre 2016), the 350 m wide feature detected with UAVSAR (Jones & Blom 2013), as well as the 100 m wide feature detected using Cosmo-SkyMed (Nof et al. 2013) (Section 2.2.5).

The non-detection of the smaller inventory events in this study was anticipated due to the known limitations of spatial resolution as well as the historical size distribution of sinkholes in the study area (Section 2.1.3). The TerraSAR-X stripmap mode data used in this investigation, considering the 10 by 10-pixel detection minimum (Massonnet & Feigl 1998), is capable of detecting events of 30 m or larger. It follows that for a system to be capable of detecting the average ~8 m sinkhole in

Tshwane, sub-metre resolutions of 0.8 m or better would be required using conventional DInSAR processing algorithms. It should also be noted that, even though the historical size distribution of sinkholes is smaller than the theoretical minimum of TerraSAR-X, previous investigations have shown that precursory deformation can be larger in extent than the sinkhole itself (Section 5.2.2). This suggests that precursor detection may be possible, in cases, even when lower resolution data is used.

The data swath size is a related consideration. Many events occurred during the study period but were outside the acquisition footprint and could therefore not be investigated. This highlights the importance of considering the swath size as well as the spatial resolution when investigating sinkhole precursors (Section 2.3.2). Larger footprints maximise the extent of the area that can be monitored. However, a larger image footprint is usually achieved at the expense of spatial resolution. Furthermore, this illustrates the importance of accurate sinkhole-hazard probability maps to identify areas most at-risk for sinkhole formation. A map of known dolomite was the best source of information for this study to assess the spatial probability of sinkholes occurring and to select the footprint for acquisitions (Figure 1.2). However, this map was found not to be a reliable indicator of sinkhole events. Not one of the deformation features that were detected using DInSAR actually occurred in areas of known dolomite on this map. Furthermore, only four out of the seven sinkhole-inventory events occurred in areas of known dolomite. Therefore, refinement of dolomite occurrence maps and the associated sinkhole hazard maps are recommended.

5.1.2 Wavelength

The maximum detectable deformation gradient (MDDG) imposes an upper boundary to the detectable magnitude of deformation (Section 2.3.1). This fundamental limitation to interferometry could have led to the missed detections of sinkhole precursors for the inventory events, especially due to the short wavelength X-band system used. Deformation exceeding a maximum of 15 mm per pixel between acquisitions would have resulted in noise. In practice, signal decorrelation and phase unwrapping limitations may limit this gradient even further (Sun & Muller 2016).

The deformation detected during this study suggests that deformation was in the order of 10 mm – 100 mm between acquisitions (11 days – 33 days) across features between 40 m and 100 m in extent. Shorter wavelengths are more sensitive to deformation, yet also more prone to temporal decorrelation (Section 2.3.1). For example, the deformation detected on Basin 2 of event B1 reached a maximum of 2.2 cm over 22 days. This translates to slightly more than a single fringe cycle over the ~40 m feature (13 pixels) making identification of the deformation basin challenging in a typically noisy interferogram (Kim, Lu & Degrandpre 2016). On X-band, a 2 cm deformation feature over the 13 pixels would be ~1.3 fringes on the interferogram. The same feature on C-band would be ~0.7 fringes and on L-band, only ~0.2 fringes. Deformation resulting in such a small fraction over the feature would be challenging to identify. However, the ability to recognise these

features would be dependent on the level of signal decorrelation in the neighbouring pixels. Longer wavelengths generally result in less noisy interferograms due to the signal's penetrative capability.

5.1.3 Temporal baseline

Short temporal baselines are important for sinkhole precursor detection for several reasons. The time-frame between precursory deformation and ultimate sinkhole development is unpredictable and can be as short as a couple of days but also as long as a few months or even years. In the first case, if sinkhole precursors occur in a short timeframe before sinkhole development, very short temporal baselines would be required to provide early warning. For events A6 and A7 (Section 4.2.6 and 4.2.7 respectively) for example, the results suggest that precursors may have occurred in the time frame leading up to the event and that a better temporal frequency of data acquisitions would be required for their detection.

Shorter temporal baselines would also be required where there is a high probability that deformation exceeding the MDDG limit would be present (Sun & Muller 2016) although this would be dependent on the resolution (Section 5.1.1) and wavelength (Section 5.1.2) of the data.

Sinkholes are non-linear deformation events in the order of meters deep (Richardson 2013). They cause decorrelation by exceeding the MDDG limit as well as by physically altering to ground surface. Therefore, any detectable precursory deformation occurring on the same interferogram as the eventual sinkhole will be undetectable. For example, the date of sinkhole event A5 was known to be 2016/01/03. TerraSAR-X acquisitions around this event were captured on 2015/12/14 and 2016/01/05. The sinkhole event is expected to have compromised the interferogram spanning it and precursory deformation occurring in the 20 days before the event could not be detected. The other event with a known date, Event B7 on 2016/01/29 had a similar window of 24 days where precursory deformation would not have been detected even if it occurred. Without knowing the exact date of the other five events, it cannot be known whether precursory deformation did not occur or whether it was masked by the sinkhole event. This was a particular challenge with Event A1 where the interferogram covering the sinkhole event had a large temporal baseline of 77 days. This emphasises the need for reliable, frequent observations to avoid this effect.

In addition to the MDDG, temporal decorrelation due to the presence of vegetation and land cover changes can also cause signal decorrelation. Increasing the temporal baseline is known to increase the effects of temporal decorrelation (Section 5.1.5) which also justifies the use of short temporal baseline data (Section 2.2.2.3). However, when very small deformation rates are expected, short temporal baselines may make deformation fringes difficult to detect, especially in the presence of phase noise as was observed for the second deformation basin of event B1 (Section 4.3.1).

5.1.4 Incidence angle and LOS

A challenge for the detection of sinkhole precursors is the side-looking geometry of the sensor and the phase measurement that occurs in the line-of-sight (LOS) of the sensor. Ground deformation occurring behind impenetrable obstructions due to the incidence angle of the SAR is in radar shadow and impossible to detect (Intrieri et al. 2015). The incidence angle used for this study results was 40.9° and the radar was facing west. The urban and peri-urban nature of the study area is characterised by complex natural and man-made obstructions to the SAR that include buildings, walls and trees as was observed for Event A6 (Section 4.2.6) and Event A5 (Section 4.2.5) respectively. Longer wavelengths are capable of increased penetration through vegetation (Section 2.3.1.) and should improve precursor detection capability in areas of thick vegetation, including residential areas. Steep incidence angles can reduce the amount of radar shadowing due to impenetrable features, however, steeper incidence angles lead to reduced spatial resolution in range that needs to be considered.

Furthermore, deformation measurements for conventional DInSAR are only in the LOS of the SAR (Section 2.3.5), ground deformation likely has components in all three dimensions. A recent DInSAR sinkhole precursor detection, in fact, showed deformation primarily in the horizontal component (Jones & Blom 2013; Jones & Blom 2015). A three-dimensional velocity measurement is ideally required which can only be derived by the combination of deformation measurements from ascending and descending orbits. Three-dimensional deformation basins that can be derived from multi-angle data acquisitions (Hooper & Zebker 2007) should be considered for future research to test the assumption of vertical deformation as adopted in this investigation.

5.1.5 Coherence

Differential interferometry's detection ability depends on the ground surface remaining coherent between image acquisitions. Coherence is a measure of phase return stability between acquisitions and is expressed as a value between zero and one, one being total correlation and zero being total decorrelation (Section 2.2.2.3). Various factors influence coherence, some relate specifically to the properties of the radar, while others are dependent on the specific conditions of the ground or the interaction between the ground and radar (Alberga 2004). Two factors are particularly relevant: 1) surface scattering processes that depend on the nature of the scatterer (double bounce vs surface vs volume) as well as the change in look angle between acquisitions (perpendicular baseline) and 2), the temporal change of scatterers between acquisitions (vegetation growth, erosion *etc*.) dependent on the temporal baseline. See Section 2.2.2.3 for a comprehensive discussion on these factors. Understanding which of these factors led to challenges in detection is critical for reliable detection of sinkhole precursors.

Analysing the temporal distribution of the DInSAR detections (Section 4.3) it became evident that deformation feature detections were visible predominantly over two periods between 2015/06/10

and 2015/08/15 as well as 2016/10/20 to 2015/11/11. These deformation detection periods were associated with periods of high coherence. Furthermore, coherence fell drastically after these periods implying that deformation might have been ongoing, but was not detectable due to phase decorrelation. This affected deformation measurements as was illustrated in the time series of coherence maps presented for Event B1 (Figure 4.22). Low coherence, therefore, led to uncertainty in constraining the end of the detected deformation events discussed in Section 4.3. To investigate the decrease in coherence over the study period, the average global scene coherence was considered together with factors that are known to affect coherence. This includes the perpendicular baseline (Figure 5.1 A), the temporal baseline (Figure 5.1 B), the presence of vegetation (as approximated by Enhanced Vegetation Index (EVI) data) (Figure 5.1 C) and rainfall events (Figure 5.1 C).

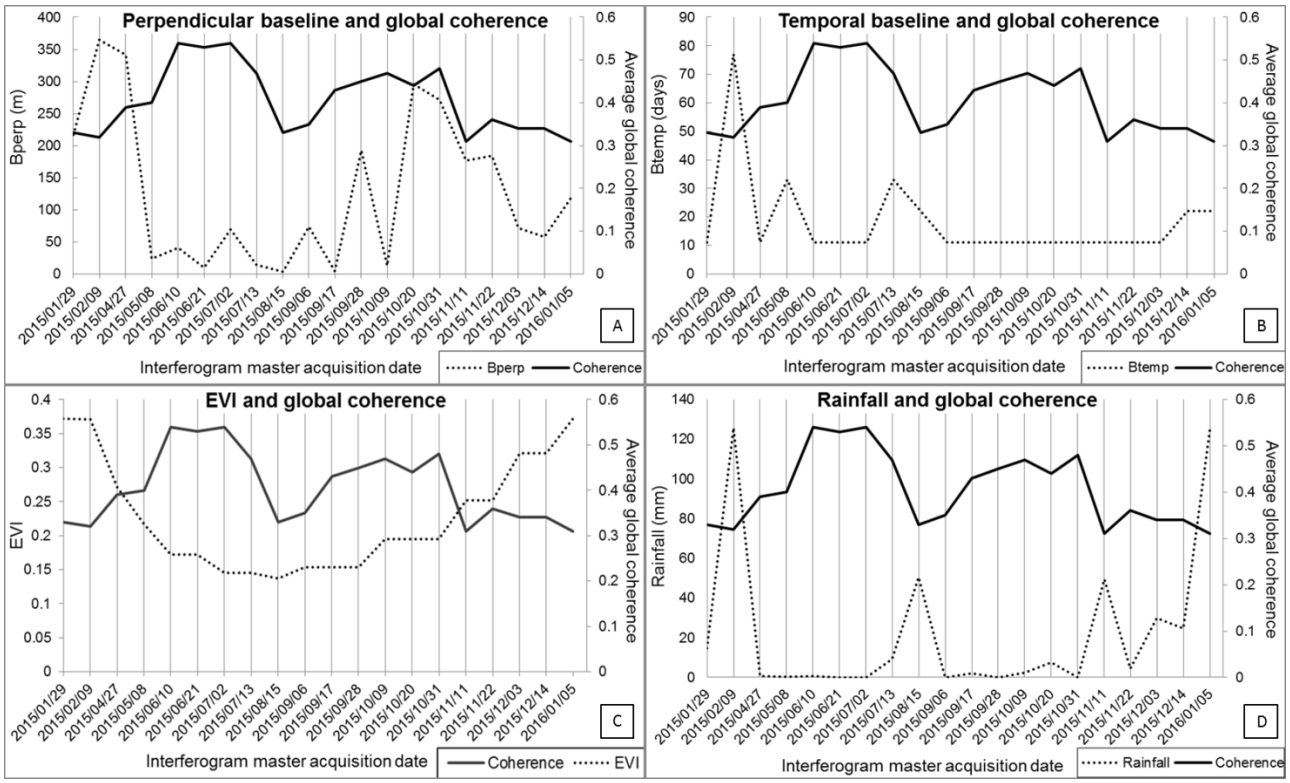

Figure 5.1 Comparisons between globally averaged interferometric coherence and factors that may influence coherence namely A) perpendicular baseline (B_{perp}), B) temporal baseline (B_{temp}), C) Enhanced Vegetation Index (EVI) and D) rainfall accumulation.

The June to August period, in particular, was characterised by high coherence. After 15 August, however, the coherence drops to approximately its lowest level before increasing again over following acquisitions. After 11 November, the coherence drops and remains low for the remainder of the acquisitions. The average scene coherence was 0.5 for the first three detections (B1 - B3, between June and August) and above 0.4 during the later detection of Event B1 (between October and November). It is apparent from all four graphs on Figure 5.1 that coherence conditions were low during the start and end of the study period. This period coincided with high seasonal rainfall (Figure 5.1 D) as well as the peak of the growing season of vegetation as indicated by high EVI

values (Figure 5.1 C). Incidentally, the first three interferogram combinations between 2015/01/29 and 2015/04/27 are also associated with high perpendicular and temporal baselines, increasing the probability of signal decorrelation. However, for all interferometric pairs, the perpendicular baseline was less than 350 m (Figure 5.1 A), which is low relative to the critical baseline of 6 km for the system (Section 2.2.2.3). Therefore, the link between decreases in coherence and perpendicular baseline conditions was expected to be low. This was confirmed by the observed low correlation between coherence and perpendicular baseline in Figure 5.1 A.

The temporal baseline started relatively high, with a baseline of 77 days for the 2015/02/09 to 2015/04/27 pair and 33 days for the 2015/05/08 to 2015/06/10 and 2015/07/13 to 2015/08/15 pairs. The following pairs exhibited temporal baselines between 11 and 22 (Figure 5.1 B). One notable exception of 33 days in July corresponds to an initial drop in observed coherence. The decrease in coherence observed in August 2015, on the other hand, was not related to large temporal baselines.

The radar scattering processes on the ground also influence coherence. Specular reflection from smooth surfaces such as water bodies and paved surfaces results in low backscatter returns and low coherence (Leblanc et al. 2015). Furthermore, volume scattering, from vegetation results in incoherence depending on the wavelength used and the nature of the vegetation (Section 2.2.2.3). This effect is more pronounced for shorter wavelengths that are unable to penetrate through the vegetation canopy. Figure 5.1 C shows the monthly average EVI as well as average global coherence. The peak of the growing season is over January for this area, and this time was associated with the lowest observed coherence. There is an initial relationship between the end of the growing season and an increase in coherence, however, the coherence loss during August and October are not associated with an increase in EVI. Vegetation phenology, therefore, cannot fully explain the decrease in coherence for all areas over the entire time series.

Rapid landscape evolution due to disturbance by factors such as the wind, rainfall, erosion or human activities also lead to a loss of coherence (Thiel & Schmullius 2016). Since these disturbances can occur over short time periods, they are not strictly dependent on the temporal baseline but can result in decorrelation of the signal. Rainfall events, in particular, can lead to rapid landscape changes but also affects radar backscatter amplitude that is used for the calculation of interferometric coherence. Rainfall events can, therefore, reduce coherence due to its ability to change surface conditions but also due to the change in dielectric properties of the surface due to a change in moisture conditions at the time of image acquisitions. The rainfall accumulation was used as a measure to investigate the effect of rainfall on the interferometric coherence. The rainfall accumulation, shown in Figure 5.1 D, is the total amount of rainfall that was recorded between the master and slave acquisitions. The results indicate that there is a strong inverse relationship between accumulated rainfall and coherence with an increase in accumulated rainfall being associated with a decrease in coherence. Importantly, the results indicate that an increase in

rainfall was recorded for the interferograms spanning 2015/08/15 to 2015/09/06 and 2015/11/11 to 2015/11/22. These periods were associated with decreased coherence. The drop in coherence associated with the rainfall event affected the detection of deformation associated with events B1 and B2 since their final date could not be accurately constrained due to unreliable interferograms with low coherence following the initial deformation observation. In fact, for event B1 in which deformation was detected over two distinct periods, both of these detection periods ended after high rainfall was recorded. It is probable that deformation was ongoing, yet undetectable, due to incoherence caused by rainfall events. The rainfall events may also have masked the deformation signals associated with some of the undetected sinkhole inventory events discussed in Section 4.2.

Loss of coherence is a fundamental limitation to DInSAR techniques. Time series stacking methods should generally not be affected by such drops of coherence as only stable, coherent pixels over the time-series is incorporated (Ferretti, Prati & Rocca 2001; Ferretti et al. 2011). However, because of the pixel selection used by these methods, they would not be able to detect the deformation occurring on pixels that do not remain coherent over the entire data stack (Section 2.2.3.3). Such low, and variable, coherence pixels were seen in all detected deformation events, but particularly for event B1.

Urban areas generally have higher coherence than agricultural or natural vegetation areas. A large part of the footprint falls over an urban area. However, many areas prone to sinkhole formation are not densely built up and can be classified as disturbed grasslands. Furthermore, many of the residential neighbourhoods are characterised by the presence of vegetation in gardens and parks or open fields and would be prone to losing coherence. Consequently, coherence was too low (less than 0.3) for successful interferometry over many areas, especially during the peak of the growing seasons.

5.2 **Physical considerations**

The physical characteristics of sinkholes and their precursors present the second set of important considerations for the successful DInSAR detection for sinkhole-induced deformation. It is important to consider that a lack of precursory deformation may always be a limitation of early warning systems based only on surface deformation monitoring. There is a need to better understand the geological nature of sinkholes, particularly to assist appropriate SAR and processing technique selection for future studies (Szwedzicki 2001; Parise & Lollino 2011; Vaccari et al. 2013). Furthermore, it is important to understand sinkholes in the local environmental context since generalisations cannot be made from the variety of detections reported on in literature. The relevant physical considerations that were observed in this investigation are discussed in Sections 5.2.1 to 5.2.4.

5.2.1 Presence of precursors

If precursory deformation is not present for a reasonable period before sinkhole collapse there can be no early warning given based on such subsidence. It is possible that this fundamental physical limitation contributed to the inability to detect some of the sinkhole events recorded in the inventory. However, due to SAR limitations (Section 5.1) as well as a lack of *in situ* information (Section 5.2.4) this study is not able to confirm the possibility that no precursory deformation occurred before these events. Nevertheless, one event, (Event A5) supports the possibility that no precursory deformation was present. For this event, the results showed that a full year of acquisitions preceded a large sinkhole (20 m x 13 m in diameter) that occurred in an area of typically high coherence. Since the event was sufficiently large and coherence was generally high in the area immediately surrounding the event, it is probable that, if precursors were present, they would have been detectable on the DInSAR results. Therefore, there is a high likelihood that precursory deformation was not present over a period longer than the final temporal baseline immediately prior to sinkhole development.

A lack of precursory deformation can be ascribed to either the geology or the land cover type. It has been noted that the specific geology of the study area may lead to cases where instantaneous collapse occurs instead of gradual deformation (Avutia 2014). This is due to the competent chert component of the dolomite leading to areas with resistant caprock present over cavities (Section 2.1.3). The land cover over the developing sinkhole can also be competent and resistant to gradual movement and thereby lead to collapse. Examples of such cover material include roads, building foundations and pavement visible on the field photographs (Figure 5.2 and Figure 4.10).

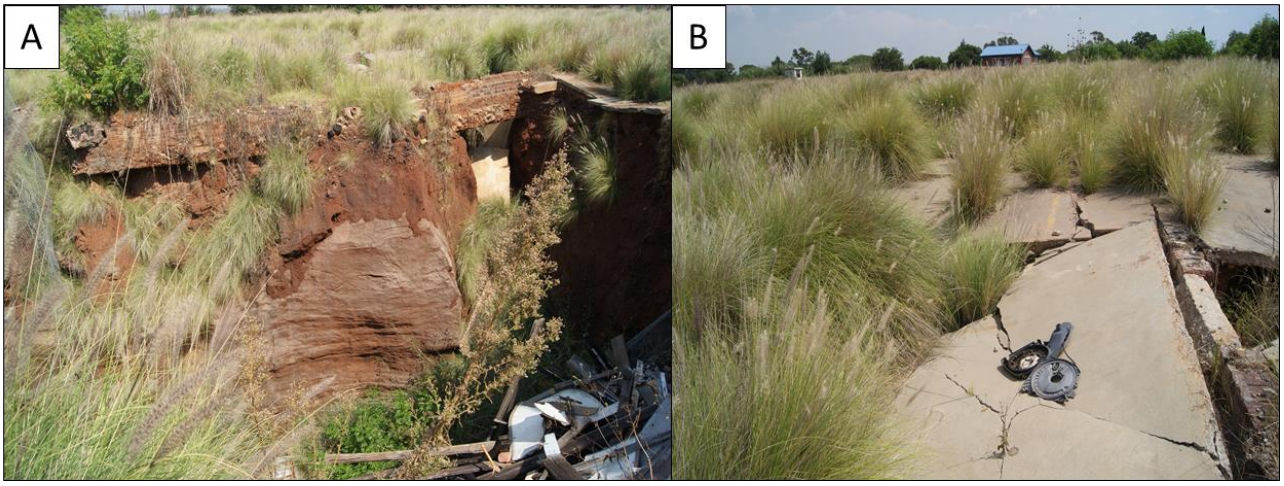

Photo: Author

Figure 5.2 Competent land cover types capable of resisting gradual subsidence leading to sinkhole events not preceded by precursory deformation. A) Building foundation revealed to remain resistant to deformation after a sinkhole collapse and B) shows pavement damage after sinkhole formation, yet remaining intact even after the event. These events occurred before the study period.

Competent land cover types were identified near Event B3 and Event A5. The deformation detected during Event B3 seemed to be constrained by two roadways (Figure 4.28 and Figure 4.30). Displacement might, in fact, be occurring under these roads but remain undetectable to the SAR. The land cover type could also explain why no precursory deformation was detected for Event A5, as discussed above. The field photograph of the event (Figure 4.10) reveals pavement surrounding the sinkhole that could have masked precursory deformation. It should be noted that the urban structures discussed here often have a high coherence and persistent scatterer techniques might be able to detect smaller deformation of such structures than conventional DInSAR (Ferretti et al. 2005; Ferretti et al. 2007; Buchoud et al. 2016).

5.2.2 Physical characteristics

The physical characteristics of sinkhole events are important considerations that guide both the data acquisition strategy and detectability of sinkhole precursors. The physical considerations that were relevant during this DInSAR investigation include 1) the timing of deformation prior to the sinkhole development, 2) its spatial extent, 3) the magnitude of deformation and 4) the displacement direction.

The timing of precursory deformation prior to the sinkhole forming is an important limitation as it controls how early a warning can be provided by DInSAR. The timing is therefore related to the temporal baseline of the SAR system discussed in Section 5.1.3. The detections made during this study showed that dolomite-related deformation can be ongoing for weeks to months before sinkhole formation (Event B1, Section 4.3.1) compared to years reported by Chang and Hanssen (2014), or hours theorised by (Closson et al. 2005). This result corresponds to two of the most relevant precursory deformation detections reported in literature, one over evaporate terrain with sinkholes related to dewatering (Nof et al. 2013), and the other over carbonate karst related to ingress of water similar to what is expected in the study area (Intrieri et al. 2015). The temporal evolution of the detected deformation may also be important, this should describe the deformation as ongoing over long periods vs. discrete events over short periods. During the study, it was found that some deformation basins exhibit deformation for periods of weeks to months. However, coherence limitations may have influenced our ability to constrain the end-date of deformation (Section 5.1.5). Furthermore, the relatively low temporal sampling rate of spaceborne SAR sensors limits discriminating between discrete and continuous deformation activity as only a single deformation measurement is made between orbits.

The spatial extent of precursory deformation is another important limitation. The limit of the smallest deformation feature that can be detected using conventional DInSAR techniques is related to the spatial resolution of the SAR scenes used as discussed in Section 5.1.1. The extent of the deformation features detected during this investigation (between 40 m and 100 m) was in

similar ranges as previous satellite-based detections (Jones & Blom 2013; Nof et al. 2013; Chang & Hanssen 2014).

However, the sinkhole events reported in the sinkhole inventory were smaller than 20 m in diameter and no deformation was detected associated with their development. This suggests the possibility of deformation being smaller than the minimum detectable deformation size of ~ 30 m (Section 5.1.1). Previous research has shown that sinkhole precursors can be larger than the sinkhole event itself with some events exhibiting deformation four times as large as the final sinkhole (Chang & Hanssen 2014; Intrieri et al. 2015). This corresponds to the deformation and sinkhole results of Event B1. However, if precursors associated with inventory events were always larger than four times the size of the sinkhole, then a large number of inventory events would have been detectable assuming that phase noise and the presence of competent land cover types were not present. The size of a sinkhole and related precursory deformation is related to the depth of the original underground cavity (Section 2.1.2). Sinkholes in the study area that form due to a cavity at shallow depth will be preceded by precursors (if any) similar in size to the cavity and ultimate sinkhole. Deeper cavities are expected to create a larger surface signature and are therefore more likely to present detectable precursory deformation.

The third physical consideration is related to the magnitude of precursory deformation. Considerations regarding the magnitude of deformation are related to the maximum detectable deformation gradient limit (and therefore the SAR wavelength, see Section 5.1.2). The magnitude of deformation detected during this study was between 1 cm and 7 cm, which is similar to precursor deformation detected in literature (Section 2.2.5). Deformation magnitudes reported in the sinkhole inventory are much larger than the deformation detected through DInSAR.

This study used conventional DInSAR on subsequent acquisitions to reduce the temporal baselines and therefore detect the highest temporal resolution deformation progression available. Averaged vertical deformation velocities between acquisitions (mean and maximum) could be derived from detected deformation basins to aid comparison. An estimate of the rate of deformation can be made from the deformation Basin 1 of Event B1 (Section 4.3.1.1) using the temporal baselines and maximum/mean deformation velocities. This rate can then be compared between the three detected periods. The deformation detected was not linear over the 55 days of detection and the rate of subsidence declined. The average rate of subsidence declined from 2 cm/day, to 1.5cm/day, over the first two 11-day detections. The rate then declined further to 1.3 cm/day on over the next 33 days. These calculations are based on the maximum depth of the subsidence. Rates based on the average subsidence over the basin instead are 0.8 cm/day, 0.6 cm/day and 0.6 cm/day respectively.

The final physical characteristic of sinkhole precursors that affects DInSAR results is the three-dimensional displacement direction of precursory deformation. SAR interferometry measures deformation in the LOS of the sensor and multi-angle SAR or *in situ* levelling data is needed to

determine the three-dimensional displacement components (Section 2.2.2.2 and Section 5.1.4). Two-dimensional (vertical) deformation was assumed during this study, however, in reality, it is possible that deformation could exhibit a horizontal component as well (Parise & Lollino 2011; Jones & Blom 2015).

5.2.3 Seasonality

The ground deformation detections in grassland areas through X-band (Event B1) show the capability of even X-band to derive deformation measurements in certain vegetated conditions. However, the observation was made during the dry season, increasing the probability of detection (FEWSNET 2016)

Sinkhole events are mainly caused by the ingress of water due to precipitation or leaking servitudes or bad stormwater management (Buttrick et al. 2011; Richardson 2013), This implies that sinkholes can occur at any time of the year and is not limited to the rainy season only. However, an increase in events can be expected during the peak of the rainy season (Buttrick et al. 2011) .However, evidence from this study suggests that rainfall events impose major limitations on DInSAR's detection ability (Section 2.2.2.3). This present a particular challenge since DInSAR's detection capability may be compromised during periods where sinkhole formation is most likely.

Sinkholes that were recorded in the inventory, as well as events detected through DInSAR during this study, were not constrained to the rainfall season. All three events detected (B1 to B3) occurred during the dry winter season between five acquisition dates starting on 10 June and ending on 15 August. With the exception of the very faint second detection of Event B1 that occurred closer to the wet season from 10 October to 11 November. The causes for the recorded sinkhole events noted in the sinkhole inventory showed that all seven events were due to leaking water-bearing services. An anthropogenic origin for most sinkholes is expected for the study area (Section 2.1.3). The leaking water pipe, in fact, resulted in a temporary wetland forming with dense vegetation. Vegetation growth, like rainfall may limit DInSAR's ability to detect deformation in areas where it is more likely.

5.2.4 Field evidence

Evidence of subsidence and sinkhole events from the field were an important part of this study. It was found that a lack of detailed physical information on the sinkholes forming is a complicating factor for comparing DInSAR results to sinkhole events. The ideal outcome of such a comparison would be to understand whether a failed DInSAR detection of precursory deformation is due to no deformation occurring (Section 5.2.1), or alternatively, due to the SAR system and processing steps used (Section 5.1). A sinkhole inventory was obtained for this investigation (Table 3.1) and could be used as a reference for DInSAR hindsight analysis of recorded sinkhole events. Conversely, detected events were investigated in the field for evidence of deformation. If it can be

found that no precursory deformation occurs, it has serious implications for future early warning systems. This study, however, cannot conclude that any precursory deformation occurred for the events in the sinkhole inventory where no deformation was detected due to a lack of *in situ* measurements. On the contrary, the detected events, even though not reported in the inventory, suggest that precursory deformation may be present in some cases.

During this study three deformation events were detected which were not in the sinkhole inventory, proving DInSAR's complementarity. One of the events was confirmed on the ground (Event B1) and led to mitigation measures being initiated by the landowner. Field investigations proved to be an important part of understanding the detected Event B1. Tension cracks were found surrounding Basin 1 and were critical in confirming the DInSAR observations. Although *in situ* measurements of deformation (including levelling and GPS surveys) were not available, the presence of tension cracks provided physical evidence confirming the presence of a deformation basin as detected by DInSAR. The tension crack of Event B1 was only present on one side of the full subsidence basin, likely due to a steeper deformation gradient (Figure 4.20). Tension cracks will not always be present as it depends on the geology and surface cover. However, the presence of tension cracks is recognised by Closson et al. (2005) as the second stage of precursor development (Section 2.1.2).

There were limitations to the information recorded on the sinkhole inventory that resulted in uncertainty in understanding the reasons for DInSAR inability to detect any of the events. The exact location, spatial extent and magnitude of reported sinkholes are essential information in assessing DInSAR's capabilities (Section 5.1.). In the sinkhole inventory, only three out of the seven events had spatial extent and magnitude reported. This resulted in uncertainty in understanding the importance of spatial resolution (Section 5.1.1). The exact date of only two events was recorded which resulted in uncertainty regarding the timing of the detections (Section 5.2.2) as well as uncertainty regarding the role of temporal baseline (Section 5.1.3). Sinkholes forming cause a major disturbance of the earth surface leading to a loss of coherence and likely exceed the deformation gradient limit making a measurement of deformation impossible as discussed in Section 2.3.1. If the date of the sinkhole forming is unknown, it cannot be placed in context with the SAR acquisition timeframe to draw conclusions. Furthermore, there was also uncertainty regarding the exact location of the sinkhole since the inventory only reports a point location where a sinkhole location could not be accessed, the point is just taken as an approximation. This happened with event A3, where the GPS location was taken outside a property, and no further information is available. This leads to uncertainty in understanding non-detections, particularly due to possible radar shadowing challenges for Event A3 (Section 5.1.4)

It is important to note that while the sinkhole inventory obtained was the most reliable source of information that could be obtained, it could not be expected to contain all events that occurred in the area (Oosthuizen & Richardson 2011; Richardson 2013). Many sinkhole events on private and

even public land in South Africa go unreported, mainly since there is no obligation to report a sinkhole event (Oosthuizen & van Rooy 2015). DInSAR thereby provides complementary methods of detecting deformation that was not noticed or reported by landowners and/or authorities and can support sinkhole record collection.

Chapter 6
Conclusion

This study determined that SAR interferometry is able to detect ground deformation prior to sinkhole formation in Gauteng, South Africa. It provides some of the first evidence of a dolomite induced subsidence basin detected through DInSAR in the region. Several more events were investigated revealing key challenges that need to be overcome for DInSAR to inform robust sinkhole early-warning systems. Sinkholes are known to be a major geohazard causing damage to infrastructure and posing a threat to lives and infrastructure in Gauteng (Section 1.5). Recent dolomite management policies are effective at reducing the risk of sinkholes and associated damages (Watermeyer et al. 2008; Potgieter, Pretorius & Walt 2016). These are especially effective at preventing sinkholes from forming since almost all sinkholes are caused by anthropogenic factors, such as leaking water bearing services (Richardson 2013). Nevertheless, sinkholes still occur at a rate of approximately 12 per annum (Richardson 2013) and their management requires constant monitoring for sinkhole development (SABS 2012). It was found that the official recommendations for monitoring do not yet include the potential of SAR interferometry in spite of its potential (Stevanovic et al. 2015; Ozden et al. 2016).

The potential and principles of DInSAR, as a mature technology for detecting small-scale ground deformation over large areas, were considered based on previous investigations (Chapter 2). SAR interferometry has been successfully used in South Africa, especially relating to detecting subsidence due to mining activities (Engelbrecht & Inggs 2011; Engelbrecht & Inggs 2013; Engelbrecht et al. 2014). Furthermore, it is shown that researchers have been interested in its potential for sinkhole monitoring for over a decade (Baer et al. 2002; Closson et al. 2003; Closson et al. 2005). Yet the capabilities of SAR systems and processing techniques have only fairly recently resulted in successful attempts at detecting sinkhole precursors (Jones & Blom 2013; Nof et al. 2013; Chang & Hanssen 2014). Specific considerations were discussed in Section 2.3 that may influence the capability of SAR interferometry to detect sinkhole precursors. Issues relating to satellite revisit time, spatial resolution, wavelength, polarisation and the maximum deformation gradient were highlighted. These were important during SAR platform and acquisition mode selection.

To investigate the use of DInSAR for monitoring sinkhole precursors in South Africa, the Gauteng Province was the focus of the investigation due to the high frequency of sinkhole events and the need for proactive mitigation measures. The results, presented in Chapter 4, is summarised in Section 6.1. The limitations for operational monitoring are summarised in Section 6.2. Recommendations for future research is drawn from the limitations and findings of the investigation (Section 6.3)

6.1 Summary of findings

The aim of this research was to determine whether SAR interferometry is able to detect precursors to sinkhole formation in Gauteng. To investigate the research question, 20 interferograms were generated covering the period 29 January 2015 to 27 January 2016. These were analysed for deformation and were considered in conjunction with ancillary data, including a sinkhole inventory (presented in Section 3.2). None of the reported sinkhole events in the inventory could be identified through DInSAR analysis. Visual analysis of the interferogram and displacement map time series, however, resulted in the confirmed detection of four subsidence basins related to unreported sinkhole events. Drawing from the results and analyses, discussed in Chapter 4 and Chapter 5, the original objectives of this research were addressed. A summary of important findings related to each objective is provided in Section 6.1.1 to Section 6.1.4.

6.1.1 Objective 1

The first objective of the study was to detect and monitor ground deformation prior to sinkhole formation using DInSAR. The detection of surface deformation linked to sinkhole development, as discussed in Section 4.3 and supported by field observations satisfied this first objective. These detections show agreement with recent findings highlighting successful detections of sinkhole precursors using DInSAR techniques discussed in Section 2.2.5 (Jones & Blom 2013; Nof et al. 2013; Chang & Hanssen 2014; Intrieri et al. 2015; Jones & Blom 2015). In particular, the research findings illustrated that subsidence related to sinkholes occurring in the Gauteng dolomites is present and detectable through DInSAR techniques. This supports the notion that DInSAR can contribute to an early warning system.

6.1.2 Objective 2

The second objective of this research was to compare the DInSAR results to sinkhole events reported on the ground. On inspection of the results, none of the reported events exhibited deformation signatures on the DInSAR results. It was anticipated that there would be challenges to detecting all these events, yet none of the sinkholes could be detected. These unsuccessful detections revealed important limitations and considerations for DInSAR if considered for early warning systems. These limitations, informing the third objective, was found to be related to SAR systems and processing parameters as well as the physical characteristics of the sinkhole events in relation to these parameters.

6.1.3 Objective 3

The third objective of this study was assessing the limitations inherent to the data and processing techniques. It was found that the most important challenge for operational detection of sinkhole precursors was the spatial scale of the deformation event, relative to the resolution of the SAR

system. It is well known that deformation cannot reliably be detected by a single pixel and sinkhole size has been identified as a challenge for sinkhole precursor detection (Intrieri et al. 2015). Sinkholes investigated in previous studies have generally been large-scale features (larger than 100 m as discussed in Section 2.2.5) often in evaporite terrain. These previously reported sinkhole sizes are unlike the sinkholes found in the karst geology of Gauteng, which are generally less than 15 m in diameter (Richardson 2013). Based on this known size distribution of sinkholes in the study area it was expected that they would be on the lower limits of detectability by conventional DInSAR on the 3 m resolution SAR system. Testing this technique showed that detection is possible but the smallest detected subsidence basin was larger than the largest recorded sinkhole. Small sinkholes in the study area are challenging to detect due to this fundamental limitation and it is imperative for further studies to compensate for this.

Another limitation due to SAR properties is a lack of detection due to the maximum detectable deformation gradient. Since precursory deformation detected in this study, and those reported elsewhere, is in the order of centimetres this limitation does not present a challenge itself as discussed in Section 5.1.2. Yet, if the precursory deformation and the sinkhole both occur between two acquisitions, the precursory deformation will have been masked by the sinkhole. If the time is very short between the sinkhole and the precursor then detection is not possible. This limitation has also been pointed out recently by (Intrieri et al. 2015).

The limitations due to spatial scale and magnitude have been noted in the literature, yet coherence challenges-related are not generally assessed in studies on sinkholes precursor detection. Temporal and perpendicular baselines were relatively small during this study, resulting in potentially high coherence. However, the presence of vegetation during the growing season and rainfall events between acquisitions resulted in a significant loss of coherence that affected the ability to derive high fidelity displacement maps. The results show that sinkhole precursors could only be detected within certain periods of high coherence. These occurred during the dry, winter season where no rain fell between acquisitions. This has important implications for an early warning system, particularly a system based on X-band SAR. It is significant to point out that many of the previously reported sinkhole precursor detections were achieved in arid areas such as Jordan (Closson et al. 2005), Israel (Nof et al. 2013) and Texas (Kim, Lu & Degrandpre 2016) with the notable exception of (Jones & Blom 2013) where coherence was maintained by L-band tree trunk interactions in a wetland environment.

The final and more fundamental limitations are due to the nature of sinkhole precursors themselves. It is possible that no precursory deformation precedes sinkhole development. The presence of chert bands in the study area, known for brittle failure with little warning (Avutia 2014), affect the potential for precursory deformation to be expressed. Furthermore, competent land cover types, like concrete, buildings or paved roads may be resistant to deformation and mask the expression of precursory deformation at the surface. Furthermore, precursory deformation might

only occur shortly before the sinkhole and deformation signatures is therefore masked by the sinkhole event depending on the temporal frequency of image acquisitions. Finally, the deformation magnitude may be too small to be detectable, especially in the presence of signal noise. Understanding the importance of these fundamental limitations can only be done if more is known about precursory deformation in the study area.

6.1.4 Objective 4

The final objective of this study was to identify considerations for detection related to the characteristics of sinkholes and their precursors in the study area. The results revealed that in cases precursory deformation was present and detectable at least a few months before sinkhole formation. However, more observations would be needed to draw accurate conclusions on the temporal evolution of deformation and the rates of deformation preceding sinkhole events. In particular, the deformation prior to sinkhole development is expected to be highly variable over space and time and will be dependent on 1) the size and depth below surface of the cavity, 2) the composition of the roof strata, 3) the process and mechanism of cavity formation and 4) the landcover at the surface. Therefore, significant time-frames of observation and very detailed field campaigns would be required to draw accurate conclusions regarding the nature of precursory deformation in the study area.

The results of the DInSAR measurements revealed that the magnitude of deformation magnitude was small, and could be detected over time spans as short as 11 days. In cases, precursory deformation was detectable for months leading up to the event, when visible signs of subsidence have not formed yet. These results are further support for DInSAR as a tool for early warning. Once cracks appear it could be mere hours until the sinkhole forms (Colesanti et al. 2005) and DInSAR-based consistent wide area monitoring of fine scale deformation is a promising technique to detect such deformation and therefore provide early warning even before cracks can be noticed. However, since such small-scale deformation often does not result in visible damages on the surface it shows that field verification will continue to be a problem in DInSAR sinkhole investigations (also noted by Vaccari et al. 2013). The detected basins were smaller in scale than most reported in the literature, yet was still larger than the most common sinkholes present in the study area. This indicated a challenge to the technique that became apparent when the sinkhole inventory was compared to the DInSAR result in support of the second research objective.

Reported sinkhole events are limited to those that are noticed by people, which implies that deformation must be deep enough to cause some kind of visible damage or cracks in the ground. DInSAR's sensitivity becomes very useful in this case since it measures actual ground deformation and is not reliant on reactive assessment after the damage has been noticed. As an example, field investigations of Event B1 showed a crack in the ground a few cm wide and tens of metres long, that was not noticed by the property owners. However, the crack only appeared on the eastern

periphery (where the deformation gradient was the steepest). No visible signs were found over the rest of the detected deformation basin. DInSAR is, therefore, a complementary data source for a sinkhole inventory and furthermore is able to detect small-scale deformation that may go unnoticed in inventories.

6.2 Limitations to the study

Although the potential of DInSAR techniques for the detection of sinkhole precursors in dolomite terrain was demonstrated, the investigation was limited by several factors. The limitations include the short time-frame under investigation, the limited sample size of successful detections, as well as the lack of detailed ground-truth observations.

Small sample size - A large sample size of detections is desired for an accurate understanding of DInSAR's capabilities and to draw accurate conclusions on the nature of precursor phenomenon under specific conditions. Yet the observation period and the data acquisition footprint will always limit the number of successful detections. Sinkholes are unpredictable (Gutiérrez, Cooper & Johnson 2008), and increasing the area and time monitored is necessary to increase the probability that a sinkhole will occur within the study period. This investigation relied on the in-depth analysis of a small number of events in a case-study based approach. The limitation of this approach is that conclusions can only be drawn from a small sample of successful detections, which has implications for drawing universally applicable conclusions. The variability of sinkholes in space and time and different geological conditions implies that the conclusions drawn should be considered only in the local context.

Accuracy assessment - A lack of detailed ground truth information imposed limitations to investigating reported sinkhole events and assessing DInSAR's detection accuracy. Comprehensive information regarding sinkholes in the inventory was often lacking, and in fact, only the dates of two out of the seven events were accurately reported. This was a limitation to investigating the ability of DInSAR to detect these events, as the research was unable to identify the exact cause of unsuccessful detections. Case studies of successful detections from DInSAR remain important to understanding the nature of precursory deformation and benefit future research. Sinkhole inventories should consider adding information relating to possible reports of precursory deformation. This will assist in distinguishing between subsidence prior to a sinkhole forming and general subsidence not leading to a cover-collapse sinkhole (Oosthuizen & Richardson 2011). Furthermore, information on the depth below the surface of the original cavity, the composition of the roof strata as well as the nature of the surface cover would add valuable information to support future investigations. Additionally, there is no obligation currently to report sinkhole events to the Council for Geoscience (Oosthuizen & van Rooy 2015). This results in many sinkholes going unrecorded and poses some challenges for assessing DInSAR's capabilities. Compulsory reporting, or similar policies, might lead to a more accurate database. On the other

hand, DInSAR provides an alternative wide-area monitoring tool that if implemented, can provide an independent recording of events. This recommendation echo's the call by (Richardson 2013) for accurate and thorough inventories to be taken in the future.

Accuracy assessments of detections were not quantitative due to the small scale of detections and their unpredictability. Visual inspection of basins could also only be performed months after they were detected due to data delivery latency and image processing times. More evidence of the basins might have been lost by this time. This is a universal challenge to sinkhole research (Vaccari et al. 2013) and only unique cases where sufficient evidence of a future sinkhole events happens to be available can be accurately assessed. On the other hand, DInSAR is seen as an operational tool and exhaustive accuracy assessments of its capability has been performed (Ferretti et al. 2007; Adam et al. 2009; Eineder et al. 2011; Quin & Loreaux 2013). DInSAR measurements can therefore generally be regarded as robust.

6.3 Recommendations for further research

Recommendations for further studies can be highlighted based on the findings of this research. Some precursory subsidence was successfully detected which paves the way for more investigations towards the ultimate aim of a sinkhole early warning system for the Gauteng area. Such investigations would need to focus on collecting a substantial database of DInSAR detections. Such a database will be useful, not only in complementing existing sinkhole and subsidence inventories as part of the National Dolomite Databank (Oosthuizen & van Rooy 2015), but also for a complete understanding of precursory deformation in Gauteng.

Optimal parameters - it is recommended that when determining the optimal parameters for SAR platform and data acquisition it is of foremost importance to not compromise on the spatial resolution of the SAR system. Detection of the most frequent events found in the study area will be impossible without sufficient spatial resolution. A spatial resolution in the order of one metre or less should provide the highest probability of detection. Such resolution is possible with the high resolution staring spotlight mode offered by SAR systems such as TerraSAR-X (Gernhardt et al. 2010). Such high-resolution data, however, compromises swath size and selecting the appropriate at-risk area to monitor will be critical. Historical sinkhole statistics (similar to those presented by Richardson (2013)) should be incorporated with current- and future land-use scenarios (Buttrick & Van Schalkwyk 1995) to identify these areas.

Temporal decorrelation - will remain a challenge for future studies. Sinkholes were only detected during periods of high global coherence. Yet, based on the successful detections, a global average coherence threshold of 0.4 can be regarded as the lower threshold of detection. This is a rough measure as it is based on a small sample and the fact that global coherence is only a proxy for local coherence. Nevertheless, it gives an indication of the coherence conditions needed for successful detections. Future studies should, therefore, consider more frequent revisit times as an

important acquisition parameter. Short temporal baselines minimise the chance that deformation will exceed the deformation gradient. It furthermore results in a higher temporal sampling of the deformation feature, as well as providing a more timely early warning of imminent sinkhole events. Most importantly however, short temporal baselines reduce decorrelation of the phase between image acquisitions.

SAR wavelength - Coherence challenges can also be addressed by using longer wavelengths that are less prone to temporal decorrelation. C-band and even L-band need to be considered for future studies, as long as the spatial resolution of the system is not reduced. Longer wavelengths, however, are less sensitive to very fine scale deformation. This may impose a limitation to detection, yet its importance remains unquantified and decorrelation noise is likely more important. A final note on coherence is the drastic effect of rainfall that was observed during this research. Rainfall imposed a major limitation to this investigation, yet remains outside the control of the researcher. Longer wavelength data is not expected to be more robust to rainfall events. Nevertheless, longer wavelengths are expected to be superior in the growing season, while shorter wavelengths offer superior detection probability under favourable coherence conditions.

However, considering these factors, it is noted that longer wavelengths should not be preferred if it is at the expense of lower spatial resolution using conventional DInSAR processing algorithms. This is due to the fundamental importance of spatial resolution. Detecting deformation smaller than approximately 10 x 10 pixels is difficult, if not impossible, (Massonnet & Feigl 1998), irrespective of coherence challenges. Minimising the chance of decorrelation and exceeding the deformation gradient through higher revisit times and longer wavelengths, should be considered only if sufficient spatial resolution is achieved.

Geometry - SAR LOS is a further consideration influencing DInSAR results as incidence angle controls spatial resolution to some extent. Moreover, low incidence angles present the real possibility of the subsidence signal being blocked by structures on the ground in the SAR's LOS. It is recommended that future studies collect data from descending and ascending satellite passes. Doing so will enable the observation of an area from the east and the west thereby mitigating LOS challenges as well as providing the opportunity to collect higher dimensional deformation observations.

SAR technology - Advances in SAR technology should be considered when designing a dolomite monitoring and early warning system. The current trend in SAR satellite design is towards constellations of many compatible SAR systems (Airbus Defence and Space 2014; Samsonov, Czarnogorska & Charbonneau 2016; Herbert 2016). This is an important direction for sinkhole research as temporal baselines are decreased while spatial coverage is increased (Milillo et al. 2015). Three future constellations, in particular, are important for sinkhole research: Sentinel 1, the RADARSAT Constellation Mission and Cosmo-SkyMed.

The launch of Sentinel 1a and b, under ESA's open access data policies, is an important development regarding early warning systems. Sentinel-1 has already proven to be capable of monitoring geohazards (Barra et al. 2016; Hickey et al. 2016). It has a potentially high revisit time of 6-days (using both, compatible, sensors). Furthermore, Sentinel-1's very large swath coverage and intermediate wavelength (C-band) are promising properties for sinkhole precursor detection. However, the spatial resolution of more than 10 m is likely to remain a fundamental limitation to the detection of frequent sinkhole precursors in the study area. The similar, C-band RADARSAT constellation mission will provide even higher temporal revisit times at potentially higher resolutions and should be considered in future research.

Advanced DInSAR - Considering the limitations imposed by spatial resolution and decorrelation effects, advanced time series stacking techniques such as SBAS and PSInSAR have been specifically designed to overcome coherence limitations typical to DInSAR (Crosetto et al. 2016). Testing these techniques in terms of future sinkhole early monitoring systems, particularly in relation to urban infrastructure stability monitoring, is recommended. However, all the techniques currently available are based on processing steps that potentially limits their suitability for the detection of sinkhole precursors. Small baseline techniques require spatial resampling to lower resolutions, which may not be suitable for sinkhole precursors on small sinkhole events. PSInSAR and related techniques are based on monitoring points that remain stable over the entire observation period. This strict requirement leads to a decrease in the potential observation density and thereby the chance of a successful detection, especially in areas characterised by distributed scatterers such as open fields (Prati, Ferretti & Perissin 2010). The application of advanced techniques will also rely on the existence of a multi-temporal stack of scenes for the area under investigation. The rapid revisit time provided by future SAR constellation missions will reduce the importance of this limitation (Airbus & Airbus Defence and Space 2014; Milillo et al. 2015; Samsonov, Czarnogorska & Charbonneau 2016). Furthermore, only linear, or known, deformation models can be detected, yet there is currently no reliable model for sinkhole precursors (Vaccari et al. 2013). All of these factors impose critical limitations to time series stacking techniques for an early warning system. It is thereby recommended that conventional DInSAR is employed in future studies, but it remains important to compare it to more advanced techniques.

6.4 Concluding remarks

Sinkhole events are low-probability but high-impact events and more evidence regarding precursors is needed not only locally, but also globally. This thesis showed that precursory deformation, if present, can be detected before sinkhole formation in Gauteng, yet limitations inherent to the SAR system still provide major challenges to reliable sinkhole early warning. It is expected, however, that SAR systems and processing techniques in the near future will outperform current systems. Many limitations identified in this study, spatial resolution and temporal coherence in particular (Moreira 2014), may be overcome in the near future.

The core contributions of this study to scientific knowledge are:

- Providing some of the first quantitate evidence of subsidence basins caused by sinkhole formation detected through DInSAR in the region. It is significant that the sinkholes were in dolomite (carbonate) terrain that is known to result in small-scale sinkholes. These are more challenging to detect than those in evaporite terrains.
- Establishing that DInSAR can detect deformation related to sinkholes of such a small magnitude that it may remain unnoticed and thereby unrecorded in sinkhole inventories.
- Identifying core limitations to X-band DInSAR sinkhole precursor detection in the region – the most important being spatial scale and factors relating to coherence. The physical presence of precursors was revealed as a fundamental limitation.

Sinkhole precursor detection has proven to be feasible by many authors, and it has now been successfully tested in the study area. The ability to detect sinkhole precursors has implications for hazard management policies in South Africa as it has been noted that current policies may be too restrictive. In part due to not factoring in engineering developments and recent successes in mitigation (Oosthuizen & van Rooy 2015). DInSAR provides a novel technique of proactive hazard mitigation not yet incorporated into current policies, particularly SANS 1936 (SABS 2012). Further research toward a more mature understanding of DInSAR's capabilities in a sinkhole early warning system may lead to its inclusion. An operational DInSAR based early warning system has the potential to enhance the exploitation of dolomite land in Gauteng. The findings from this and other studies combined with technological innovations are paving the way for a robust sinkhole detection and early warning system able to save lives and property in the near future.

[38 645 words]

References

Abelson M, Baer G, Shtivelman V, Wachs D, Raz E, Crouvi O, Kurzon I & Yechieli Y 2003. Collapse-sinkholes and radar interferometry reveal neotectonics concealed within the Dead Sea basin. *Geophysical Research Letters* 30, 10: 1–4.

Adam N, Parizzi A, Eineder M & Crosetto M 2009. Practical persistent scatterer processing validation in the course of the Terrafirma project. *Journal of Applied Geophysics* 69, 1: 59–65.

Airbus & Airbus Defence and Space 2014. TerraSAR-X Services Image Product Guide. *Technical document* , 2.0: 24.

Airbus Defence and Space 2014. TerraSAR-X / PAZ Constellation: Enhanced revist time and coverage. Promotional booklet [online]. Available from: www.intelligence-airbusds.com/en/5055-terrasar-x-paz-radar-satellite-constellation [Accessed 1 August 2016].

Alberga V 2004. Volume decorrelation resolution in polarimetric SAR interferometry. *IEEE Transactions on Geoscience and Remote Sensing* 42, 11: 2467–2478.

Alvarez-Salazar O, Hatch S, Rocca J, Rosen P, Shaffer S, Shen Y, Sweetser T & Xaypraseuth P 2014. *Mission design for NISAR repeat-pass interferometric SAR.* Proceedings of the International Society for Optics and Photonics Remote Sensing, Security and Defence conference held 22 - 25 September 2014, Amsterdam, Netherlands: 92410–92410.

Attema EPW, Duchossois G & Kohlhammer G 1998. *ERS-1/2 SAR land applications: overview and main results.* Proceedings of the IEEE International Geoscience and Remote Sensing Symposium held 6 - 10 July 1998, Seattle, United States of America: 1796–1798.

Augarde CE, Lyamin AV & Sloan SW 2003. Prediction of undrained sinkhole collapse. *Journal of Geotechnical and Geoenvironmnetal Engineering* 129: 197–205.

Avutia DJ 2014. Analytical and numerical study of dolomite sinkholes in Centurion, South Africa. Master's thesis. Cape Town: University of Cape Town, Department of Civil Engineering.

Baer G, Schattner U, Wachs D, Sandwell D, Wdowinski S & Frydman S 2002. The lowest place on Earth is subsiding—An InSAR (interferometric synthetic aperture radar) perspective. *Geological Society of America Bulletin* 114, 1: 12–23.

Balz T, Wei L, Jendryke M, Perissin D & Liao M 2012. *Tomosar and PS-InSAR analysis of high-rise buildings in Berlin.* Proceedings of the IEEE International Geoscience and Remote Sensing Symposium held 22 - 27 July 2012, Munich, Germany: 447–450.

Barra A, Monserrat O, Mazzanti P, Esposito C, Crosetto M & Scarascia Mugnozza G 2016. First insights on the potential of Sentinel-1 for landslides detection. *Geomatics, Natural Hazards and Risk* 5705: 1–10.

Batayneh AT, Abueladas AA & Moumani KA 2002. Use of ground-penetrating radar for assessment of potential sinkhole conditions: An example from Ghor al Haditha area, Jordan. *Environmental Geology* 41, 8: 977–983.

Battazza F & Ciappa A 2009. COSMO-SkyMed mission: a set of X-band SAR applications

conducted during 2008. *European Journal of Remote Sensing* 41, 3: 7–21.

Baumgartner S, Gabele M & Gebert N 2007. *Digital beamforming and traffic monitoring using the new F-SAR system of DLR.* Proceedings of International Radar Symposium held 5 - 7 September 2007, Köln, Germany: 1–5.

Bekaert DPS, Walters RJ, Wright TJ, Hooper AJ & Parker DJ 2015. Statistical comparison of InSAR tropospheric correction techniques. *Remote Sensing of Environment* 170: 40–47.

Berardino P, Mora O, Lanari R, Mallorqui JJ & Sansosti E 2002. A new algorithm for monitoring localized deformation phenomena based on small baseline differential SAR interferograms. *IEEE Transactions on Geoscience and Remote Sensing* 40, 11: 2375–2383.

Billi A, De Filippis L, Poncia PP, Sella P & Faccenna C 2016. Hidden sinkholes and karst cavities in the travertine plateau of a highly-populated geothermal seismic territory (Tivoli, central Italy). *Geomorphology* 255: 63–80.

Bonano M, Manunta M, Pepe A, Paglia L & Lanari R 2013. From previous C-band to new X-band SAR systems: Assessment of the DInSAR mapping improvement for deformation time-series retrieval in urban areas. *IEEE Transactions on Geoscience and Remote Sensing* 51, 4: 1973–1984.

Boncori JPM, Devoti R, Visini F, Carafa MMC, Pezzo G, Fornaro G, Berardino P, Atzori S, D'Amico V, Kastelic V, Meletti C, Pietrantonio G, Riguzzi F, Salvi S & Prieto DF 2015. *Mid-term review results of the ESA stse pathfinder charming project (constraining seismic hazard models with InSAR and GPS).* Proceedings of Fringe held 23-27 March 2015, Rome, Italy.

Bonforte A, Guglielmino F, Coltelli M, Ferretti A & Puglisi G 2011. Structural assessment of mount Etna volcano from permanent scatterers analysis. *Geochemistry, Geophysics, Geosystems* 12, 2: 1–19.

Bovenga F, Wasowski J, Nitti DO, Nutricato R & Chiaradia MT 2012. Using COSMO/SkyMed X-band and ENVISAT C-band SAR interferometry for landslides analysis. *Remote Sensing of Environment* 119: 272–285.

Bruckno B, Vaccari A, Hoppe E, Acton S, Campbell E, Bruckno BS, Vaccari A, Hoppe E, Acton ST & Campbell E 2015. *Integration and delivery of interferometric Synthetic Aperture Radar [InSAR] data into stormwater planning within karst terranes.* Proceedings of the Sinkhole Conference held 5-9 October 2015, Rochester, Minnesota: 371–380.

Bruckno B, Vaccari A, Hoppe E, Niemann W & Campbell E 2013. *Validation of Interferometric Synthetic Aperture Radar as a tool for identification of geohazards and at-risk transportation infrastructure.* Proceedings of the Highway Geology Symposium held 7-12 May 2013, Redding, United States of America: 1–19.

Buchoud E, Vrabie V, Mars JI, D'Urso G, Girard A, Blairon S & Hénault JM 2016. Quantification of submillimeter displacements by distributed optical fiber sensors. *IEEE Transactions on Instrumentation and Measurement* 65, 2: 413–422.

Bürgman R, Rosen PA & Fielding EJ 2000. Synthetic Aperture Radar Interferometry to measure

Earth's surface topography and its deformation. *Annual Review of Earth and Planetary Science* 28: 169–209.

Buttrick DB, Trollip NYG, Watermeyer RB, Pieterse ND & Gerber AA 2011. A performance based approach to dolomite risk management. *Environmental Earth Sciences* 64, 4: 1127–1138.

Buttrick DB & Van Schalkwyk A 1995. The method of scenario supposition for stability evaluation of sites on dolomitic land in South Africa, technical paper. *Journal of the South African Institution of Civil Engineers* 37, 4: 9–14.

Buttrick DB, Van Schalkwyk A, Kleywegt RJ & Watermeyer RB 2001. Proposed method for dolomite land hazard and risk assessment in South Africa. *Journal of the South African Institution of civil engineering* 43, 2: 27–36.

Calo F, Fornaro G, Parise M & Zeni G 2011. *The SBAS-DINSAR approach for the spatial and temporal analysis of sinkhole phenomena.* Proceedings of Fringe held 19-23 September 2011, Frascati, Italy: s.p.

Carbonel D, Rodríguez V, Gutiérrez F, Mccalpin JP, Linares R, Roqué C, Zarroca M, Guerrero J & Sasowsky I 2013. Evaluation of trenching, ground penetrating radar (GPR) and electrical resistivity tomography (ERT) for sinkhole characterization. *Earth Surface Processes and Landforms* 39, 2: 214–227.

Castañeda C, Gutiérrez F, Manunta M & Galve JP 2009. DInSAR measurements of ground deformation by sinkholes, mining subsidence, and landslides, Ebro River, Spain. *Earth Surface Processes and Landforms* 34, 11: 1562–1574.

Chang L & Hanssen RF 2014. Detection of cavity migration and sinkhole risk using radar interferometric time series. *Remote Sensing of Environment* 147: 56–64.

Chang W, Tan S, Lemmetyinen J, Tsang L, Xu X & Yueh SH 2014. Dense media radiative transfer applied to SnowScat and SnowSAR. *IEEE Journal of Selected Topics in Applied Earth Observations and Remote Sensing* 7, 9: 3811–3825.

Cigna F, Osmanoğlu B, Cabral-Cano E, Dixon TH, Ávila-Olivera JA, Garduño-Monroy VH, DeMets C & Wdowinski S 2012. Monitoring land subsidence and its induced geological hazard with Synthetic Aperture Radar Interferometry: A case study in Morelia, Mexico. *Remote Sensing of Environment* 117: 146–161.

Clapuyt F, Vanacker V & Van Oost K 2015. Reproducibility of UAV-based earth topography reconstructions based on Structure-from-Motion algorithms. *Geomorphology* 260: 4–15.

Clark S 2016. With Russian launch grounded, Iridium flips order of satellite deployments. Spaceflight Now [online]. Available from: https://spaceflightnow.com/2016/02/29/with-russian-launch-grounded-iridium-flips-order-of-satellite-deployments/ [Accessed 1 August 2016].

Closson D, Karaki NA, Hansen H, Derauw D, Barbier C & Ozer A 2003. Space-borne radar interferometric mapping of precursory deformations of a dyke collapse, Dead Sea area, Jordan. *International Journal of Remote Sensing* 24, 4: 843–849.

Closson D, Karaki NA, Klinger Y, Hussein MJ & Husse 2005. Subsidence and sinkhole hazard

assessment in the Southern Dead Sea area, Jordan. *Pure and Applied Geophysics* 162, 2: 221–248.

Closson D, Karaki NA, Milisavljevic N, Hallot F & Acheroy M 2010. Salt-dissolution-induced subsidence in the Dead Sea area detected by applying interferometric techniques to ALOS Palsar Synthetic Aperture Radar images. *Geodinamica Acta* 23, 1–3: 65–78.

Colesanti C, Mouelic SL, Bennani M, Raucoules D, Carnec C & Ferretti A 2005. Detection of mining related ground instabilities using the Permanent Scatterers technique—a case study in the east of France. *International Journal of Remote Sensing* 26, 1: 201–207.

Conway B & Cook J 2013. *Monitoring evaporite karst activity and land subsidence in the Holbrook Basin, Arizona using interferometric synthetic aperture radar (InSAR).* Proceedings of the Sinkhole Conference held 5-10 May 2013, Carlsbad, United States of America: 187–194.

Crosetto M, Arnaud A & Duro J 2003. *Deformation monitoring using remotely sensed radar Interferometric data.* Proceedings of the Federation of Surveyors Symposium on Deformation Measurements held 25-28 May 2003, Santorini, Greece: 1–8.

Crosetto M, Biescas E, Duro J, Closa J & Arnaud A 2008. Generation of advanced ERS and Envisat Interferometric SAR products using the Stable Point Network technique. *Photogrammetric Engineering & Remote Sensing* 74, 4: 443–450.

Crosetto M, Gili JA, Monserrat O, Cuevas-González M, Corominas J & Serral D 2013. Interferometric SAR monitoring of the Vallcebre landslide (Spain) using corner reflectors. *Natural Hazards and Earth System Science* 13, 4: 923–933.

Crosetto M, Monserrat O & Crippa B 2010. *Persistent scatterer interferometry: Potentials and limits.* Proceedings of the International Society for Photogrammetry and Remote Sensing Congress held 15-18 June 2010, Alberta, Canada.

Crosetto M, Monserrat O, Cuevas-González M, Devanthéry N & Crippa B 2016. Persistent Scatterer Interferometry: a review. *ISPRS Journal of Photogrammetry and Remote Sensing* 115: 78–89.

Crosetto M, Monserrat O, Luzi G, Cuevas-González M & Devanthéry N 2014. Discontinuous GBSAR deformation monitoring. *ISPRS Journal of Photogrammetry and Remote Sensing* 93: 136–141.

Das P & Mohanty PR 2016. Resistivity imaging technique to delineate shallow subsurface cavities associated with old coal working: a numerical study. *Environmental Earth Sciences* 75, 8: 661–673.

Day PW 2011. *Managing poorly quantified risks by means of national standards with specific reference to dolomitic ground.* Proceedings of the International Symposium on Geotechnical Safety and Risk held 2-3 June 2011, Munich, Germany: 269–274.

Day PW 2012. SANS 1946 and related standards. Development on dolomite land. Presentation. Jones & Wagener consultants [online]. Available from: https://www.sabs.co.za/presentations/docs/Peter_Day_Dolomite_Standards SABS

Convention 2012.pdf [Accessed 1 August 2016].

De Waele J, Gutiérrez F, Parise M & Plan L 2011. Geomorphology and natural hazards in karst areas: A review. *Geomorphology* 134, 1–2: 1–8.

Dehghani M 2016. Landslide monitoring using hybrid conventional and Persistent Scatterer Interferometry. *Journal of the Indian Society of Remote Sensing* 44: 1–9.

Del Ventisette C, Ciampalini A, Manunta M, Calo F, Paglia L, Ardizzone F, Mondini AC, Reichenbach P, Mateos RM, Bianchini S, Garcia I, Fusi B, Deak ZV, Radi K, Graniczny M, Kowalski Z, Piatkowska A, Przylucka M, Retzo H, Strozzi T, Colombo D, Mora O, Sanchez F, Herrera G, Moretti S, Casagli N & Guzzetti F 2013. Exploitation of large archives of ERS and ENVISAT C-band SAR data to characterize ground deformations. *Remote Sensing* 5, 8: 3896–3917.

Diop S, Forbes C & Chiliza GS 2010. Landslide inventorization and susceptibility mapping in South Africa. *Landslides* 7, 2: 207–210.

Dou J, Li X, Yunus AP, Paudel U, Chang KT, Zhu Z & Pourghasemi HR 2015. Automatic detection of sinkhole collapses at finer resolutions using a multi-component remote sensing approach. *Natural Hazards* 78, 2: 1021–1044.

Doyle GS 2000. Three applications of satellite-borne repeat pass SAR interferometry in southern Africa. Master's thesis. Cape Town: University of Cape Town, Department of Electrical Engineering.

Doyle GS, Inggs MR & Hartnady CJH 1997. *The use of interferometric SAR in a study of reservoir induced crustal deformation.* Proceedings of the South African Symposium on Communications and Signal Processing held 9-10 September 1997, Grahamstown, South Africa.

Doyle GS, Stow RJ & Inggs MR 2001. *Satellite radar interferometry reveals mining induced seismic deformation in South Africa.* Proceedings of the IEEE International Geoscience and Remote Sensing Symposium held 9-13 July 2001, Sydney, Australia: 7031–7033.

Doyle GS, Wilkinson AJ & Inggs MR 1999. *Contending with high relief and temporal decorrelation in an InSAR study of the effects of reservoir loading.* Proceedings of the IEEE International Geoscience and Remote Sensing Symposium held 28 June-2 July 1999, Hamburg, Germany: 476–478.

E-GEOS 2010. Cosmo-skymed: The first radar constellation for operational applications and services. Product sheet [online]. Available from: http://www.e-geos.it/products/pdf/e-GEOS_COSMO-SkyMed.pdf [Accessed 1 August 2016].

Eineder M, Hajnsek I, Krieger G, Moreira A & Papathanassiou K 2014. Tandem-L: satellite mission proposal for monitoring dynamic processes on the Earth's surface. German Aerospace Center (DLR) [online]. Available from: http://www.dlr.de/hr/en/desktopdefault.aspx/tabid-8113/14171_read-35837/ [Accessed 1 August 2016].

Eineder M, Minet C, Steigenberger P, Cong X & Fritz T 2011. Imaging geodesy - Toward

centimeter-level ranging accuracy with TerraSAR-X. *IEEE Transactions on Geoscience and Remote Sensing* 49, 2: 661–671.

Engelbrecht J 2013. Parameters affecting interferometric coherence and implications for long-term operational monitoring of mining-induced surface deformation. Doctoral dissertation. Cape Town: University of Cape Town, Department of Electrical Engineering.

Engelbrecht J & Inggs MR 2016. Coherence optimisation and its limitations for deformation monitoring in agricultural regions. *IEEE Journal of Selected Topics in Applied Earth Observations and Remote Sensing* , 99: 1–8.

Engelbrecht J & Inggs MR 2011. *Detection and monitoring of surface subsidence associated with mining activities in the Witbank coalfields, South Africa, using differential radar interferometry.* Proceedings of the IEEE International Geoscience and Remote Sensing Symposium held 24-29 July 2011, Vancouver, Canada: 1596–1599.

Engelbrecht J & Inggs MR 2013. Differential Interferometry techniques on L-Band data employed for the monitoring of surface subsidence due to mining. *South African Journal of Geomatics* 2, 2: 82–93.

Engelbrecht J, Musekiwa C, Kemp J & Inggs MR 2014. Parameters affecting interferometric coherence-the case of a dynamic agricultural region. *IEEE Transactions on Geoscience and Remote Sensing* 52, 3: 1572–1582.

ESA 1998. ENVISAT-1 Mission and system summary. Brochure [online]. Available from: https://earth.esa.int/support-docs/pdf/mis_sys.pdf [Accessed 1 August 2016].

Ferretti A, Colombo D, Fumagalli A, Novali F & Rucci A 2015. InSAR data for monitoring land subsidence: time to think big. *Proceedings of the International Association of Hydrological Sciences* 372: 331–334.

Ferretti A, Fumagalli A, Novali F, Prati C, Rocca F & Rucci A 2011. A new algorithm for processing interferometric data-stacks: SqueeSAR. *IEEE Transactions on Geoscience and Remote Sensing* 49, 9: 3460–3470.

Ferretti A, Monti-guarnieri A, Prati C & Rocca F 2007. InSAR principles: Guidelines for SAR Interferometry processing and interpretation. ESA Publications. Available from: http://www.esa.int/About_Us/ESA_Publications [Accessed 1 August 2016].

Ferretti A, Perissin D, Prati C & Rocca F 2005. *On the physical nature of SAR Permanent Scatterers.* Proceedings of the URSI Commission F Symposium on Microwave Remote Sensing of the Earth, Oceans, Ice, and Atmosphere held 20-21 April 2005, Ispra, Italy: 1–6.

Ferretti A, Prati C & Rocca F 2000. Nonlinear subsidence rate estimation using permanent scatterers indifferential SAR interferometry. *IEEE Transactions on Geoscience and Remote Sensing* 38, 5: 2202–2212.

Ferretti A, Prati C & Rocca F 2001. Permanent Scatterers in SAR Interferometry. *IEEE Transactions on Geoscience and Remote Sensing* 39, 1: 8–20.

Ferretti A, Savio G, Barzaghi R, Borghi A, Musazzi S, Novali F, Prati C & Rocca F 2007.

Submillimeter accuracy of InSAR time series: Experimental validation. *IEEE Transactions on Geoscience and Remote Sensing* 45, 5: 1142–1153.

Ferretti A, Tamburini A, Novali F, Fumagalli A, Falorni G & Rucci A 2011. Impact of high resolution radar imagery on reservoir monitoring. *Energy Procedia* 4: 3465–3471.

FEWSNET 2016. Illustrating the extent and severity of the 2015 - 16 drought. *Famine Early Warning Systems Network/USAID Southern Africa Special Report*: 1–8.

Filin S, Avni Y, Baruch A, Morik S, Arav R & Marco S 2014. Characterization of land degradation along the receding Dead Sea coastal zone using airborne laser scanning. *Geomorphology* 206: 403–420.

Fornaro G, Lombardini F, Pauciullo A, Reale D & Viviani F 2014. Tomographic processing of Interferometric SAR Data: developments, applications, and future research perspectives. *Signal Processing Magazine, IEEE* 31, 4: 41–50.

Fornaro G, Reale D & Verde S 2013. Bridge thermal dilation monitoring with millimeter sensitivity via multidimensional SAR imaging. *IEEE Geoscience and Remote Sensing Letters* 10, 4: 677–681.

Fornaro G, Verde S, Reale D & Pauciullo A 2015. CAESAR: an approach based on covariance matrix decomposition to improve multibaseline-multitemporal interferometric SAR processing. *Geoscience and Remote Sensing, IEEE Transactions on* 53, 4: 2050–2065.

Galve JP, Castañeda C & Gutiérrez F 2015. Railway deformation detected by DInSAR over active sinkholes in the Ebro Valley evaporite karst, Spain. *Natural Hazards and Earth System Sciences* 15, 11: 2439–2448.

Galve JP, Gutiérrez F, Cendrero A, Remondo J, Bonachea J, Guerrero J & Lucha P 2009. Predicting sinkholes by means of probabilistic models. *Quarterly Journal of Engineering Geology and Hydrogeology* 42: 139–144.

Galve JP, Gutiérrez F, Remondo J, Bonachea J, Lucha P & Cendrero A 2009. Evaluating and comparing methods of sinkhole susceptibility mapping in the Ebro Valley evaporite karst (NE Spain). *Geomorphology* 111, 3–4: 160–172.

Gamma Remote Sensing 2011. GAMMA V1.8. Interferometric SAR, Differential Interferometry and Geocoding Software User's guide [confidential]

Gebert N, Domínguez BC, Davidson MWJ, Martin MD & Silvestrin P 2014. *SAOCOM-CS – A passive companion to SAOCOM for single-pass L-band SAR interferometry.* Proceedings of European Conference on Synthetic Aperture Radar held 3-6 June 2014, Berlin, Germany: 1251–1254.

Gernhardt S, Adam N, Eineder M & Bamler R 2010. Potential of very high resolution SAR for persistent scatterer interferometry in urban areas. *Annals of GIS* 16, 2: 103–111.

Goldstein RM & Werner CL 1998. Radar interferogram filtering for geophysical applications. *Geophysical Research Letters* 25, 21: 4035.

Gomba G, Parizzi A, De Zan F, Eineder M, Bamler R, Zan FD, Eineder M, Member S & Bamler R

2016. Toward operational compensation of ionospheric effects in SAR interferograms: The split-spectrum method. *IEEE Transactions on Geoscience and Remote Sensing* 54, 3: 1446–1461.

Gong W, Thiele A, Hinz S, Meyer F, Hooper A & Agram P 2016. Comparison of small baseline Interferometric SAR processors for estimating ground deformation. *Remote Sensing* 8, 4: 330.

Greif V & Vlcko J 2013. Application of the PS-InSAR technique for the post-failure landslide deformation monitoring at Lubietova site in central Slovakia. *Landslide Science and Practice* 2.

Guerrero J, Gutiérrez F, Bonachea J & Lucha P 2008. A sinkhole susceptibility zonation based on paleokarst analysis along a stretch of the Madrid – Barcelona high-speed railway built over gypsum- and salt-bearing evaporites (NE Spain). *Engineering Geology* 102, 1–2: 62–73.

Gutiérrez F, Cooper AH & Johnson KS 2008. Identification, prediction, and mitigation of sinkhole hazards in evaporite karst areas. *Environmental Geology* 53, 5: 1007–1022.

Gutiérrez F, Galve JP, Lucha P, Castañeda C, Bonachea J & Guerrero J 2011. Integrating geomorphological mapping, trenching, InSAR and GPR for the identification and characterization of sinkholes: A review and application in the mantled evaporite karst of the Ebro Valley (NE Spain). *Geomorphology* 134, 1–2: 144–156.

Gutiérrez F, Guerrero J & Lucha P 2008. Quantitative sinkhole hazard assessment. A case study from the Ebro Valley evaporite alluvial karst (NE Spain). *Natural Hazards* 45, 2: 211–233.

Gutiérrez F, Parise M, Waele JD & Jourde H 2014. A review on natural and human-induced geohazards and impacts in karst. *Earth-Science Reviews* 138: 61–88.

Hanssen RF 2001. *Radar Interferometry - data interpretation and error analysis*. Berlin: Springer Science & Business Media.

Herbert JK 2016. COSMO-SkyMed second generation. EO Portal Directory [online]. Available from: https://directory.eoportal.org/web/eoportal/satellite-missions/c-missions/cosmo-skymed-second-generation [Accessed 1 August 2016].

Hickey J, Biggs J, Ebmeier S & Parker A 2016. Integrating ALOS-2 and Sentinel-1 InSAR data for systematic volcano deformation monitoring. *Geophysical Research Abstracts* 18: 16706.

Hooper A & Zebker HA 2007. Phase unwrapping in three dimensions with application to InSAR time series. *Journal of the Optical Society of America* 24, 9: 2737–2747.

Hooper A, Zebker H, Segall P & Kampes B 2004. A new method for measuring deformation on volcanoes and other natural terrains using InSAR persistent scatterers. *Geophysical Research Letters* 31: 1–5.

Hung WC, Hwang C, Chen YA, Chang CP, Yen JY, Hooper A & Yang CY 2011. Surface deformation from persistent scatterers SAR interferometry and fusion with leveling data: A case study over the Choushui River Alluvial Fan, Taiwan. *Remote Sensing of Environment* 115, 4: 957–967.

Intrieri E, Gigli G, Nocentini M, Lombardi L, Mugnai F, Fidolini F & Casagli N 2015. Sinkhole

monitoring and early warning: An experimental and successful GB-InSAR application. *Geomorphology* 241: 304–314.

Jaros MB, James GM & Gewanlal C 2009. *Multi-layer geosynthetic reinforced embankment over potential sinkholes for a rapid rail link in South Africa.* Proceedings of GIGSA GeoAfrica conference held 2-5 September 2009, Cape Town, South Africa: 1–7.

Jia H & Liu L 2016. A technical review on persistent scatterer interferometry. *Journal of Modern Transportation* 24: 1–6.

Jiang M, Li ZW, Ding XL, Zhu JJ & Feng GC 2011. Modeling minimum and maximum detectable deformation gradients of interferometric SAR measurements. *International Journal of Applied Earth Observation and Geoinformation* 13, 5: 766–777.

Jones CE & Blom RG 2013. Bayou Corne, Louisiana, sinkhole: Precursory deformation measured by radar interferometry. *Geology* 42, 2: 111–114.

Jones CE & Blom RG 2015. *Pre-event and post-formation ground movement associated with the Bayou Corne sinkhole.* Proceedings of the Sinkhole Conference held 5-9 October 2015, Rochester, Minnesota: 415–422.

Joyce KE, Belliss SE, Sergey V, McNeill SJ, Glassey PJ, Samsonov SV, McNeill SJ & Glassey PJ 2009. A review of the status of satellite remote sensing and image processing techniques for mapping natural hazards and disasters. *Progress in Physical Geography* 33, 2: 183–207.

Joyce KE, Samsonov S, Levick SR, Engelbrecht J & Belliss S 2014. Mapping and monitoring geological hazards using optical, LiDAR, and synthetic aperture RADAR image data. *Natural Hazards* 73, 2: 137–163.

Kankaku Y, Sagisaka M & Suzuki S 2014. *PALSAR-2 launch and early orbit status.* Proceedings of the IEEE International Geoscience and Remote Sensing Symposium held 13-18 July 2014, Québec, Canada: 3410–3412.

Katsaros KB & Brown RA 1991. Legacy of Seasat mission for studies of the atmosphere and air-sea-ice interactions. *Bulletin of the American Meteorological societyociety* 72, 7: 967–980.

Kaufmann O & Quinif Y 2002. Geohazard map of cover-collapse sinkholes in the “Tournaisis” area, southern Belgium. *Engineering Geology* 65: 117–124.

Kemp J 2011. The application of multi-source remote sensing for sediment transport mapping in an intertropical context (La Réunion Island and South Africa). Doctoral Dissertation. Saint-Denis: University of La Réunion, Faculty of Science and Technology.

Kemp J & Burns J 2016. *Agricultural monitoring using pursuit monostatic TanDEM-X coherence in the Western Cape , South Africa.* Proceedings of the European Conference on Synthetic Aperture Radar held 6-9 June 2014, Hamburg, Germany: 643–646.

Kim J-W, Lu Z & Degrandpre K 2016. Ongoing Deformation of Sinkholes in Wink, Texas, Observed by Time-Series Sentinel-1A SAR Interferometry (Preliminary Results). *Remote Sensing* 8, 4: 313.

Klein E, Contrucci I, Daupley X, Hernandez O, Nadim C, Cauvin L, Pirson M, Klein E, Contrucci I,

Daupley X, Hernandez O & Bigarre P 2008. *Evolution monitoring of a solution-mining cavern in salt : identifying and analysing early-warning signals prior to collapse.* Proceedings of the Solution Mining Research Institute's Technical Conference held 5-9 October 2008, Austin, United States of America: 2–12.

Krieger G, Zink M, Bachmann M, Bräutigam B, Schulze D, Martone M, Rizzoli P, Steinbrecher U, Walter Antony J, De Zan F, Hajnsek I, Papathanassiou K, Kugler F, Rodriguez Cassola M, Younis M, Baumgartner S, López-Dekker P, Prats P & Moreira A 2013. TanDEM-X: A radar interferometer with two formation-flying satellites. *Acta Astronautica* 89: 83–98.

Kruger C 2015. Massive sinkhole in Laudium. Rekord Centurion [online]. Available from: http://rekordcenturion.co.za/70476/massive-sinkhole-in-laudium/ [Accessed 1 August 2016].

Larry D. Seale J 2005. Creation, analysis, and evaluation of remote sensing sinkhole databases for Florida. Master's thesis. Tampa: University of South Florida, Department of geology.

Leblanc A, Short N, Mathon-dufour V, Tremblay T & Oldenborger GA 2015. *DInSAR seasonal surface displacement in built and natural permafrost environments, Iqaluit, Canada.* Proceedings of the Canadian Permafrost Conference held 20 - 23 September 2015, Québec city, Canada: 1–6.

Lee EJ, Shin S, Ko BC & Chang C 2016. Early Sinkhole Detection using a Drone-based Thermal Camera and Image Processing. *Infrared Physics & Technology*.

Lee JS, Grunes MR & Pottier E 2001. Quantitative comparison of classification capability: Fully polarimetric versus dual and single-polarization SAR. *IEEE Transactions on Geoscience and Remote Sensing* 39, 11: 2343–2351.

Leprince S, Barbot S, Ayoub F & Avouac JP 2007. Automatic and precise orthorectification, coregistration, and subpixel correlation of satellite images, application to ground deformation measurements. *IEEE Transactions on Geoscience and Remote Sensing* 45, 6: 1529–1558.

Manunta M, Calo F, Paglia L, Bonano M & Lanari R 2011. *DORIS FP7-EU project : exploitation of 20 years DInSAR data archive for landslide monitoring.* Proceedings of Fringe held 19-23 September 2011, Frascati, Italy: 19–23.

Marinkovic P, Ketelaar G & Hanssen RF 2004. *A controlled ENVISAT/ERS persistent scatterer experiment, Iiplications of corner reflector monitoring.* Proceedings of the CEOS SAR workshop held 27-28 May 2004, Ulm, Germany: 1–8.

Massonnet D & Feigl KL 1998. Radar interferometry and its application to changes in the Earth's surface. *Reviews of Geophysics* 36, 4: 441.

Massonnet D, Rossi M, Carmona C, Adragna F, Peltzer G, Feigl K & Rabaute T 1993. The displacement field of the Landers earthquake mapped by radar interferometry. *Nature* 364, 6433: 138–142.

MDA 2014. *RADARSAT-2 Product Description.* Official : 1–39.

Meraka 2016. Wide Area Monitoring System. MODIS time series viewer [online]. Available from: http://wamis.meraka.org.za/time-series-viewer [Accessed 1 August 2016].

Meta A, Imbembo E, Trampuz C, Coccia A & De Luca G 2012. *A selection of meta sensing airborne campaigns at L-, X- and Ku-band.* Proceedings of the IEEE International Geoscience and Remote Sensing Symposium held 22 - 25 September 2014, Amsterdam, Netherlands: IEEE: 4571–4574.

Milillo P, Riel B, Minchew B, Yun SH, Simons M & Lundgren P 2015. On the synergistic use of SAR constellations' data exploitation for Earth science and natural hazard response. *IEEE Journal of Selected Topics in Applied Earth Observations and Remote Sensing* 9, 3: 1095–1100.

Minh HTD, Tebaldini S, Rocca F, Le Toan T, Villard L & Dubois-Fernandez PC 2015. Capabilities of BIOMASS tomography for investigating tropical forests. *IEEE Transactions on Geoscience and Remote Sensing* 53, 2: 965–975.

Momubaghan GA 2012. Geotechnical investigations for the Gautrain mass transit rapid link over dolomite bedrock in the Centurion area. Master's thesis. Pretoria: University of Pretoria, Department of Geology.

Moreira A 2014. *A golden age for spaceborne SAR system.* Proceedings of the International Conference on Microwaves, Radar, and Wireless Communication held 16-18 June 2014, Gdańsk, Poland: 1–4.

Moreira A, Prats-iraola P, Younis M, Krieger G, Hajnsek I & Papathanassiou KP 2013. A Tutorial on Synthetic Aperture Radar. *IEEE Geoscience and Remote Sensing Magazine*: 6–43.

Nannini M, Iraola PP, Scheiber R, Yague N & German M 2014. *Sentinel-1 mission : results of the InSARap project.* Proceedings of European Conference on Synthetic Aperture Radar held 6-9 June 2014, Hamburg, Germany: 5–8.

Nemoto Y, Nishino H, Ono M, Mizutamari H, Nishikawa K & Tanaka K 1991. Japanese Earth Resources Satellite-1 Synthetic Aperture Radar. *Proceedings of the IEEE* 79, 6: 800–809.

Neumann M, Ferro-Famil L & Reigber A 2008. Multibaseline polarimetric SAR interferometry coherence optimization. *IEEE Geoscience and Remote Sensing Letters* 5, 1: 93–97.

Neumann M, Nguyen Q, Rosen PA, Shimada J, Simard M & Tung W 2016. NASADEM global elevation model: methods and progress. *The International Archives of the Photogrammetry, Remote Sensing and Spatial Information Sciences* XLI-B4: 125–128.

Nof RN, Baer G, Ziv A, Raz E, Atzori S & Salvi S 2013. Sinkhole precursors along the Dead Sea, Israel, revealed by SAR interferometry. *Geology* 4, 9: 1019–1022.

Nof RN, Ziv A, Doin MP, Baer G, Fialko Y, Wdowinski S, Eyal Y & Bock Y 2012. Rising of the lowest place on Earth due to Dead Sea water-level drop: Evidence from SAR interferometry and GPS. *Journal of Geophysical Research: Solid Earth* 117, 5: 1–16.

Oosthuizen AC & Richardson S 2011. Sinkholes and subsidence in South Africa. *Council for Geoscience Report (number 2011-0010)*: 1–31.

Oosthuizen AC & van Rooy JL 2015. Hazard of sinkhole formation in the Centurion CBD using the Simplified Method of Scenario Supposition. *Journal of the South African Institution of civil*

engineering 57, 2: 69–75.

Osmanoğlu B, Sunar F, Wdowinski S & Cabral-Cano E 2015. Time series analysis of InSAR data: Methods and trends. *ISPRS Journal of Photogrammetry and Remote Sensing* 115: 90–102.

Ozden A, Faghri A, Li M & Tabrizi K 2016. Evaluation of Synthetic Aperture Radar satellite remote sensing for pavement and infrastructure monitoring. *Procedia Engineering* 145: 752–759.

Paine JG, Buckley SM, Collins EW & Wilson CR 2012. Assessing collapse risk in evaporite sinkhole-prone areas using microgravimetry and Radar Interferometry. *Journal of Environmental & Engineering Geophysics* 17, 2: 75–87.

Palubinskas G, Meyer F, Runge H, Reinartz P, Scheiber R & Bamler R 2005. *Estimation of along-track velocity of road vehicles in SAR data.* Proceedings of the International Society for Optics and Photonics conference held 19 September 2005, Bruges, Belgium: 1–9.

Papathanassiou KP & Cloude SR 2001. Single-baseline polarimetric SAR interferometry. *IEEE Transactions on Geoscience and Remote Sensing* 39, 11: 2352–2363.

Parise M 2015. A procedure for evaluating the susceptibility to natural and anthropogenic sinkholes. *Georisk: Assessment and Management of Risk for Engineered Systems and Geohazards* 9, 4: 1–14.

Parise M & Lollino P 2011. A preliminary analysis of failure mechanisms in karst and man-made underground caves in Southern Italy. *Geomorphology* 134, 1–2: 132–143.

Peltier A, Bianchi M, Kaminski E, Komorowski JC, Rucci A & Staudacher T 2010. PSInSAR as a new tool to monitor pre-eruptive volcano ground deformation: Validation using GPS measurements on Piton de La Fournaise. *Geophysical Research Letters* 37, 12: 1–5.

Pitz W & Miller D 2010. The TerraSAR-X satellite. *IEEE Transactions on Geoscience and Remote Sensing* 48, 2: 615–622.

Potgieter AS, Pretorius SJ & Walt IJVD 2016. Integration of a dolomite risk management programme in local governance in South Africa : Tlokwe City Council. *Journal of Environmental Protection* 7: 1041–1049.

Prati C, Ferretti A & Perissin D 2010. Recent advances on surface ground deformation measurement by means of repeated space-borne SAR observations. *Journal of Geodynamics* 49, 3–4: 161–170.

Prats-Iraola P, Nannini M, Scheiber R, De Zan F, Wollstadt S, Minati F, Costantini M, Bucarelli A, Borgstromc S & Walter T 2015. *Investigations with the sentinel-1 interferometric wide swath mode.* Proceedings of Fringe held 23-27 March 2015, Rome, Italy: 3–4.

Prats-Iraola P, Nannini M, Scheiber R, De Zan F, Wollstadt S, Minati F, Vecchioli F, Costantini M, Borgstrom S, De Martino P, Siniscalchi V, Walter T, Foumelis M & Desnos Y-L 2015. *Sentinel-1 assessment of the interferometric wide-swath mode.* Proceedings of the IEEE International Geoscience and Remote Sensing Symposium held 26-31 July 2015, Milan, Italy: 5247–5251.

Przylucka M, Herrera G, Graniczny M, Colombo D & Béjar-Pizarro M 2015. Combination of

conventional and advanced DInSAR to monitor very fast mining subsidence with TerraSAR-X data: Bytom City (Poland). *Remote Sensing* 7, 5: 5300–5328.

Quin G & Loreaux P 2013. Submillimeter accuracy of multipass corner reflector monitoring by PS technique. *IEEE Transactions on Geoscience and Remote Sensing* 51, 3: 1775–1783.

Raucoules D, Bourgine B, de Michele M, Le Cozannet G, Closset L, Bremmer C, Veldkamp H, Tragheim D, Bateson L, Crosetto M, Agudo M & Engdahl M 2009. Validation and intercomparison of Persistent Scatterers Interferometry: PSIC4 project results. *Journal of Applied Geophysics* 68, 3: 335–347.

Richards NP & Brynard HJ 2006. *The development of a national geohazards programme for South Africa : Why , how and when ?.* Proceedings of the International Association for Engineering Geology Congress held 6-10 September 2006, Nottingham, United Kingdom: 1–6.

Richardson S 2013. Sinkhole and subsidence record in the chuniespoort group dolomite , Gauteng , South Africa. Master's thesis. Pretoria: University of Pretoria, Department of Geology.

Rosenqvist A, Shimada M, Ito N & Watanabe M 2007. ALOS PALSAR: A pathfinder mission for global-scale monitoring of the environment. *IEEE Transactions on Geoscience and Remote Sensing* 45, 11: 3307–3316.

Roth A, Huber M & Kosmann D 2004. *Geocoding of TerraSAR-X data.* Proceedings of the International Society for Photogrammetry and Remote Sensing Congress held 12–19 July 2004, Istanbul, Turkey: 840–844.

Roux JJL, Newby TS, Sumner PD, Le Roux JJ, Newby TS & Sumner PD 2007. Monitoring soil erosion in South Africa at a regional scale : review and recommendations. *South African Journal of Science* 103: 329–335.

Rucker ML, Hulburt S & Edwards MD 2013. *Reconnaissance evaluation of a potential future sinkhole using integrated simple surface geophysics and surface monitoring points.* Proceedings of the Sinkhole Conference held 5-10 May 2013, Carlsbad, United States of America: 221–230.

Rucker ML, Panda BB, Meyers RA & Lommler JC 2013. Using InSAR to detect subsidence at brine wells, sinkhole sites, and mines. *Carbonates and Evaporites* 28: 141–147.

SABS 2012. *Development of dolomite land - Part 4 : Risk management.* South African National Standard 1936-4:2012 Edition 1. Pretoria: South African Bureau of Standards: 64–73.

Samsonov S, Czarnogorska M & Charbonneau F 2016. *RADARSAT constellation mission for monitoring ground deformation in Alberta's oil sands.* Proceedings of the IEEE Annual Wireless and Microwave Technology Conference held 17 March 2016, Clearwater Beach, United States of America: 1–4.

Samsonov S & D'Oreye N 2012. Multidimensional time-series analysis of ground deformation from multiple InSAR data sets applied to Virunga Volcanic Province. *Geophysical Journal International* 191: 1095–1108.

Samsonov S, D'Oreye N & Smets B 2013. *Natural and anthropogenic ground deformation*

monitored using high spatio-temporal resolution MSBAS time series method. Proceedings of the International Workshop on the Analysis of Multi-Temporal Remote Sensing Images held 25-27 June 2013, Banff, Canada: n.p.

Sansosti E, Berardino P, Bonano M, Calò F, Castaldo R, Casu F, Manunta M, Manzo M, Pepe A, Pepe S, Solaro G, Tizzani P, Zeni G & Lanari R 2014. How second generation SAR systems are impacting the analysis of ground deformation. *International Journal of Applied Earth Observation and Geoinformation* 28: 1–11.

Sartain N, Mian J, Riordan NO & Storry R 2011. *Case study on the assessment of sinkhole risk for the development of infrastructure over karstic ground.* Proceedings of the International Symposium on Geotechnical Safety and Risk held 2-3 June 2011, Munich, Germany: 635–642.

Schättler B, Schwarz E, Mrowka F & Fritz T 2015. *Serving the TerraSAR-X mission For over eight years : current status and recent extensions of the TerraSAR-X ground segment.* Proceedings of the ASAR workshop held 20-22 October 2015, Montreal, Canada: 1–27.

Schunert A & Soergel U 2012. Grouping of Persistent Scatterers in high-resolution SAR data of urban scenes. *ISPRS Journal of Photogrammetry and Remote Sensing* 73: 80–88.

Sharma P, Jones CE, Dudas J, Bawden GW & Deverel S 2016. Monitoring of subsidence with UAVSAR on Sherman Island in California's Sacramento-San Joaquin Delta. *Remote Sensing of Environment* 181: 218–236.

South Africa 2016. *National aerial imagery of South Africa from 2008 to 2012.* (Aerial imagery). Cape Town: Chief Directorate of National Geo-spatial Information.

Stamper P 2011. An analysis of audit committee effectiveness: a case study of public entities in Gauteng. Research report. Pretoria: UNISA, Graduate school of business leadership.

Stevanovic Z, Parise M, Closson D, Gutiérrez F & Stevanović Z 2015. Anticipating and managing engineering problems in the complex karst environment. *Environmental Earth Sciences* 74: 7823–7835.

Stuecheli M, Vaccari A & Acton ST 2012. *Graph cut segmentation of sparsely sampled images with application to InSAR-measured changes in elevation.* Proceedings of the IEEE Southwest Symposium on Image Analysis and Interpretation held 22-24 April, 2012, Santa Fe, United States of America: 149–152.

Sun L & Muller J-P 2016. Evaluation of the use of sub-pixel offset tracking techniques to monitor landslides in densely vegetated steeply sloped areas. *Remote Sensing* 8: 659.

Szwedzicki T 2001. Geotechnical precursors to large-scale ground collapse in mines. *International Journal of Rock Mechanics and Mining Sciences* 38: 957–965.

Tang W, Liao M & Yuan P 2016. Atmospheric correction in time-series SAR Interferometry for land surface deformation mapping - a case study of Taiyuan, China. *Advances in Space Research*: n.p.

Teatini P, Tosi L, Strozzi T, Carbognin L, Cecconi G, Rosselli R & Libardo S 2012. Resolving land

subsidence within the Venice Lagoon by persistent scatterer SAR interferometry. *Physics and Chemistry of the Earth* 40–41: 72–79.

Tebaldini S, Rocca F, Mariotti D'Alessandro M & Ferro-Famil L 2016. Phase calibration of airborne tomographic SAR data via phase center double localization. *IEEE Transactions on Geoscience and Remote Sensing* 54: 1775–1792.

Terwel K & Hanssen RF 2015. *Predicting structural disasters with Radar interferometry.* Proceedings of the International Association for Bridge and Structural Engineering Congress held 23-25 September 2015, Geneva, Switzerland: 824–831.

Thiel C & Schmullius C 2016. The potential of ALOS PALSAR backscatter and InSAR coherence for forest growing stock volume estimation in Central Siberia. *Remote Sensing of Environment* 173: 258–273.

Tomás R, Romero R, Mulas J, Marturià JJ, Mallorquí JJ, Lopez-Sanchez JM, Herrera G, Gutiérrez F, González PJ, Fernández J, Duque S, Concha-Dimas A, Cocksley G, Castañeda C, Carrasco D & Blanco P 2014. Radar interferometry techniques for the study of ground subsidence phenomena: A review of practical issues through cases in Spain. *Environmental Earth Sciences* 71: 163–181.

Trollip NYG 2006. The geology of an area south of Pretoria with specific reference to dolomite stability. Master's thesis. Pretoria: University of Pretoria, Department of Geology.

Vaccari A, Stuecheli M, Bruckno B, Hoppe E & Acton ST 2013. Detection of geophysical features in InSAR point cloud data sets using spatiotemporal models. *International Journal of Remote Sensing* 34, 22: 8215–8234.

Van den Eeckhaut M, Poesen J, Dusar M, Martens V & Duchateau P 2007. Sinkhole formation above underground limestone quarries: A case study in South Limburg (Belgium). *Geomorphology* 91: 19–37.

Van Niekerk A 2014. *Stellenbosch University Digital Elevation Model (SUDEM).* Product description report (2013 edition). University of Stellenbosch: 1–13.

Voigt S, Giulio-tonolo F, Lyons J, Ku J, Jones B, Schneiderhan T, Platzeck G, Kaku K & Hazarika MK 2016. Global trends in satellite-based emergency mapping. *Science* 353, 6296: 247–252.

Watermeyer RB, B BD, Trollip NYG & Pieterse N 2008. *A perfromance based approach to development of dolomite land.* Proceedings of the Geotechnical Division of SAICE's Conference on Problem Soils in South Africa held 3-4 Nov 2008, Midrand, South Africa: 167–174.

Wegmüller U, Walter D, Spreckels V & Werner C 2008. *Evaluation of TerraSAR-X DINSAR and IPTA for ground motion monitoring.* Proceedings of the TerraSAR-X Science Team Meeting held 25-26 November 2008, Oberpfaffenhofen, Germany: 25–26.

Wegmüller U, Werner CL, Strozzi T & Wiesmann A 2002. Phase unwrapping with GAMMA ISP. *Gamma Remote Sensing Technical report*: 1–12.

White MA, Nemani RR, Thornton PE & Running SW 2002. Satellite evidence of phenological

differences between urbanized and rural areas of the eastern United States deciduous broadleaf forest. *Ecosystems* 5: 0260–0273.

Wu Q, Deng C & Chen Z 2016. Automated delineation of karst sinkholes from LiDAR-derived digital elevation models. *Geomorphology* 266: 1–10.

Xia YXY, Kaufmann H & Guo XGX 2002. *Differential SAR interferometry using corner reflectors.* Proceedings of the IEEE International Geoscience and Remote Sensing Symposium held 24-28 June 2002, Toronto, Canada: 1243–1246.

Xie M, Huang J, Wang L, Huang J & Wang Z 2016. Early landslide detection based on D-InSAR technique at the Wudongde hydropower reservoir. *Environmental Earth Sciences* 75, 717: 1–13.

Yechieli Y, Abelson M & Baer G 2015. Sinkhole formation and subsidence along the Dead Sea coast, Israel. *Hydrogeology Journal*: 601–612.

Yu B, Liu G, Li Z, Zhang R, Jia H, Wang X & Cai G 2013. Subsidence detection by TerraSAR-X interferometry on a network of natural persistent scatterers and artificial corner reflectors. *Computers and Geosciences* 58: 126–136.

Yu Z, Li Z & Wang S 2015. An Imaging Compensation Algorithm for Correcting the Impact of Tropospheric Delay on Spaceborne High-Resolution SAR. *IEEE Transactions on Geoscience and Remote Sensing* 53, 9: 4825–4836.

Zebker HA & Villasenor J 1992. Decorrelation in interferometric radar echoes. *IEEE Transactions on Geoscience and Remote Sensing* 30, 5: 950–959.

Zhang L, Ge D, Guo X, Wang Y, Li M & Zhang X 2011. *Seasonal subsidence retrieval with coherent point target SAR interferometry: A case study in Dezhou city.* Proceedings of the IEEE International Geoscience and Remote Sensing Symposium held 24-29 July 2011, Vancouver, Canada: 1600–1603.

Zhou X, Chang N & Li S 2009. Applications of SAR Interferometry in Earth and Environmental Science Research. *Sensors* 9: 1876–1912.